

**ANALYSIS OF FREQUENCY CHARACTERISTICS OF  
SEISMIC REFLECTIONS WITH ATTENUATION IN THIN  
LAYER ZONE: METHODS AND APPLICATIONS**

.....  
A Dissertation

Presented to

the Faculty of the Department of Earth and Atmospheric  
Sciences

University of Houston  
.....

In Partial Fulfillment

of the Requirements for the Degree

Doctor of Philosophy  
.....

By

Shenghong Tai

December, 2009

Analysis of frequency characteristics of seismic reflections  
with attenuation in thin layer zone: methods and applications

---

Shenghong Tai

APPROVED:

---

Dr. John P. Castagna

---

Dr. De-Hua Han

---

Dr. Aibing Li

---

Dr. K.R.Sandyha Devi, Shell Corp.

---

Dean, College of Natural Sciences and Mathematics

## ACKNOWLEDGEMENTS

I am deeply grateful to the many people without whom the completion of this dissertation would not have been possible. My advisor, Dr. John P. Castagna, provided me with solid guidance and encouragement throughout my doctoral research at the University of Houston. His knowledge and ready willingness to help have been great resources for me in learning geophysics. I admire his scientific insight and clear and elegant writing style. My co-advisor, Dr. De-hua Han, always taught me to find the “physics concept” in seismic data analysis. The research-oriented Rock Physics Laboratory has offered me many opportunities to discuss my research with the group, leading to many valuable suggestions. I would also like to thank my committee members Dr. Aibing Li and Dr. K.R.Sandhya Devi for their comments on my dissertation. A special thanks to my friends Qiulang Yao, ZhiJian Zhang, and Tianguang Xu for their encouragement and suggestions that helped me through my most difficult situations. I am also grateful to Charles I. Puryear for his critical comments and proof reading my dissertation. Thanks to all friends who helped me overcome my deficiency in English communication skills.

Finally, my deepest thanks go to my wife, Huiyan Zhang, who has been a constant resource of support, and my lovely daughter, Tai Yang, who brings endless happiness.

**ANALYSIS OF FREQUENCY CHARACTERISTICS OF  
SEISMIC REFLECTIONS WITH ATTENUATION IN THIN  
LAYER ZONE: METHODS AND APPLICATIONS**

.....

An Abstract of a Dissertation

Presented to

the Faculty of the Department of Earth and Atmospheric  
Sciences  
University of Houston

.....

In Partial Fulfillment

of the Requirements for the Degree

Doctor of Philosophy

.....

By

Shenghong Tai

December, 2009

## ABSTRACT

Each hydrocarbon reservoir has its own characteristic seismic frequency response to seismic signals due to its unique rock and fluid properties in the surrounding environment. Much evidence shows the presence of low frequency spectral anomalies with a high degree of correlation to the location of hydrocarbon reservoirs. To understand the physical reasons causing this phenomenon, and to utilize it as an attribute of hydrocarbon indicator, I categorize the influence factors of seismic frequency into two types: global and local factors. The global factors change the frequency of the entire seismic section and determine the background frequency of the seismic section; the local factors only bring some regional or local frequency variation at the given time and location. Wave equations based on synthetic models can be used to generate local frequency energy anomalies related to local fluid properties, lithology change, and layer thickness variation.

Spectral decomposition analyses a signal in both the time and frequency domain. The choice of an analyzing wavelet function is fundamental to any spectral decomposition method and determines the resolution in the two domains. An orthonormal wavelet optimized to a desired signal in the least square sense is utilized by a hybrid spectral decomposition method which combines the continuous wavelet transform with a non-linear operator. This results in significantly improved frequency resolution and enhances local frequency components. The tool can be used to directly compute seismic frequency attributes from seismic data and identify regions of anomalous frequency caused by gas or fluid as seismic wave propagates through them. This is illustrated for hydrocarbon-bearing sands corresponding to frequency anomalies using deep water Gulf of Mexico field seismic data.

## TABLE OF CONTENTS

ACKNOWLEDGEMENTS.....	III
ABSTRACT.....	V
TABLE OF CONTENTS.....	VI
LIST OF FIGURES.....	VIII
<b>CHAPTER 1 Introduction.....</b>	<b>1</b>
1.1 Motivation.....	1
1.2 Assumptions.....	3
1.3 Thesis layout.....	4
<b>CHAPTER 2 Designing an orthonormal wavelet matching a specified signal.....</b>	<b>6</b>
2.1 Summary .....	6
2.2 Introduction .....	6
2.3 Multi-resolution decomposition.....	9
2.4 Construction $\Phi$ from $\Psi$ .....	12
2.5 Guaranteeing orthonormality .....	13
2.6 Matching wavelets .....	14
2.7 Match of phase of the signal .....	16
2.8 Examples of application .....	17
2.9 Discussion.....	25
2.10 Conclusion.....	27
<b>CHAPTER 3 A hybrid wavelet transform based on CWT and non-linear transform.....</b>	<b>29</b>
3.1 Summary .....	29
3.2 Introduction.....	29
3.3 Continuous Wavelet Transform (CWT) and time-frequency decomposition.....	31
3.4 Converting scale to frequency.....	33
3.5 Example of wavelet analysis to the synthetic data .....	34
3.6 The morphological top-hat transforms.....	37

3.7 Combination of CWT and top-hat transform.....	43
3.8 Discussions.....	48
3.9 Conclusions.....	49
<b>CHAPTER 4 Attenuation estimation with continuous wavelet transforms.....</b>	<b>51</b>
4.1 Summary.....	51
4.2 Introduction.....	51
4.3 Methods.....	53
4.4 Synthetic example and application.....	55
4.5 Conclusions.....	60
<b>CHAPTER 5 Frequency characteristics of seismic reflections in thin layer zone.....</b>	<b>62</b>
5.1 Summary.....	62
5.2 Introduction.....	62
5.3 Tuning and peak frequency.....	65
5.4 The factors that influence local frequency of seismic data .....	74
5.5 Conclusions.....	79
<b>CHAPTER 6 Anomalous frequency as a direct hydrocarbon indicator .....</b>	<b>80</b>
6.1 Time–frequency analysis and local-frequency anomaly.....	80
6.2 Field data examples.....	84
6.3 Conclusions.....	94
<b>CHAPTER 7 Conclusions.....</b>	<b>96</b>
7.1 Conclusions.....	96
7.2 Main novelties and achievements of this dissertation.....	97
<b>References.....</b>	<b>99</b>

## LIST OF FIGURES

Figure 2-1. The quadrature mirror filter bank and its frequency response .....	10
Figure 2-2. The frequency responses and amplitude distortion of filters .....	10
Figure 2-3. Constraint matrix A .....	18
Figure 2-4. The amplitude spectrum of input signal and the matched wavelet .....	19
Figure 2-5. Comparison of the original signal and the matched wavelet .....	19
Figure 2-6. A synthetic seismic trace composed of different center frequencies .....	21
Figure 2-7. The synthetic seismic trace and its matched orthogonal wavelet .....	22
Figure 2-8. Comparison of time-frequency decomposition with different wavelets ....	24
Figure 2-9. The uncertainty product $\Delta t * \Delta f$ versus the center frequency .....	26
Figure 3-1. Morlet wavelet in time and frequency domains .....	33
Figure 3-2. The center frequency approximation of a Ricker wavelet .....	34
Figure 3-3. Synthetic seismic trace and its time-frequency spectral by CWT .....	35
Figure 3-4. Morphological dilation of an image .....	38
Figure 3-5. Morphological erosion of an image .....	38
Figure 3-6. Illustration of opening concept .....	39
Figure 3-7. Illustration of performing a top-hat transformation on a function .....	40
Figure 3-8. An example of the top-hat transforms .....	42
Figure 3-9. The flowchart of HWT spectral decomposition .....	44
Figure 3-10. Comparison of results of spectral decomposition .....	45
Figure 3-11. The original signal and its reconstructed signal .....	46
Figure 3-12. Comparison of spectral decomposition of a real seismic trace .....	47
Figure 4-1. Amplitude and time-frequency spectral of a synthetic trace .....	55
Figure 4-2. Amplitude and time-frequency spectral of a synthetic trace with noise ....	56

Figure 4-3. The ratio of Fourier amplitude spectral .....	56
Figure 4-4. The diagram of the measurement and sonic signal .....	57
Figure 4-5. The amplitude spectrum of the signal .....	58
Figure 4-6. The amplitude spectrum of Hilbert transform .....	59
Figure 4-7. CWT time-frequency spectral of the signal .....	59
Figure 4-8. Comparison of the original signal and the forward modeled signal .....	60
Figure 5-1. Three-layer “boxcar” model and its four types of the reflectivity series ....	66
Figure 5-2. Synthetic wedge model and its frequency response in 2D display .....	68
Figure 5-3. Peak frequency versus thickness for different wedge models .....	69
Figure 5-4. Peak frequency versus thickness for two reflectivity models .....	70
Figure 5-5. Tuning effect of the peak frequency for type III reflectivity model .....	72
Figure 5-6. Source frequency effect of peak frequency .....	73
Figure 5-7. Velocity variation effect of peak frequency at fixed thickness .....	76
Figure 5-8. The geology model and its synthetic seismic traces .....	77
Figure 5-9. Peak frequency variation of different Q values and velocities .....	78
Figure 5-10. Comparison of thickness and velocity variation on peck frequency .....	79
Figure 6-1. Curve of peak frequency vs. travel time .....	82
Figure 6-2. 3D seismic data volume of Kingkong reservoir .....	85
Figure 6-3. RMS amplitude of a 2D map at target sand .....	86
Figure 6-4. A seismic profile AB crosses wells .....	87
Figure 6-5. Time-frequency gathers of seismic traces .....	87
Figure 6-6. Low-frequency anomalies profile of AB line .....	88
Figure 6-7. Negative frequency anomalies of 2D map at target sand horizon .....	89
Figure 6-8. 3D volume of frequency-anomaly attributes .....	90
Figure 6-9. Amplitude spectrums of the seismic data .....	91

Figure 6-10. Well log, synthetic trace, and seismic section at KingKong well .....	92
Figure 6-11. The three common frequency sections .....	93
Figure 6-12. A 12 Hz common frequency profile .....	93
Figure 6-13. RMS energy of 2D map at 12 Hz frequency at the target sand .....	94

# CHAPTER 1

## Introduction

### 1.1 Motivation

In the geologic interpretation of seismic data, emphasis has traditionally been placed on the amplitude of the reflected wavelet, whereas its frequency behavior has not been widely used. This is probably due to the fact that variations in amplitude can be related to variations in physical properties such as the velocity and density through the definition of the reflection coefficient in a straightforward manner. Relationships between the peak frequency of a reflected wavelet and the properties of geological formations are complex and related to a variety of factors. Partyka (1999) introduced the concept of frequency decomposition in reservoir characterization. During recent years, seismic frequency characteristics for recognition of hydrocarbon reservoirs have become a major interest due to the rapid development of spectral decomposition techniques. Low-frequency amplitude anomalies associated with reservoirs have been observed for many years. Taner et al. (1979) noted the occurrence of lower apparent frequencies for reflectors on seismic sections beneath gas and condensate reservoirs. John Castagna et al. (2003) showed that frequency decomposition can illuminate low-frequency shadows beneath gas reservoirs. A growing number of surveys over different oil and gas fields throughout the world have established the presence of spectral anomalies with a high degree of correlation to the location of hydrocarbon reservoirs ( Holzner et al., 2005; Akrawi and Bloch, 2006; Graf et al., 2007; Lambert et al., 2008; van Mاسترigit and Al-Dulaijan, 2008). The phenomenon of low frequencies associated with hydrocarbon reservoir is not well understood. Many researchers have applied the attenuation concept to justify low

frequency phenomena because attenuation acts like a low pass filter, i.e. it suppresses higher frequencies proportionally more than the lower frequencies. Some targets that are oil or gas reservoirs usually have a lower Q value than the background and exhibit a zone of anomalous absorption lying in a larger background region (Winkler and Nur 1982; Klimentos, 1995; Parra and Hackert, 2002; Kumar et al., 2003). Yet, it is often difficult to explain observed shadows under thin reservoirs, where there is insufficient travel path through the absorbing gas reservoir to justify the observed shift of spectral energy from high to low frequencies (Castagna, 2003). If the low frequency anomalies were caused by pure attenuation factors, an application of reverse Q filter could recover the high-frequency components within that zone, but, the low-frequency shadow zone still exists even after Q compensation (Yanghua Wang, 2007). Recently, Korneev et al. (2004) tried to explain these low-frequency phenomena using a “frictional-viscous” model (Goloshubin and Bakulin, 1998; Goloshubin and Korneev, 2000; Goloshubin et al., 2006). Saenger (2009) considered poroelastic effects caused by wave-induced fluid flow and oscillations of different fluid phases as significant processes in the low-frequency range that can modify the omnipresent seismic background spectrum.

Although Ebro (2004) gave some possible explanations of low-frequency anomalies, the physical mechanism for the low-frequency anomaly zone is still not well established. The detection of anomalous zones is clearly the first step in analyzing this possible direct hydrocarbon indicator. It would still be useful to determine the mechanism of the effect, so that the effect could be quantitatively related to the reservoir properties.

The purposes of this dissertation are to analyze and understand the mechanisms that influence the local frequency components of seismic data in a thin layer (a quarter

wavelength thickness) without attempting to address specific mechanisms of attenuation for fractured and porous media. I built a set of synthetic forward models based on wave-equation to help understand and evaluate the contributions of various factors related to local fluid properties, lithology changes, and layer thickness variation to local frequency anomalies. A new spectral decomposition method was developed to extract hydrocarbon related frequency anomaly and illustrated on synthetic and real data.

## **1.2 Assumptions**

An important assumption of this work is a constant quality factor  $Q$  in the operational frequency band. For the synthetic seismic model we apply the wave equation operator to the plane wave describing the seismic propagation; the Ricker wavelet is used as a source wavelet in our forward modeling technique. I ignore multiple and scattering phenomena to study the peak frequency characteristic of seismic reflections from a wedge model with arbitrary upper and lower normal incidence reflection in Chapter 5 and 6. Analysis and discussion have not been limited to layers of sufficient thickness for the top and bottom reflected wavelets to be resolved, but also to the thickness less than the tuning thickness. When the two reflections are not resolvable in the time domain, the thickness information is encoded in the amplitude and shape of the reflected wavelet. Attention is focused on the change in frequency content of the reflected seismic waveforms due to the dispersive behavior of thin layer reflectivity, which varies according to the frequency content of the incident impulse. To make the assumptions clear, they are also reiterated throughout the dissertation as appropriate.

### **1.3 Thesis layout**

In addition to the introduction and conclusions, the thesis consists of five chapters on various aspects of spectral decomposition and application of frequency characterization: Spectral decomposition analyzes the signal in the time-frequency domain. The choice of a wavelet function is very important in any spectral decomposition method to keep a good resolution in both domains. In Chapter 2, I describe a method to design an orthonormal wavelet, which is optimized to the desired signal in the least square sense. For signal detection applications, the decomposition of a signal in the presence of noise using a wavelet matched to the signal would produce a sharper or higher resolution in time-frequency space as compared to standard non-matched wavelets. A continuous wavelet transform (CWT) is a time-frequency analysis method. Unlike Fourier transform, the continuous wavelet transform possesses the ability to construct a time-frequency representation of a signal that offers very good time and frequency localization. In Chapter 3, I develop a hybrid spectral decomposition method, which combines the continuous wavelet transform with a non-linear operator. This spectral decomposition method can significantly improve frequency resolution and enhance local frequency components. Compared to other spectral decomposition methods such as matching pursuit, the algorithm runs very fast, because it takes an advantage of fast Fourier transform for CWT and a logical operator in extracting local maxima. Chapter 4 describes attenuation estimation with continuous wavelet transforms. I had found that spectral ratios obtained using continuous wavelet transforms as compared to Fourier ratios are more accurate, less subject to windowing problems, and more robust in the presence of noise, which results in a more robust and effective means of estimating  $Q$ .

In order to understand the physical mechanisms for low-frequency anomalies associated with reservoirs, I analyze the mechanisms that influence local frequency components of seismic data in thin layers in Chapter 5. A detailed forward model is built to guide understanding of the underlying physical factors and evaluation of the contributions of various factors related to local fluid properties, lithology change, and layer thickness variation to local frequency anomalies. In Chapter 6, a definition for trend is introduced; a corresponding algorithm for finding intrinsically the trend and implementing the detrending also is presented. I show how to use the developed method to directly compute seismic frequency attributes and to extract local frequency anomalies from field data that includes the KingKong reservoir and a nearby fizz gas well (Lisa Anne). Conclusions in Chapter 7 summarize the main achievements and novelties of this dissertation.

## **CHAPTER 2**

### **Designing an orthonormal wavelet matching a specified signal**

#### **2.1 Summary**

In this chapter, an efficient approach to obtain an orthonormal wavelet that is matched to seismic signal is developed. The error between the wavelet and the seismic signal is minimized subject to the constraints of the amplitude of the band-limited wavelet spectrum. The phase-matching algorithm is developed in time domain to minimize the difference of the energy between the desired signal and the optimum wavelets. Matching a wavelet to a signal of interest has potential advantages in extracting signal features with greater accuracy, particularly when the signal is contaminated with noise. We have applied this technique to a carefully designed synthetic seismic signal. The results indicate that a matched wavelet, that was able to capture the broad seismic signal features, performs better image resolution than standard wavelets in decomposing the complex spectra when uncorrelated noise is present, and also when modes overlap in time and frequency domains.

#### **2.2 Introduction**

In seismic exploration, spectral decomposition is a tool that produces a continuous time-frequency analysis of a seismic trace. Thus, a frequency spectrum is output for each time sample of the seismic trace (Chakraborty and Okaya, 1995; Partyka et al., 1999; Castagna et al., 2003). Time-frequency analysis of a given signal may be interpreted as a wavelet decomposition of the signal into a set of frequency channels. Unlike Fourier analysis,

spectral decomposition using wavelet transforms can be implemented using a non-unique process or a non-unique basis; thus, the same seismic trace can result in different time-frequency character analysis (Castagna and Sun, 2006). In signal feature detection and pattern recognition, the decomposition of a signal in the presence of noise using a wavelet matched to the signal produces higher resolution in time-frequency space than standard wavelets. This resolution improvement is one reason wavelet application have become a topic of research in diverse fields. Specifically, finding a wavelet that represents the best estimate for a given signal has become a topic of significant research interest in the last decade. Mallat and Zhang (1993) pointed out that a single wavelet basis function is not flexible enough to represent a complicated non-stationary signal such as seismic signal. To address this shortcoming, techniques have been developed to find orthonormal wavelet bases with compact support (Daubechies, 1998; Mallat, 1999). In these techniques, a dictionary of mother wavelets is pre-computed to be used in the matching process. The matching algorithm selects the mother wavelet from the dictionary that provides the best match to the signal at the time location of interest (Wang, 2007). This selection process gives rise to optimal matching for the lower frequency band of the signal. However, the output of this matching technique is strongly influenced by the contents of the dictionary; the dictionary of pre-defined functions might not include functions that compactly represent the signal of interest. Also, representing different segments by different functions does not optimally reflect the temporal structure of the signal. Various techniques to find wavelets that minimize these deficiencies have been investigated by different researchers (Chapa and Rao, 2000; Gupta et al., 2005). Chapa and Rao (2000) obtained a solution for constructing adaptive band-limited wavelets. They

have shown that for orthonormal multi-resolution analysis with band-limited wavelets, there is a solution that yields wavelets that “look” like a desired signal. They used a sub-optimal matching algorithm in the sense that it is performed on the magnitude and phase obtained from the Fourier transform of the wavelet independently of one another (Vaidyanathan, 1993; Rao and Bopardikar, 1998). Recently, Bahrapour et al. (2008) simplified Chapa’s method by reducing the optimal matching problem to the solution of a set of functional equations for the amplitude and phase of the wavelet spectrum. However, Takal et al. (2006) pointed out that the group delay of the matched wavelet, obtained by Chapa’s method of matching the phase spectra of the signal and matched wavelet, did not closely match in the low-frequency band of the signal primarily due to the fact that the signal had to be band limited to satisfy the required orthonormality constraints.

In this chapter, I describe how such a technique could be applied to generate a mother wavelet that matches the seismic signal. We developed a method to match the phase of desired signal in least squares sense in the time domain, which also automatically satisfies the periodicity constraints and the Poisson summation constraints used to match the amplitude spectra (Gupta, 2005). The algorithm to match the phase of the signal was implemented by iterative procedures. Although the method of matching the wavelet to a desired signal was derived using the constraint of orthonormal multi-resolution analysis (OMRA) based on 2 scaling factor, it also can be generalized to an M-band wavelet system. I applied the method to extract a matched wavelet from a synthetic seismic data and utilized the wavelet to decompose the signal to a time-frequency domain through the hybrid continuous wavelet transform (which is described in Chapter 3). The results show

that the matched wavelets discriminate various features in complex signals better than standard wavelets, such as Morlet (Chui, 1992; Kritski et al., 2007) and Ricker wavelets, which are commonly used in applied geophysics.

### 2.3 Multi-resolution decomposition

Mallat (1999) showed that the discrete wavelet transform can be used to generate an orthonormal multi-resolution decomposition of a discrete signal consisting of a series of detail functions and a residual low-resolution approximation of the original signal. Chapa and Rao's algorithm applies multi-resolution analysis (MRA) to develop an orthonormal wavelet that matches a signal of interest. The multi-resolution analysis involves a decomposition of the function space into a sequence of subspaces  $V_j$ . The orthonormal MRA decomposes a signal,  $f(x)$ , into a series of detail functions  $W_j$  and a residual low resolution approximate function,  $V_j$ . That is,  $f(x)$  is projected onto  $W_j$  and  $V_j$ , where  $V_{j-1} = V_j \oplus W_j$ ,  $\oplus$  denotes the union of spaces (like the union of sets). The orthogonal complement of  $V_j$  is  $W_j$ . The recursive projection of  $f(x)$  onto  $V_j$  and  $W_j$  produces the detail functions  $g_j(x)$  and  $f_j(x)$  such that

$$f(x) = f_j(x) + \sum_{j=1}^J g_j(x) \quad (2.1)$$

The orthonormal bases of  $W_j$  and  $V_j$  are given by the wavelets  $\psi_{jk}(x)$  and scaling function  $\phi_{jk}(x)$ , where

$$\langle \psi_{jk}(x), \phi_{j'k'}(x) \rangle = \delta(j - j')(k - k') \quad (2.2)$$

For a two-band decomposition, the forward transform consists of analysis filter pair  $h_0$  (low pass) and  $h_1$  (high pass) followed by down sampling, while an up sampling ahead of the reverse transform filters pair  $g_0$  and  $g_1$  which called synthesis filters. A pyramid algorithm computes the forward transform. Higher level wavelet transform coefficients of a signal are determined recursively by decimated convolution of analysis filters with lower level wavelet transform coefficients. The inverse transform is performed by using the synthesis filters to replace the analysis filters and reversing the sequence of the forward transform algorithm (Figure 2.1). The high-and low-pass filters should have less overlap in their spectra (Figure 2.2) so that amplitude distortion may be minimized.

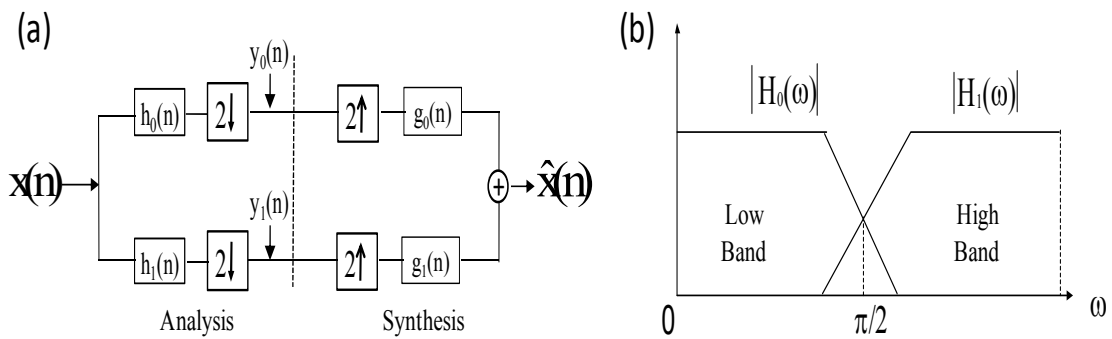


Figure 2.1 (a) The quadrature mirror filter bank. (b) Typical frequency magnitude response of analysis filters.

If  $H_0(\omega)$  has good pass-band and stop-band responses, then the amplitude distortion almost keeps constant in the pass bands of  $H_0(\omega)$  and  $H_1(\omega)$ . The main difficulty comes in the transition band region. The degree of overlap of  $H_0(\omega)$  and  $H_1(\omega)$  is very crucial in determining this distortion. Figure 2.2a shows the response of three linear phase designs of  $H_0(\omega)$ . If the pass-band edge is too small as in the first curve, the amplitude distortion exhibits a dip at approximately  $\pi/2$ . If the pass-band edge is too large as it shows in the

second curve (i.e.  $H_0$  and  $H_1$  have too much overlap), the amplitude distortion exhibits peaks at approximately  $\pi/2$ . The third curve, where the pass-band edge is carefully chosen, produces a less distorted response which is a much better response of the amplitude. The goal of designing a pass-band filter  $h_0$  is to adjust the coefficient of  $h_0$  so

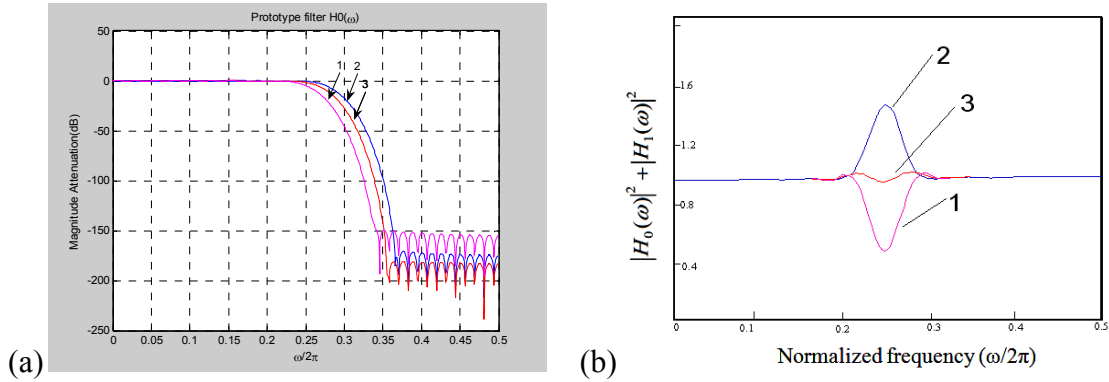


Figure 2.2 ( a) The frequency responses of three different  $H_0(\omega)$ . ( b) Amplitude distortion as function of degree of overlap between analysis filters.

that the filter pairs satisfy the condition  $|H_0(\omega)|^2 + |H_1(\omega)|^2 = 1$ .

In order to perfectly reconstruct the original signal from the detail functions and the residual approximation, the following must be true of the Fourier spectral magnitudes of  $h$  and  $g$ .

$$|H(\omega)|^2 + |G(\omega)|^2 = 1 \tag{2.3}$$

Cancellation of aliasing is achieved by setting  $g_k = (-1)^k h_{1-k}$ . The filters,  $h$  and  $g$  are related to the mother wavelet,  $\psi(x)$ , and the scaling function,  $\phi(x)$  by their 2-scale relations,  $\psi(x) = 2 \sum_k g_k \phi(2x - k)$  and  $\phi(x) = 2 \sum_k h_k \phi(2x - k)$  or in the frequency domain by

$$\Psi(\omega) = G\left(\frac{\omega}{2}\right)\Phi\left(\frac{\omega}{2}\right), \quad \Phi(\omega) = H\left(\frac{\omega}{2}\right)\Phi\left(\frac{\omega}{2}\right) \tag{2.4}$$

## 2.4 Construction $\Phi$ from $\Psi$ .

A recursive equation for finding  $\Phi(\omega)$  from  $\Psi(\omega)$  can be found by taking the squared magnitude of equations (2.4), adding them, then substituting equation (2.3), giving:

$$\begin{aligned} |\Phi(2\omega)|^2 + |\Psi(2\omega)|^2 &= |H(\omega)\Phi(\omega)|^2 + |G(\omega)\Phi(\omega)|^2 \\ &= (|H(\omega)|^2 + |G(\omega)|^2)|\Phi(\omega)|^2 \\ &= |\Phi(\omega)|^2 \end{aligned} \quad (2.5)$$

Substituting  $\omega = \pi n$ ,  $n \in \mathbb{Z}$  yields

$$|\Phi(n\pi)|^2 = |\Phi(2n\pi)|^2 + |\Psi(2n\pi)|^2 \quad (2.6)$$

Since we are seeking to construct an orthonormal multi-resolution analysis,  $\phi(x)$  must be orthonormal, and its Poisson summation must be equal to 1 everywhere.

$$\sum_{m=-\infty}^{\infty} |\Phi(\omega + 2\pi m)|^2 = 1 \quad (2.7)$$

If  $\Phi(\omega)$  is normalized such that  $\Phi(0) = 1$ , the Poisson summation is

$$|\Phi(2n\pi)| = \{1 \text{ for } n = 0, \text{ or } 0 \text{ for } n \neq 0\}, \quad (2.8)$$

and equation (2.6) can be rewritten as

$$|\Phi(2n\pi)| = \{1 \text{ for } n = 0, \text{ or } \Psi(2n\pi) \text{ for } n \neq 0\}. \quad (2.9)$$

Therefore, at integer multiples of  $\pi$ ,  $\Phi$  can be computed directly from values of  $\Psi$ .

Substituting  $\omega = \pi n / 2$  in (2.5) gives:

$$\left| \Phi\left(\frac{n\pi}{2}\right) \right|^2 = |\Phi(n\pi)|^2 + |\Psi(n\pi)|^2 \text{ for } n \neq 0. \quad (2.10)$$

At integer multiples of  $\pi/2$ ,  $\Phi$  can be computed from values of  $\Psi$  and the previously calculated values of  $\Phi$ . Repeated substitution leads to the following closed form solution.

$$\left| \Phi\left(\frac{\pi n}{2^l}\right) \right|^2 = \sum_{p=0}^l \left| \Psi\left(\frac{2\pi n}{2^p}\right) \right|^2 \text{ for } n \neq 0 \quad (2.11)$$

## 2.5 Guaranteeing orthonormality

Lawton (1999) described the necessary and sufficient condition for constructing orthonormal wavelet bases. Given that  $g_k = (-1)^k h_{1-k}$  and  $\Phi(0) = 1$ , the multi-resolution generated by  $\phi(x)$  and related to  $\psi(x)$  is orthonormal if

$$\begin{aligned} \langle \phi_{j,k}, \phi_{j,m} \rangle &= \delta_{k,m} \\ \langle \phi_{j,k}, \psi_{j,m} \rangle &= 0 \\ \langle \psi_{j,k}, \psi_{l,m} \rangle &= \delta_{j,l} \delta_{km} \end{aligned} \quad (2.12)$$

Therefore, an orthonormal multi-resolution analysis is guaranteed when the scaling function is orthonormal, thereby satisfying (2.7). Let  $\Delta\omega = \pi / 2^l$ , then

$$|\Phi(n\Delta\omega)|^2 = \sum_{p=0}^l \left| \Psi\left(\frac{2^{l+1}n\Delta\omega}{2^p}\right) \right|^2 \quad \text{for } n \neq 0 \quad (2.13)$$

Setting  $n\Delta\omega = n\Delta\omega + 2\pi m$  and summing over  $m$  gives

$$\sum_{m=-\infty}^{\infty} |\Phi(n\Delta\omega + 2\pi m)|^2 = \sum_{m=-\infty}^{\infty} \sum_{p=0}^l \left| \Psi\left(\frac{2^{l+1}(n\Delta\omega + 2\pi m)}{2^p}\right) \right|^2 \quad (2.14)$$

The left side of (2.14) is the Poisson summation sampled at  $\Delta\omega$  and must be equal to 1 everywhere if  $\phi(x)$  is orthonormal. Therefore, substituting for  $\Delta\omega$  gives a necessary condition on  $\Psi$  that will guarantee an orthonormal multi-resolution analysis

$$\sum_{m=-\infty}^{\infty} \sum_{p=0}^l \left| \Psi\left(\frac{2\pi}{2^p}(n + 2^{l+1}m)\right) \right|^2 = 1 \quad (2.15)$$

A wavelet whose spectrum satisfies the condition in (2.14) will be guaranteed by (2.15) that the Poisson summation for  $\Phi(\omega)$  is equal to 1 everywhere. Therefore, (2.15) is necessary and sufficient to guarantee that  $\phi(x)$  generates an orthonormal multi-resolution analysis.

## 2.6 Matching wavelets

Finding the matched wavelet is done numerically with discrete  $\Psi$ . We will assume that the resultant wavelet is real and therefore has a symmetric frequency spectrum. Assume the scaling function derived from the wavelet in (2.10) has a minimum sample spacing of  $\Delta\omega_{\min} = \pi / 2^l$  the minimum sample spacing required of is  $2 \Delta\omega_{\min} = \pi / 2^{l-1}$ . Now let's assume that  $\Psi(\omega)$  is band-limited to  $\pi K_L < |\omega| < \pi K_U$ , where  $K_L, K_U \in \mathfrak{R}$ , then the argument of (2.15) is limited to

$$\pi K_L < \left| \frac{2\pi}{2^p} (n + 2^{l+1} m) \right| < \pi K_U . \quad (2.16)$$

Let  $Y(k) = |\Psi(2k\Delta\omega_{\min})|^2$   $K \in \mathbf{Z}$ , then condition (2.15) and (2.16) become

$$\sum_{m=-\infty}^{\infty} \sum_{p=0}^l Y\left(\frac{2\pi}{2^p} (n + 2^{l+1} m)\right) = 1 \quad (2.17)$$

$$2^{M-1} K_L < \left| \frac{2\pi}{2^p} (n + 2^{l+1} m) \right| < 2^{M-1} K_U \quad 0 \leq \ell \leq M . \quad (2.18)$$

Assuming that  $|\Psi(\omega)| = |\Psi(-\omega)|$ , the conditions in (2.17) generate a set of L linear constraints in  $Y(k)$  of the form

$$\sum_{i=1}^L a_{ik} Y(k) = 1, \quad (2.19)$$

where  $k = [2^{M-1}K_L], \dots, [2^{M-1}K_U]$  since  $n$  and  $m$  are integers and we are matching only one side of a symmetric spectrum. Let the desired signal spectrum, sampled at  $2\Delta\omega_{\min}$ , be given as  $S(k)$  and let  $W(k) = |S(k)|^2$  be its power spectrum. Then the objective function,  $E$ , to be minimized is defined as the mean square error between  $Y$  and  $W$ , normalized by the energy in  $W$ .

$$E = \frac{(W - Y)^T (W - Y)}{W^T W} \quad (2.20)$$

$$AY = \bar{1} \quad (2.21)$$

where  $A = \{a_{ik}\}$  and  $\bar{1}$  is a vector of 1's with length  $L$ . It is important to note that  $A$  is a function of  $K_L$  and  $K_U$  only. After setting the band-limits set, and deriving  $A$ , the objective function is chosen to be the mean square error between the power spectra of  $\Psi$  and  $S$ , so that the minimization problem is linear and has a closed form solution using Lagrangian multipliers. The Lagrangian function is given as

$$L = \frac{(W - Y)^T (W - Y)}{W^T W} + \lambda (AY - \bar{1}) \quad (2.22)$$

and the object function is minimized by setting  $\Delta L = 0$ , which gives

$$Y = A^T (AA^T)^{-1} (\bar{1} - AW) + W \quad (2.23)$$

Since  $Y(k) = |\Psi(k\Delta\omega)|^2$ , we include the inequality constraints  $Y(k) \geq 0$ . If the solution in (2.23) has a negative value, then it can be set to 0 with an additional equality constraint in

A. From the error,  $E$ , given by

$$E = \frac{(\bar{1} - AW)^T (AA^T)^{-1} (\bar{1} - AW)}{W^T W} \quad (2.24)$$

we see that the error in the match is a function of the deviation of  $AW$  from  $\bar{1}$ . If the desired signal already satisfies the constraints for an orthonormal MRA, then the deviation from  $\bar{1}$  is 0,  $E = 0$ , and from (2.23)  $Y=W$ . As  $W$  moves away from the constraints, the error in the match,  $E$ , increases. It can also be seen from both (2.23) and (2.24) that any scale factor applied to  $W$  would affect the solution,  $Y$ , and the error in the match  $E$ . Let the input spectrum be normalized by a constant  $\alpha$ ; the solution in (2.23) and the error in (23) becomes

$$Y(a) = A^T (AA^T)^{-1} \left(1 - \frac{1}{a} AW\right) + \frac{1}{a} W \quad (2.25)$$

$$E(a) = \frac{\left(1 - \frac{1}{a} AW\right)^T (AA^T)^{-1} \left(1 - \frac{1}{a} AW\right)}{\frac{1}{a} W^T W} \quad (2.26)$$

Setting  $dE(a)/da = 0$  and solving for  $a$  gives the value of the normalizing factor on  $W$  that will produce the minimum error  $E$ .

$$a = \frac{1^T (AA^T)^{-1} AW}{1^T (AA^T)^{-1} 1} \quad (2.27)$$

## 2.7 Matching the phase of the wavelet to the signal

Since the resultant of the previous step yields the wavelet magnitude spectrum only, the wavelet  $Y(t)$  is symmetrical in the time domain with zero degree phases. In order to match the group delay of the resultant wavelet to the group delay of a desired signal, we rotate the phase of the wavelet in the time domain so that it matches the desired signal in a least squares sense. The energy difference between the desired signal and the matched wavelets is given by:

$$R_k(t) = \sum_{i=1}^N (S(t_i) - Y(t_i, \theta_k))^2, \quad (2.28)$$

where  $N$  is sample number,  $\theta$  is the phase angle of the wavelet,  $\theta_k$  stand for the  $k$ -th iterate of  $\theta$ . Our objective is to minimize  $R(t)$  by rotating the wavelet phase given by the formula:

$$Y(t, \theta) = Y(t) \cos(\theta) + Y^H(t) \sin(\theta), \quad (2.29)$$

here,  $Y^H(t)$  is the imaginary function of Hilbert transform of the wavelet  $Y(t)$ .

The phase matching part of the wavelet matching algorithm is as follows:

- 1) Take the Hilbert transform of the wavelet  $Y(t)$  to obtain its imaginary function

$$Y^H(t).$$

- 2) Initialize the  $\theta$  value starting from 0 with step  $\Delta\theta = 0.5$  or less to update

$$\theta_{k+1} = \theta_k + \Delta\theta.$$

- 3) Calculate  $Y(t, \theta)$  by the formula (2.29).

- 4) Compute the least-squares residuals  $R_{k+1}(t)$  from the formula (2.28).

- 5) If  $R_{k+1}(t) < R_k(t)$ , return to step 2 continuously repeat step 2 to 5 until  $R_{k+1}(t) >$

$$R_k(t), \text{ stop updating } \theta_k.$$

$Y(t, \theta_k)$  is a matched wavelet of the desired signal with orthonormal features. Since the phase matching is implemented in the time domain which also automatically satisfies the periodicity constraints and the same constrains used to match the amplitude spectra.

## 2.8 Examples of application

To demonstrate the performance of the spectrum matching algorithm, the algorithm is applied to the transient signal given by the following formula:

$$f_T(t) = 0.1te^{-\alpha t} \cos(\omega_0 t)u(t), \quad (2.30)$$

where  $u(t)$  is the unit-step function. The transient signal in this example was constructed by setting  $\alpha = 2$  and  $\omega_0 = 1.6\pi$ , and dilating it such that its spectrum,  $F_T(\omega)$ , has maximum energy in the pass band  $2\pi/3 \leq |\omega| \leq 8\pi/3$ . Figure 2.5a shows the transient signal. Let  $l = 5$  so that  $\Delta\omega = 2\pi/2^5$ . The optimization procedure operates on the non-zero portion of the positive frequency axis,  $K=11, 12, \dots, 43$ . The constraint matrix,  $A = \{a_{ik}\}$  derived from (2.17) is given in Figure 2.3.

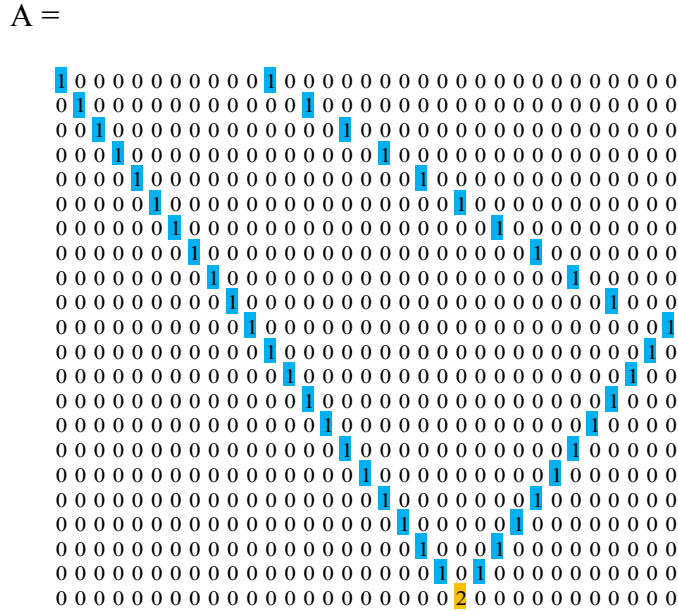


Figure 2.3 Constraint matrix A for  $\{Kl, Ku\} = \{2\pi/3, 8\pi/3\}$ .

We calculate  $W(k)$  using the following expression:  $W(k) = |\Psi_m(k\Delta\omega)|^2$ . The amplitude of the matched wavelet in the positive band is shown in Figure 2.4(a). It can be shown that the Poisson summation of the matched wavelet is  $\sum_{m=-\infty}^{\infty} |\Phi(\omega + 2\pi m)|^2 = 1$ , meaning that it is orthonormal. The phase of the matched wavelet can be obtained by rotating its angle so that it matches the original signal energy in the time domain in the least squares sense.

We follow the procedures described in section 6 and obtain the best matched wavelet after rotating 155 degree from the zero phase matched wavelet. The resulting of the matched wavelet is shown by the red solid line in Figure 2.5b. Although the function that is used in this example is not band-limited, the calculated wavelet and the signal are well matched.

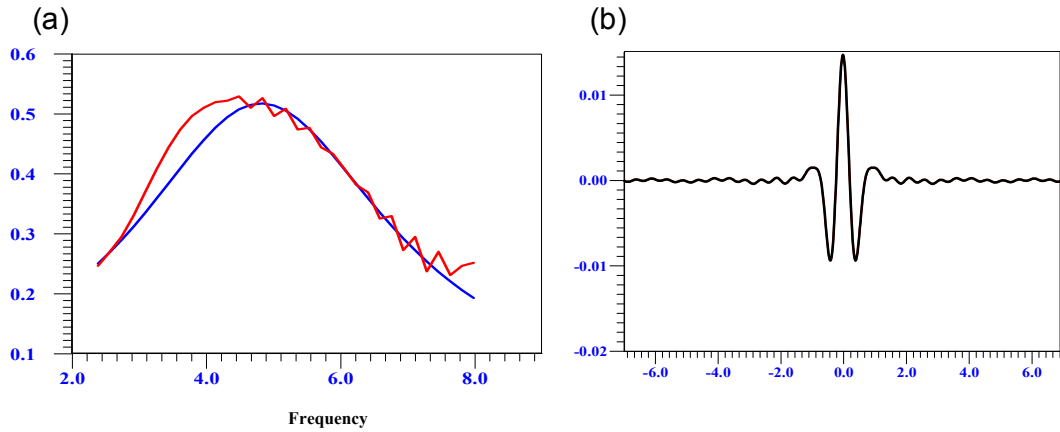


Figure 2.4 (a) The amplitude of the spectrum of the transient signal  $f_T(t)$  and corresponding adapted wavelet are presented. Red line: the optimal wavelet. Blue line: original signal. (b) The matched wavelet with zero degree phases.

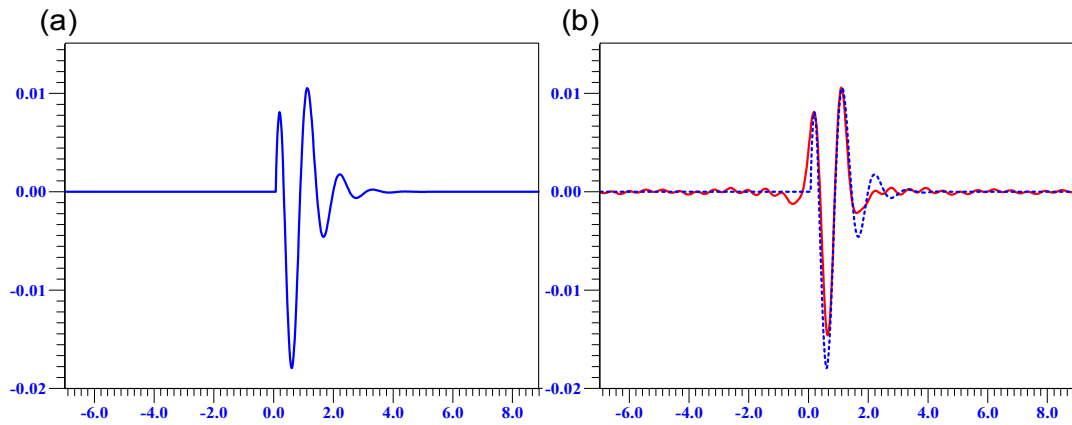


Figure 2.5 The transient  $f_T(t)$  and corresponding adapted wavelets are presented. (a) The transient signal. (b) Dashed blue line: the optimal adapted wavelet matched by the method described in this paper. Solid red line: original signal.

We applied the method described in this paper to a carefully designed synthetic seismic signal. Figure 2.6 shows a synthetic trace generated by the wave propagation equation using Ricker wavelets with different center frequencies as source wavelets; the center frequencies are at 20Hz, 40Hz, 55Hz, and 70 Hz respectively. We considered intrinsic attenuation in the synthetic data by varying the quality factor  $Q$  for the different synthetics; we see that the amplitude of the signal decreases and wavelets are lengthened gradually along the time axes of each trace. The synthetic trace is a superposition of four traces. The Fourier spectral analysis of the band-limited signal is shown in Figure 2.7b (blue line). In order to reduce spectral leakage from adjacent Fourier frequency bins and thereby improve the dynamic range of the analysis (Percival, 1993), we use the power-spectral density to characterize the signal power instead of directly using the Fourier energy spectrum of the signal (Figure 2.7b red line). We dilate the signal such that its spectrum has maximum energy in the pass band  $\{2\pi/3, 8\pi/3\}$ . Hence, the constraint matrix,  $A$ , remains unchanged.

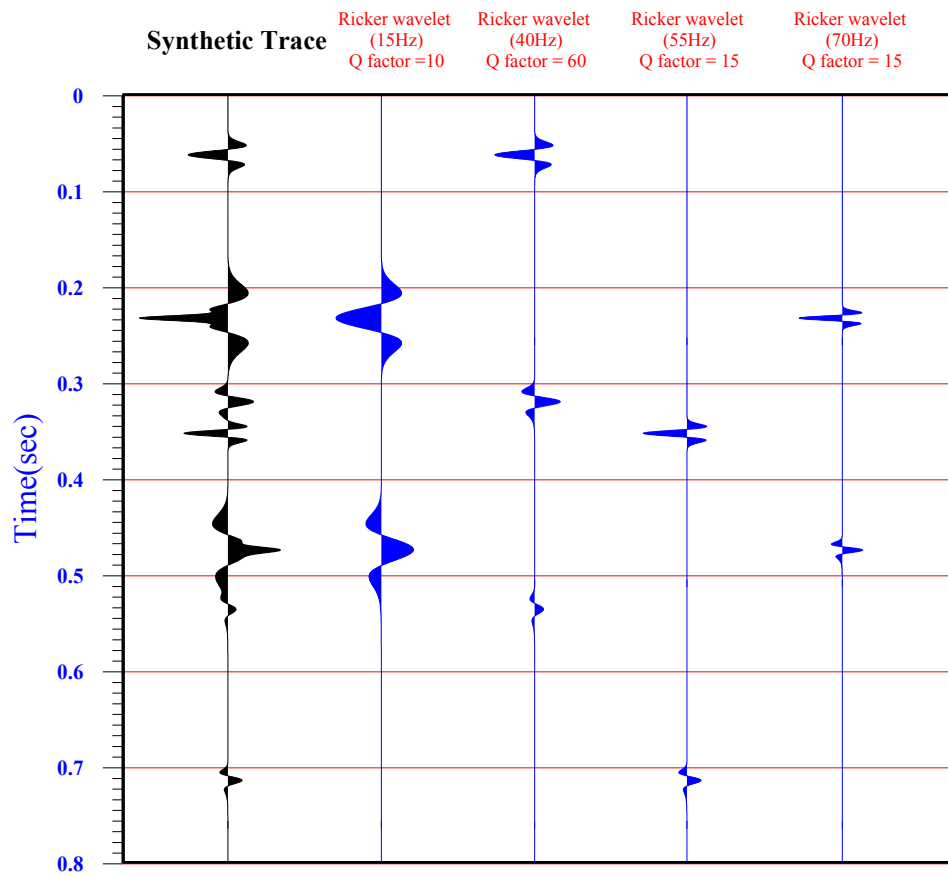


Figure 2.6 Synthetic trace composed of Ricker wavelets with different center frequencies. Q values are specified at the top.

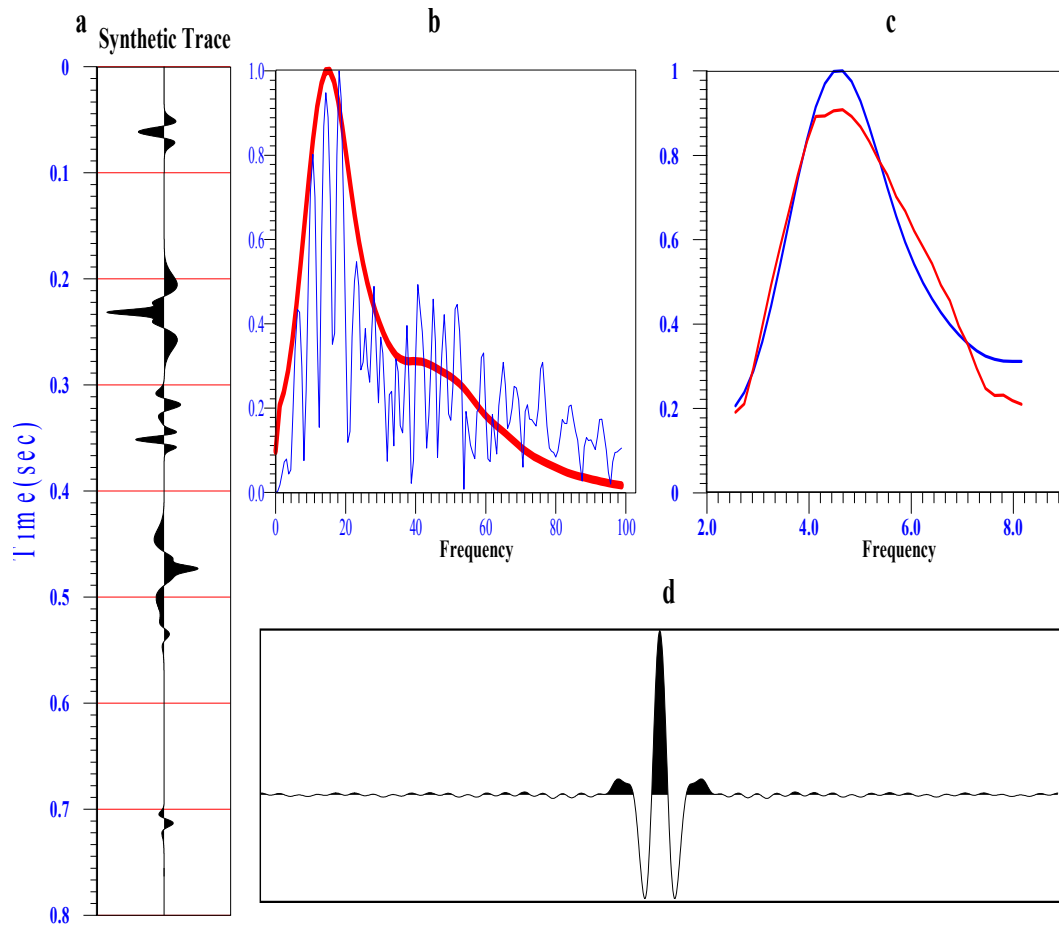


Figure 2.7 (a) The synthetic seismic trace. (b) The normalized Fourier frequency spectrum (blue line) and the power spectral density (red line) of the signal. (c) The modulated spectrum of the signal and corresponding adapted wavelet. Red line: the optimal adapted wavelet. Blue line: the synthetic signal. (d) The optimal adapted matched orthogonal wavelet.

Figure 2.7c shows the spectra of the truncated signal and the matched wavelet. The matched zero degree phase wavelet is shown in Figure 2.7d. Since the key elements of

the method in the extraction of analysis wavelet from a given signal is similar to a sharpening filter used in signal enhancement, thus for signal detection and recognition applications, the decomposition of a signal by a wavelet matched to the signal would produce a sharper or taller peak in time-scale space as compared to standard non-matched wavelets. We have tested this concept through time-frequency decomposition of the synthetic signal using a hybrid wavelet transform (the method will be introduced in chapter 3). We used the matched wavelet as a mother wavelet to decompose the synthetic seismic signal into the time-frequency domain. For comparison, three different wavelets are used to decompose the signal, the matched wavelet, the Morlet wavelet and the Ricker wavelet respectively. The Morlet and Ricker wavelets are popular for various time frequency decomposition methods in seismic data processing. Figure 2.8 shows the results of the wavelet decomposition of the synthetic signal using three different wavelets. The matched wavelet clearly results in a prominent peak at the appropriate time and frequency location for spectral decomposition as compared to the Morlet wavelet and the Ricker wavelet. Each individual event spectrum shown in Figure 2.6 can be clearly identified in the corresponding the time-frequency decomposition plot in Figure 8a. Specifically, two events close to 230 milliseconds and 470 milliseconds containing two different center frequency wavelets, which were not isolated by the Ricker wavelet decomposition, are clearly defined by the matched wavelet decomposition. The Ricker wavelet decomposition smeared the energy of the two events

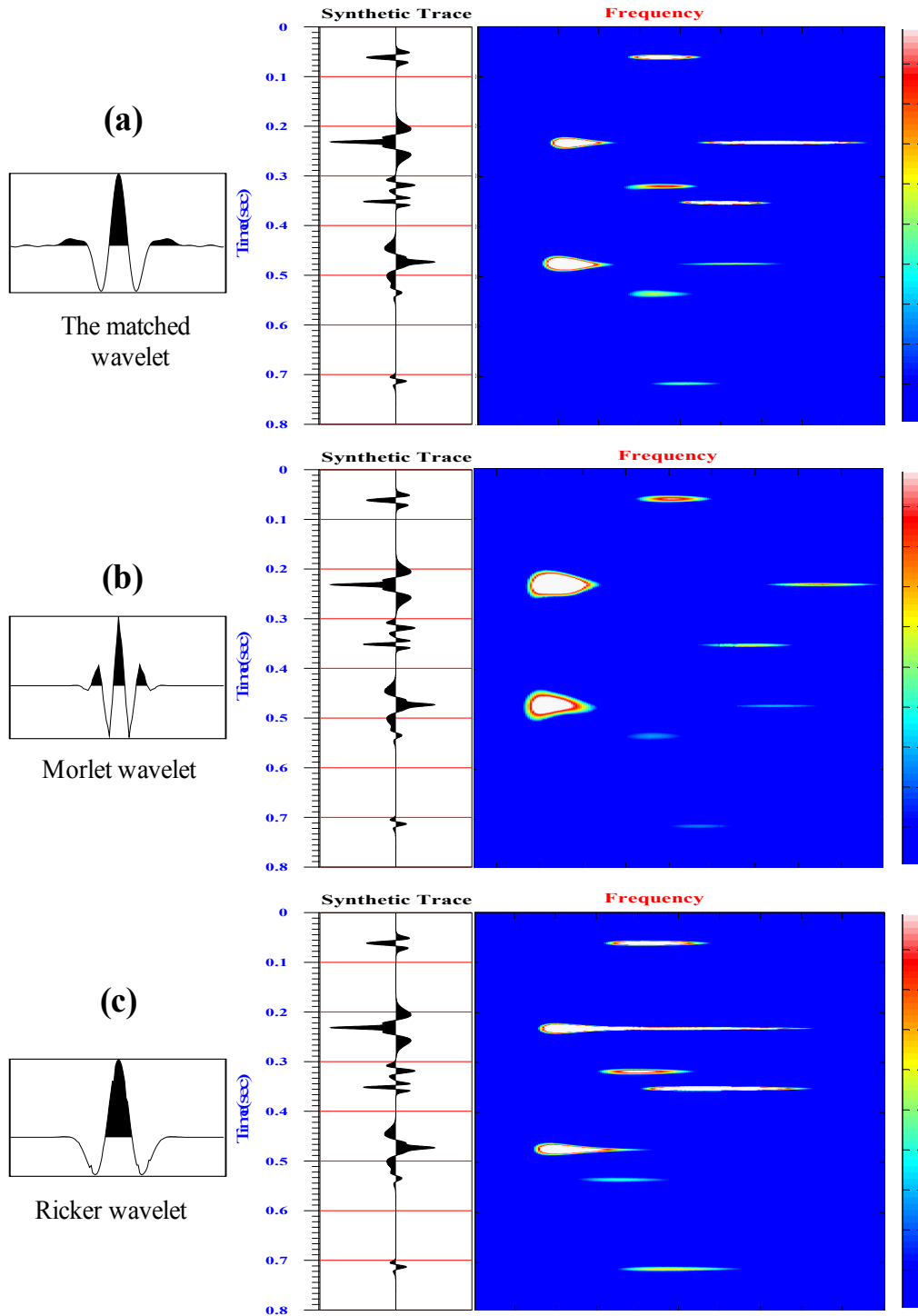


Figure 2.8 The results of time-frequency decomposition of the synthetic trace by using three different wavelets. (a) is the result of time –frequency using the matched wavelet, (b) is the result using the Morlet wavelet , and (c) is the result using the Ricker wavelet.

with the different frequencies near 230 milliseconds and missed a high frequency event near 470 milliseconds. The Morlet wavelet is very well localized in the frequency domain but poor for its time resolution. In this case, the Morlet wavelet couldn't detect the events at 320 milliseconds because the two events are too close to each other in the time series, which is beyond of its time resolution.

## 2.9 Discussions

The Heisenberg Uncertainty Principle states that the wavelength and frequency bandwidth of a waveform cannot both be arbitrarily decreased simultaneously. The uncertainty principle for waveform analysis says that if the effective bandwidth of a signal is  $\omega$ , then the effective duration cannot be less than  $1/\omega$  and vice versa. This principle is mathematically formulated as:

$$\Delta \tau \cdot \Delta \omega \geq 1/2, \quad (2.31)$$

where  $\Delta$  refers to the standard deviation,  $\tau$  is the time, and  $\omega$  is angular frequency. Therefore, it can be inferred that one can achieve an arbitrary level of resolution in one domain at the expense of the other. We quantify each wavelet at every frequency for standard deviation in time and frequency by using the following equation:

$$\sigma = \{\sum P(x)(x - \mu)^2\}^{(1/2)}, \quad (2.32)$$

where  $P(x)$  represents the amplitude distribution with respect to time or frequency,  $x$  is the time or frequency sample location, and  $\mu$  is the mean. Figure 2.9a illustrates the relationship between time-standard deviations and center frequency for the three wavelet types of interest and Figure 2.9b shows the uncertainty product  $\Delta t \cdot \Delta f$  versus center frequency.

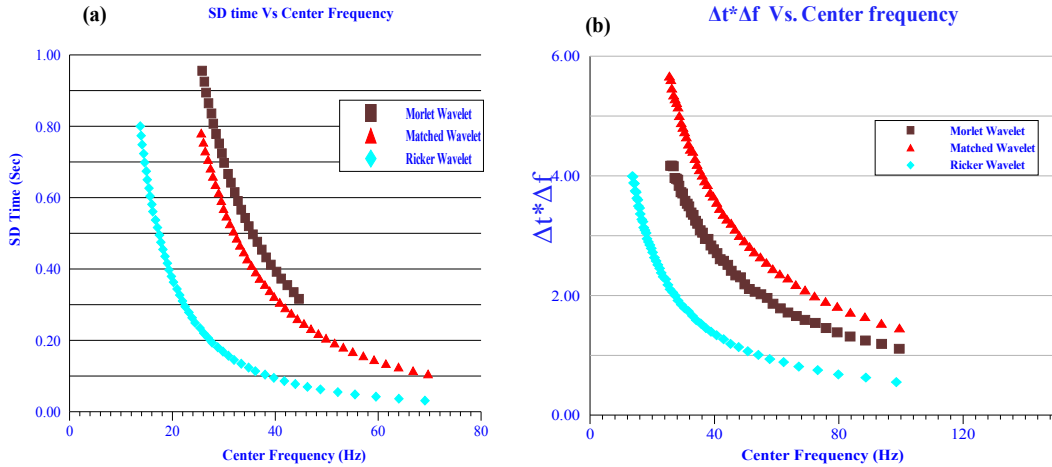


Figure 2.9 (a) The standard deviation in time versus the center frequency. (b) The uncertainty product  $\Delta t * \Delta f$  versus the center frequency.

We observe a trend for all three wavelets, that as the center frequency increases, corresponding to a higher frequency standard deviation, there is a decrease in the time standard deviation and vice versa. We observe that the Ricker wavelets have the best time resolution of the three wavelets, which agrees with the observation that the Ricker wavelet is more compact in time than the Morlet wavelet in synthetic seismic data plots. This result does not contradict the observation that a wavelet matched to the signal produces higher resolution in time-frequency space than standard wavelets because the results strictly address the time-frequency characteristics of the wavelet itself. Spectral decomposition using the wavelet transform is similar to convolution; a mother wavelet that “looks” like a signal of interest will yield optimal coefficients.

The methodology described in this chapter for wavelet synthesis provides a mechanism to create an orthonormal basis that is suitable to match a signal of interest. The primary features of the seismic signal can be captured with a matching wavelet that preserves the temporal relationships of the features. However, to achieve an exact wavelet match to the signal of interest, the signal must be orthonormal. Meyer’s wavelet is an example of an

orthonormal signal that can be exactly matched to a wavelet using the proposed algorithm (Chapa, 2000). The seismic signal is not orthonormal; hence an exact match cannot be expected. However, an exact match to the seismic signal might not be necessary because the wavelet itself is used to decompose the signal into different frequencies. For a matched wavelet, we expect that the signal energy can be captured in a narrow frequency band. The discrete solution for the matched wavelet spectrum is identical to that of the continuous solution at the sampled frequencies according to Equations 2.15. By increasing the number of Fourier coefficients and the number of sampled frequencies, the accuracy of the calculations increases. However, the computation time also increases. We observe that the matched wavelet includes ripples at the baseline of the seismic signal. These ripples are the result of using hard cutoffs of the rectangular function to obtain the necessary pass band. This problem can be mitigated by using a window function such as the Hanning or Gaussian window. Furthermore, there are precision errors in the matrix calculation. The matched wavelet technique requires further testing to gauge its performance in extracting seismic features and detecting artifacts in noisy seismic signals.

## **2.10 Conclusions**

In this chapter, I have developed methods for estimating orthogonal wavelets that are matched to a given signal in the least squares sense. Although the method of matching wavelets to a desired signal was derived from the constraint condition of orthonormal multi-resolution analysis (OMRA) using scaling factor of 2, it can also be generalized to an M-band wavelet system. We applied the method to extract a matched wavelet from a

carefully designed synthetic seismic trace and applied it as a mother wavelet to decompose the signal into the time-frequency domain using the hybrid wavelet transform. The results show that the matched wavelets discriminate features in complex signals better than standard wavelets, such as Morlet wavelets (Chui, 1992) and Ricker wavelet, which are commonly used in applied geophysics.

## **CHAPTER 3**

### **A hybrid wavelet transform based on CWT and non-linear transform**

#### **3.1 Summary**

A high-resolution approach to estimate time-frequency spectral and associated amplitudes through the use of combination of continuous wavelet transform (CWT) with a non-linear transform is presented. This is a two-step procedure in which one dimension seismic trace is first decomposed into two dimensions of time frequency domain by continuous wavelet transform, followed by the morphological top-hat transforms which has been widely used to enhance and detect the weak signal in image process areas. This combinational use of the CWT and a nonlinear transform is termed the hybrid wavelet transform (HWT). A synthetic seismic signal and field data are provided to demonstrate the performance of the hybrid wavelet transforms for high-resolution time-frequency decomposition as well as instantaneous amplitude estimation. The results show that the new method provides the high time and frequency resolution when compared to the smoothed continuous wavelet transform. When combined with conventional wavelet analysis and image-filtering techniques, the HWT provides an integrated, versatile, and efficient approach for analyzing non-stationary seismic signals with promising results as applied to the seismic attributes extraction and reservoir feature detection.

#### **2.2 Introduction**

Generally, seismic traces are statistically non-stationary. Although periodic wavelet features can dominate the time series, these signals exhibit statistical variation in amplitude and frequency over time. Wavelet methods can be used to decompose the time series into the time-frequency domain. The continuous wavelet transform time-frequency

decomposition method has become a useful tool in seismic data processing (Chakraborty and Okaya, 1995), and in recent years, has been widely applied to the analysis of the frequency content of seismic signals, mapping of channel deposits, and detection of gas by mapping low-frequency anomalies beneath the reservoir (Kazemeini, 2009), providing an effective means of quantifying non-stationary seismic signals. The complex continuous wavelet transform (CWT) yields information on both the amplitude and phase of seismic signals (Sinha, et al., 2005); the phase spectrum can highlight discontinuities such as faults. The Heisenberg Uncertainty Principle states that we cannot simultaneously optimize both time and frequency resolution (Mallat, 1999; Morlet, et al., 1982). In order to obtain optimal frequency resolution in the time-frequency analysis, we have to sacrifice temporal resolution. The CWT utilizes a wavelet dictionary to generate a highly redundant representation of the signal in the frequency domain (i.e. the filtered spectra are not independent); the redundancy is augmented at higher frequencies. Because of this effect, the CWT cannot simultaneously yield optimal time and frequency resolution; instead, it provides optimal frequency resolution at low frequencies and optimal time resolution at high frequencies. However, we can minimize this shortcoming by implementing a combination of the continuous wavelet transform and the morphological top hat nonlinear localization transform.

In this chapter, I will introduce a time-frequency decomposition method that incorporates two steps to analyze the seismic data. The first step is to process the one-dimensional seismic data by the continuous wavelet transform, yielding two-dimensional time-frequency components related to the choice of wavelet dictionary members (basis); I expand the data using a basis derived from the data. The second step is to apply the

morphological top-hat non-linear localization transform to isolate and extract the local peak energy in the time-frequency domain. The hybrid wavelet transform yields a high-resolution time-frequency distribution, enabling precise location and discrimination of reflectors. These characteristics of the hybrid wavelet transform spectral decomposition method substantially enhance the utility of spectral analysis for reservoir characterization and attenuation measurement.

### **3.3 Continuous wavelet transform (CWT) and time-frequency decomposition**

The continuous wavelet transform (CWT) is a time-frequency analysis method, which differs from the traditional Short-Time Fourier Transform (STFT). The STFT uses a constant window size and slides along in time, computing the FFT at each time using only the data within the window. Utilization of this method mitigates the frequency localization problem, but the result is still dependent on the window size used. The primary problem with the STFT is the inconsistent treatment of different frequencies: at low frequencies there are so few periods within the window that frequency localization is lost, while at high frequencies there are so many periods that time localization is lost. The continuous wavelet transform corrects this inconsistency by utilizing a variable window length that is related to the scale of observation (frequency); this flexibility allows for the isolation of high-frequency features. Another important difference between the STFT and the CWT is the fact that the CWT is not limited to the use of sinusoidal basis functions. Rather, a wide selection of localized waveforms can be utilized provided they satisfy pre-defined mathematical criterion (3.3). The wavelet transform of a continuous time signal,  $f(x)$ , is defined as:

$$W_{\psi}(s, \tau) = \int_{-\infty}^{\infty} f(x)\psi_{s,\tau}(x)dx , \quad (3.1)$$

where  $\psi_{s,\tau}(x) = \frac{1}{\sqrt{s}}\psi\left(\frac{x-\tau}{s}\right)$ ,  $s$  and  $\tau$  are called scale and translation parameters, respectively. Given  $W_\psi(s, \tau)$ ,  $f(x)$  can be obtained using the inverse continuous wavelet transform :

$$f(x) = \frac{1}{C_\psi} \int \int_{-\infty}^{\infty} W_\psi(s, \tau) \frac{\psi_{s,\tau}(x)}{s^2} d\tau ds \quad , \quad (3.2)$$

where 
$$C_\psi = \int_{-\infty}^{\infty} \frac{|\Psi(u)|^2}{|u|} du \quad . \quad (3.3)$$

$\Psi(u)$  is the Fourier transform of  $\psi(x)$ ,  $C_\psi$  is known as the admissibility criterion.

We implement the wavelet transform by computing a convolution of the seismic trace with the members of a scaled wavelet dictionary. The relative contribution to the total energy contained within the signal at a specific scale is given by the scale-dependent energy distribution:

$$E(s) = \frac{1}{C_\psi} \int_{-\infty}^{\infty} |W_\psi(s, \tau)|^2 d\tau \quad . \quad (3.4)$$

Peaks in  $E(s)$  highlight the dominant energetic scales within the signal. The different wavelets we choose will control the time and frequency resolution. The Morlet wavelet, which is the most popular complex wavelet used in practice, is very well localized in the frequency domain.

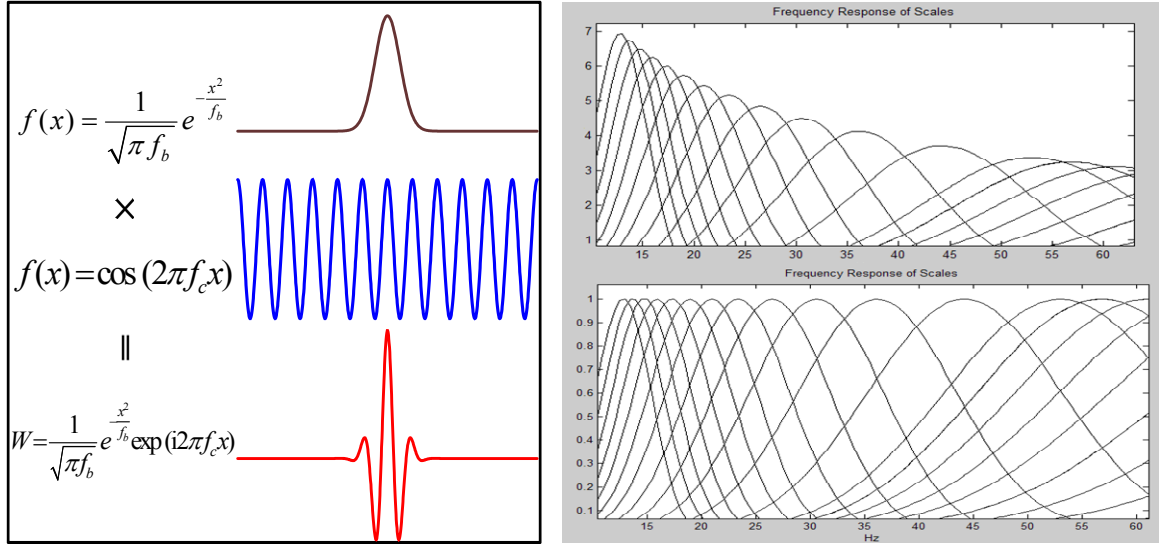


Figure 3.1 Construction of the Morlet wavelet as a cosine curve modulated by a Gaussian in the time domain (left) and its dictionary in the frequency domain (right up) and after normalization (right down).

The Morlet wavelet response pairs in the time and frequency domains are:

$$g_j(t) = \exp(-a_j t^2) \exp(iw_j t) \quad (3.5)$$

$$G_j(w) = \int_{-\infty}^{\infty} g_j(t) \exp(iwt) dt = \sqrt{\frac{\pi}{a_j}} \cdot \exp\left(\frac{-(w-w_j)^2}{4a_j}\right) \quad (3.6)$$

where  $a_j$  is scale. We may choose  $a_j = \frac{\ln 2}{4\pi^2} \omega_j^2$  and design narrow band filters (see

Figure 3.1) that constitute the wavelet dictionary.

### 3.4 Converting scale to frequency

We convert the scale-dependent wavelet energy spectrum of the signal,  $E(s)$ , to a frequency-dependent wavelet energy-spectrum in order to analyze the Fourier energy spectrum of the signal. To do this, we must convert from the wavelet a scale to a

characteristic frequency of the wavelet such as the spectral peak frequency or the pass-band central frequency (Figure 3.2). The frequency associated with a wavelet of arbitrary scale is given by:

$$F_s = \frac{F_c}{S \cdot \Delta} \quad , \quad (3.7)$$

where  $S$  is the scale,  $\Delta$  is the sampling period, and  $F_c$  is the center frequency of the wavelet. The calculated frequency  $F_s$  is called the pseudo-frequency with units in Hz. In practice, a fine discretization of the CWT is computed wherein the  $\tau$  location is discretized at the sampling interval and the scale is discretized logarithmically.

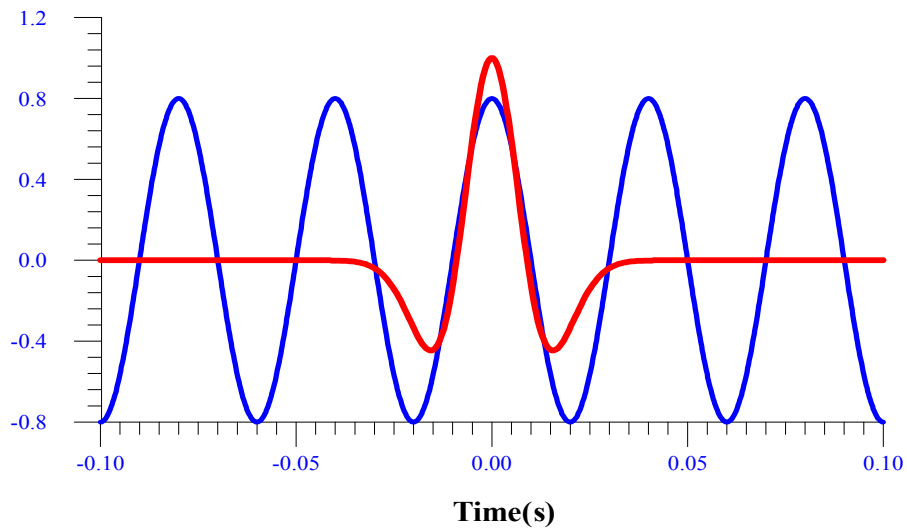


Figure 3.2 The center frequency of a Ricker wavelet (red line) is approximated by matching to the function  $\cos(2\pi f_c t)$  (blue line).  $f_c = 25\text{Hz}$  provides the best fit and is taken as the center frequency of the wavelet.

### 3.5 Example of wavelet analysis to the synthetic data

We use a synthetic seismic signal in order to study the time-localization properties of CWT methods. Figure 3.3a shows the synthetic trace generated by the wave propagation

equation of Ricker wavelets with center frequency equal to 20Hz, 40Hz, 55Hz, and 70 Hz respectively. Intrinsic attenuation was also accounted for in the synthetic data by varying the quality factor Q. As we vary the wavelet center frequency, we observe that the amplitude of the signal decreases and the wavelets are lengthened in time. The synthetic trace is a superposition of the four different traces shown in Figure 3.3a.

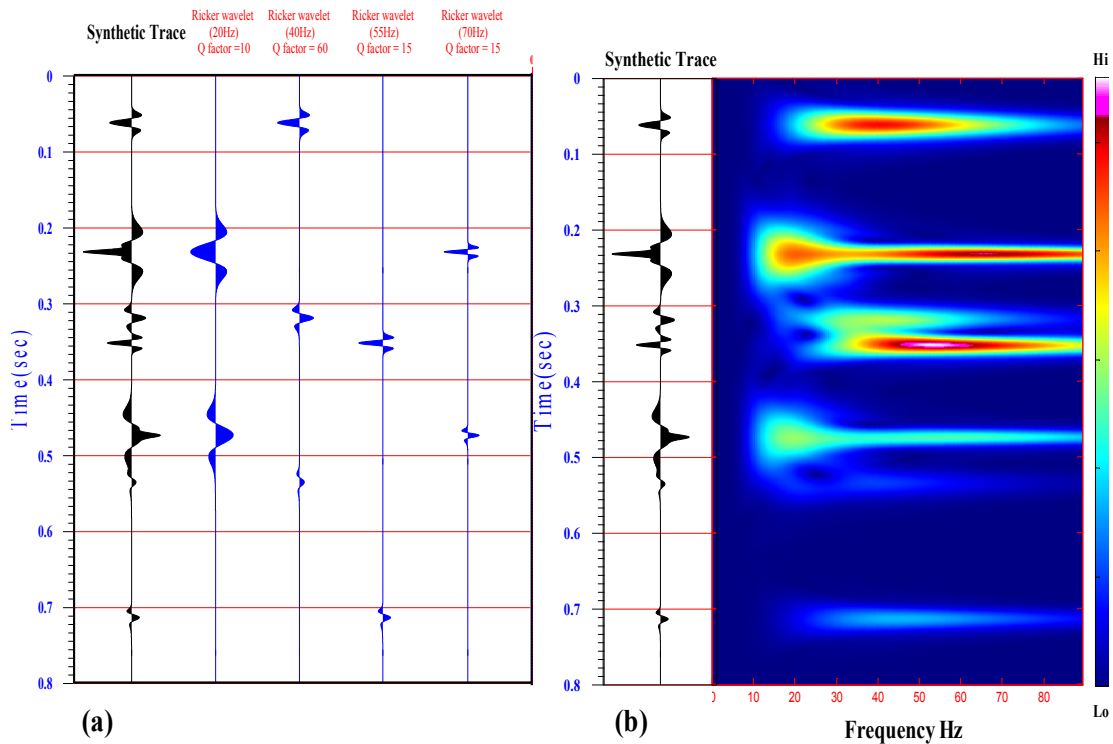


Figure 3.3 (a) Synthetic trace comprised of Ricker wavelets with different center frequencies, wave propagation attenuation was included. (b) Time-frequency distribution of synthetic trace by the continuous wavelet transforms.

The Figure 3.3b shows time-frequency analysis for a synthetic trace by continuous wavelet transform. The first seismic event at approximately 50 milliseconds with a center frequency of 40 Hz is isolated at the location of peak energy on the CWP output, the energy of the second seismic event near 230 milliseconds, which consists of a 20 Hz wavelet and 70 Hz wavelet arriving simultaneously is distributed from 14 Hz to 80 Hz.

Although there are two peak energies at 20 and 70 Hz, they overlap and could not be clearly resolved. Similar results were shown for the event near 470 milliseconds. The events near 320, 350, and 710 milliseconds can be identified in the frequency domain using individual peak energy locations. Note also that the event near 530 milliseconds is nearly invisible in the frequency domain due to its relatively weak energy content compared to the previous events.

Because of the increased redundancy at higher frequencies and the variable window length, the CWT cannot provide optimal time and frequency resolution simultaneously. Instead, it yields good time resolution and poor frequency resolution at high frequencies and good frequency resolution and poor time resolution at low frequencies. Furthermore, for reservoir characterization applications, we are more interested in the spectral characteristics of individual reflectors than composite windowed responses (measuring attenuation for example); best results are achieved if the reflector of interest is isolated by the decomposition method. In order to achieve this optimization, we target the local spectral energy rather than the more global spectral energy distribution given by Fourier transform. We achieve this by applying a combination of the continuous wavelet transform with a nonlinear transform to extract the local extreme value. This hybrid wavelet transform can provide better time and frequency resolution and more accurate amplitude estimates as compared to conventional continuous wavelet transform. The top-hat transform is a nonlinear transform used in digital signal processing to extract the local extreme value. Using binary logical operations, the top-hat transform can be implemented much more efficiently and faster than conventional methods to find local extreme values.

### 3.6 The morphological top-hat transforms

Image morphology includes a broad set of image-processing operations that process images based on shapes. Morphological operations apply a structuring element to an input image, creating an output image that is the same size as the input images (Gonzales, 2002). The most basic morphological operations are dilation and erosion. Dilation adds pixels to the boundaries of objects in an image, while erosion removes pixels on object boundaries. The number of pixels added or removed from the objects in an image depends on the size and shape of the structuring element used to process the image. Mathematically, dilation is defined in terms of set operations. With A and B as sets in  $Z^2$ , the dilation of A by B, denoted  $A \oplus B$ , is defined as :

$$A \oplus B(s, t) = \min \{ A(s+x, t+y) - B(x, y) \mid (s+x), (t+y) \in D_x; (x, y) \in D_b \} , \quad (3.8)$$

where A is object and B is the reflection of the structuring element,  $A, B \in Z$ , and  $D_x$  and  $D_b$  are the domains of A and B. The definition of erosion is similar to that of dilation.

The erosion of A by B, denoted  $A \ominus B$ , is defined as :

$$A \ominus B(s, t) = \max \{ A(s-x, t-y) + B(x, y) \mid s-x, t-y \in D_x; (x, y) \in D_b \} . \quad (3.9)$$

Figure 3.4 shows a simple set A with length d in the left of picture. A reflection of structuring element is in the middle. In this case the structuring element and its reflection are equal because B is symmetric with respect to its origin. The dashed line on the right shows the original set for reference, and the solid line shows the limit beyond which any further displacements of the origin  $\hat{B}$  by z would cause the intersection of  $\hat{B}$  and A to be empty. Therefore, all points inside the boundary constitute the dilation of A by B.

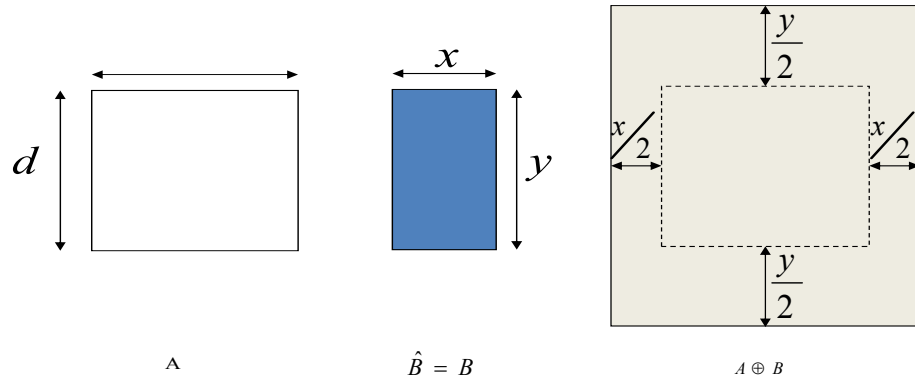


Figure 3.4 Morphological dilation of an image

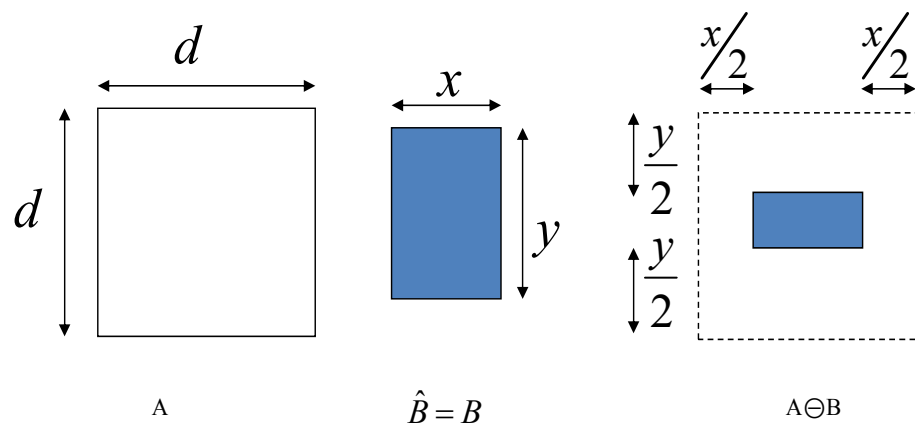


Figure 3.5 Morphological erosion of an image

Figure 3.5 illustrates erosion, which is the opposite of dilation and is a process similar to the Figure 3.4. As before, set A is shown as a dashed line for reference in the right of the picture. The boundary of the shaded region shows the limit beyond which further displacement of the origin of B would cause this set to cease being completely contained in A. Thus, the locus of points within this boundary (i.e., the shaded region) constitutes the erosion of A by B. In practical application, dilation and erosion are used most often in various combinations as opening and closing in morphological operations. The opening of set A by structuring element B, denoted  $A \circ B$ , is defined as :

$$A \circ B = (A \ominus B) \oplus B. \quad (3.10)$$

Thus, the opening  $A$  by  $B$  is the erosion of  $A$  by  $B$ , followed by a dilation of results  $B$ . similarly, the closing of  $A$  by structuring element  $B$ , denoted  $A \bullet B$ , is defined as :

$$A \bullet B = (A \oplus B) \ominus B . \quad (3.11)$$

The closing of  $A$  by  $B$  is simply the dilation of  $A$  by structuring element  $B$ , followed by the erosion of the result by  $B$ .

Opening and closing of images have a simple geometrical interpretation. Suppose that we view an image function  $f(x, y)$  from 3D perspective (like a relief map), and open  $f$  by a spherical structuring element  $b$ , viewing this element as a "rolling ball". Then the mechanics of opening  $f$  by  $b$  may be interpreted geometrically as the process of pushing the ball against the underside of the surface, while at the same time rolling it so that the

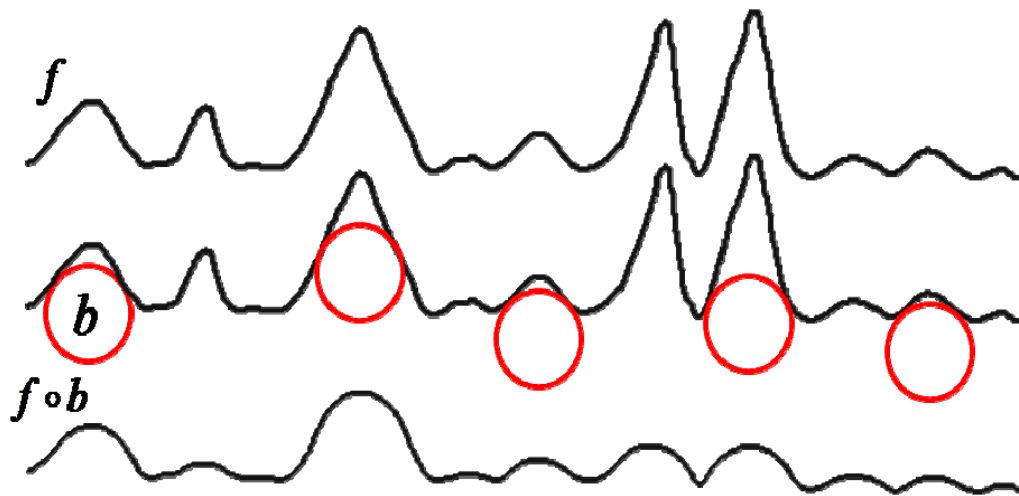


Figure 3.6 (Top, a) a scan line of function. (Middle, b) positions of rolling ball for opening. (Bottom,c) Results of opening.

entire underside of the surface is traversed. The opening  $f \circ b$ , is then the surface defining the highest points reached by any part of the sphere as it slides over the entire undersurface of  $f$ . Figure 3.6 illustrates this concept. Figure 3.6a illustrates a 1D scan line as a continuous function  $f(x)$  in the top of the figure. Figure 3.6b illustrates the

rolling ball in various positions on the undersurface of  $f$ , and Figure 3.6c illustrates the result of opening  $f$  by  $b$  along the scan line. The peaks that are narrow with respect to the diameter of the ball are reduced in amplitude and sharpness. In practical applications, opening operations are usually applied to remove small local details, while leaving the overall more extensive features relatively intact. For local extremum value extraction, we apply the morphological top-hat transform to remove the background signal and extract the regional maximum value. The morphological top-hat transform is defined as :

$$h = f - (f \circ b) = f - (f \square b) \oplus b \quad , \quad (3.12)$$

where,  $f$  is the input function and  $b$  is the structuring element function. This transformation is often used to extract the local extreme value and enhancing detail in the presence of shading. Figure 3.7 illustrates the result of performing a top-hat transformation on a function. Note the enhancement in the second peak at which the value is relatively weak. The top-hat transform provides more robust results than can be obtained using traditional threshold method that utilize a global threshold function.

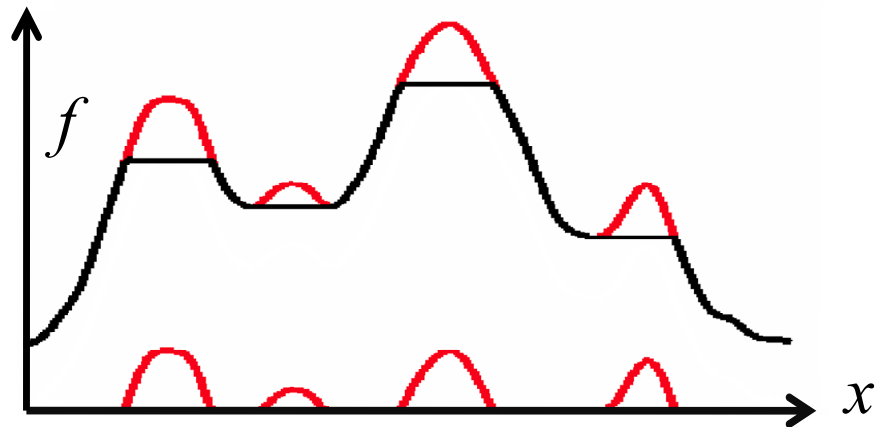


Figure 3.7 Top-hat transforms to extract local extreme value, the above line is a function containing the local maxima (red line segments), and the lower part is the top hat transform results.

we can show that this process is equivalent to a thresholding function  $f(x, y)$  with a locally varying threshold function  $T(x, y)$ ,

$$h(x, y) = \{1 \text{ if } f(x, y) \geq T(x, y) \text{ or } 0 \text{ if } f(x, y) < T(x, y)\} \quad (3.13)$$

where  $T(x, y) = f_0(x, y) + T_0$ . The function  $f_0(x, y)$  is the morphological opening of  $f$ , and the constant  $T_0$  is the result of the application of thresholding function applied to  $f_0$ .

We provide an example of utilizing the top-hat transform to identify local extreme value locations. The matrix A contains two primary regional maxima, 13 and 18, and several smaller maxima of 11. The top-hat transform returns a binary logical matrix that identify the locations of the regional maxima.

A=

10	10	10	10	10	10	10	10	10	10
10	13	13	13	10	10	11	10	11	10
10	13	13	13	10	10	10	11	10	10
10	13	13	13	10	10	11	10	11	10
10	10	10	10	10	10	10	10	10	10
10	11	10	10	10	18	18	18	10	10
10	10	10	11	10	18	18	18	10	10
10	10	11	10	10	18	18	18	10	10
10	11	10	11	10	10	10	10	10	10
10	10	10	10	10	10	11	10	10	10

A=

0	0	0	0	0	0	0	0	0	0
0	1	1	1	0	0	1	0	1	0
0	1	1	1	0	0	0	1	0	0
0	1	1	1	0	0	1	0	1	0
0	0	0	0	0	0	0	0	0	0
0	1	0	0	0	1	1	1	0	0
0	0	0	1	0	1	1	1	0	0
0	0	1	0	0	1	1	1	0	0
0	1	0	1	0	0	0	0	0	0
0	0	0	0	0	0	1	0	0	0

Figure 3.8. (top) A matrix A with local values, (bottom) the locations of the regional maximum are marked by the top-hat transform

### **3.7 Combination of CWT and top-hat transform**

The CWT is a tool for analyzing the signal at different frequencies with different resolutions. It is designed to yield good time resolution and poor frequency resolution at high frequencies and does not allow the localization of relatively weak high-frequency waves due to their low amplitudes. In order to minimize the time-frequency resolution tradeoff effect previously described, we combine the CWT with the top-hat transform to extract transients with an inflection point corresponding to a local wave peak and to enhance the energy of relatively weak wave peaks. Local maxima of the signal are extracted by means of the top-hat transform isolating the time location of these transients. The proposed method includes two main steps. The first one is based on the continuous wavelet transform applied on each trace of the seismic data to obtain the multi-frequency components of the coefficients of the wavelet transform at successive frequency. We use a wavelet which has matched to a signal of interest to decompose the signal into a time-frequency domain through the continuous wavelet transform because the matched wavelets can discriminate various features in complex signals better than standard wavelets (Chapa and Rao, 2000). The second step includes a morphological top-hat algorithm which localizes the maxima energy of frequency location corresponding to the temporal position. After top-hat transform, the results may contain noise along the edges of the local peak zones. To eliminate this noise, a median filter is used after top-hat operation. The workflow is summarized in Figure 3.9.

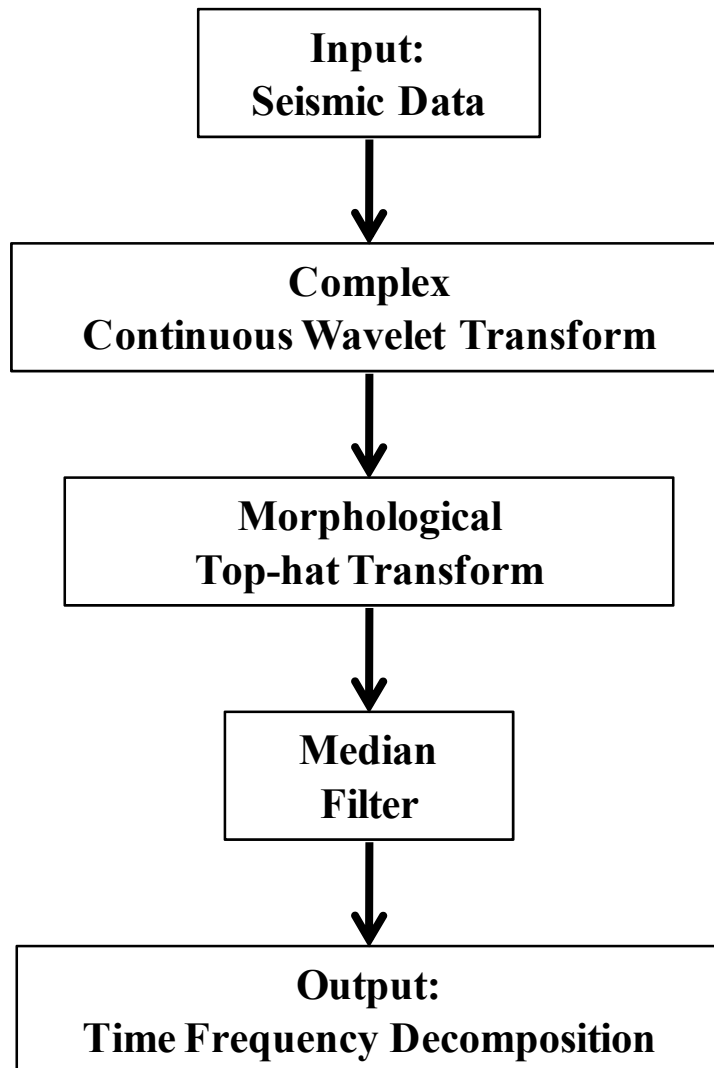


Figure 3.9 The flowchart for spectral decomposition using the hybrid wavelet transform.

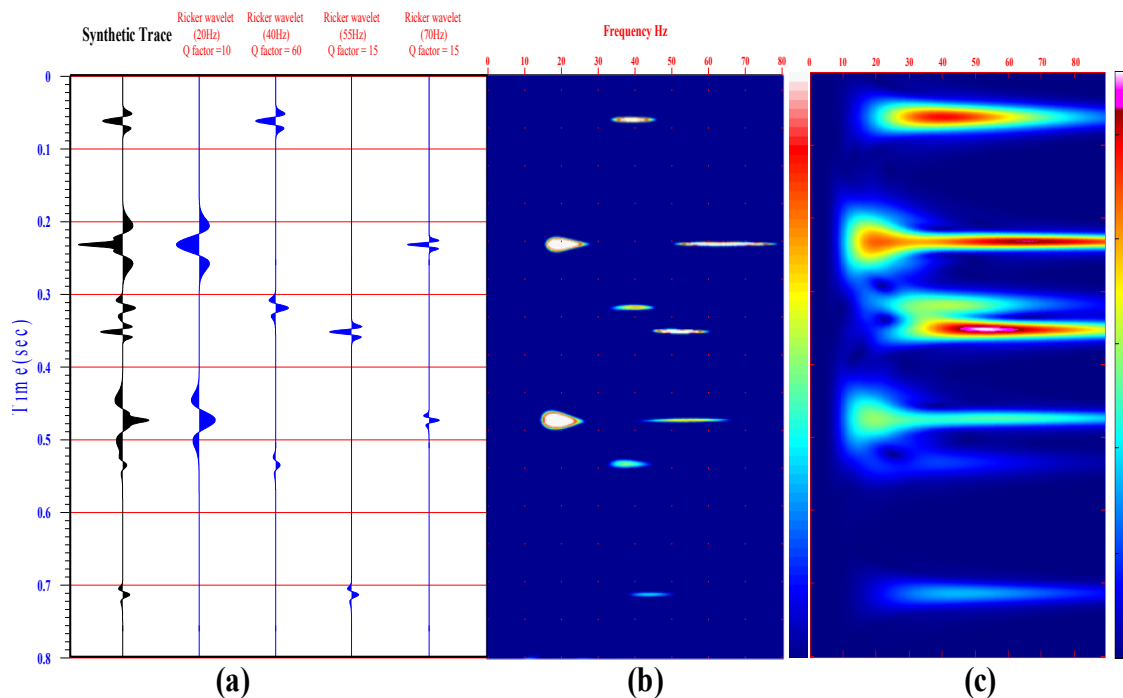


Figure 3.10 Comparison of results of application of spectral decomposition to a (a) synthetic seismic trace using (b) the hybrid wavelet transform and (c) continuous wavelet transform.

The middle plot of Figure 3.10 shows the result of time-frequency decomposition of a synthetic seismic trace by using the hybrid wavelet transform. The frequency content of the different events is sharply defined in the resulting frequency-domain plot. Specifically, two events near 230 milliseconds and 470 milliseconds, illuminated by wavelets with two different center frequencies, that failed to separate by direct application of the continuous wavelet transform, are split by the new decomposition method HWT. Note that the weak event near 530 milliseconds is also highlighted in the corresponding frequency section. In the time-frequency plane, a clear downward shift in the center frequency of the trace with time is evident as a result of wavelet attenuation. It

can be found that the event with center frequency 40Hz Ricker wavelet at time 55 milliseconds, its peak frequency shifts down to 36Hz as it travels to 318 milliseconds, to 34 Hz as it propagates to 535 milliseconds.

To reconstruct the signal back, the inverse continuous wavelet transform is used to take the energy in time-frequency domain and transform it back into time domain.

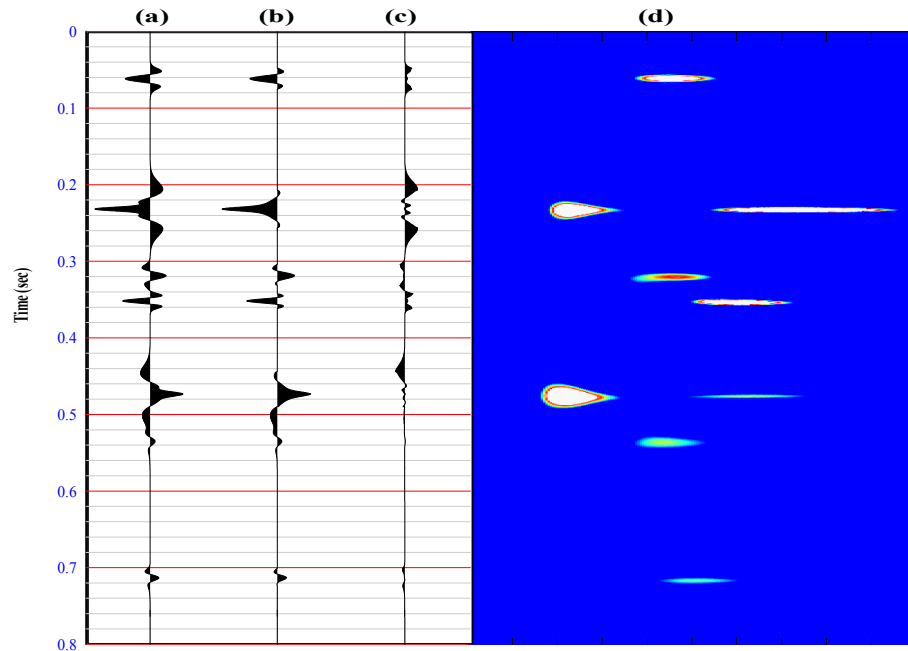


Figure3.11. (a) is an original synthetic trace. (b) is an reconstruction of the signal by using HWT results. (c) is a residual between the original and reconstructed signal. (d) is the time frequency spectral of HWT.

Figure 3.11 demonstrates the inverse CWT use the result of hybrid wavelet transform of synthetic trace. The signal is almost reconstructed by using a partial values in the transform domain (i.e., have magnitude above a certain thresholds). Some low-frequency signals are lost for trade off providing good time resolution in time series by HWT.

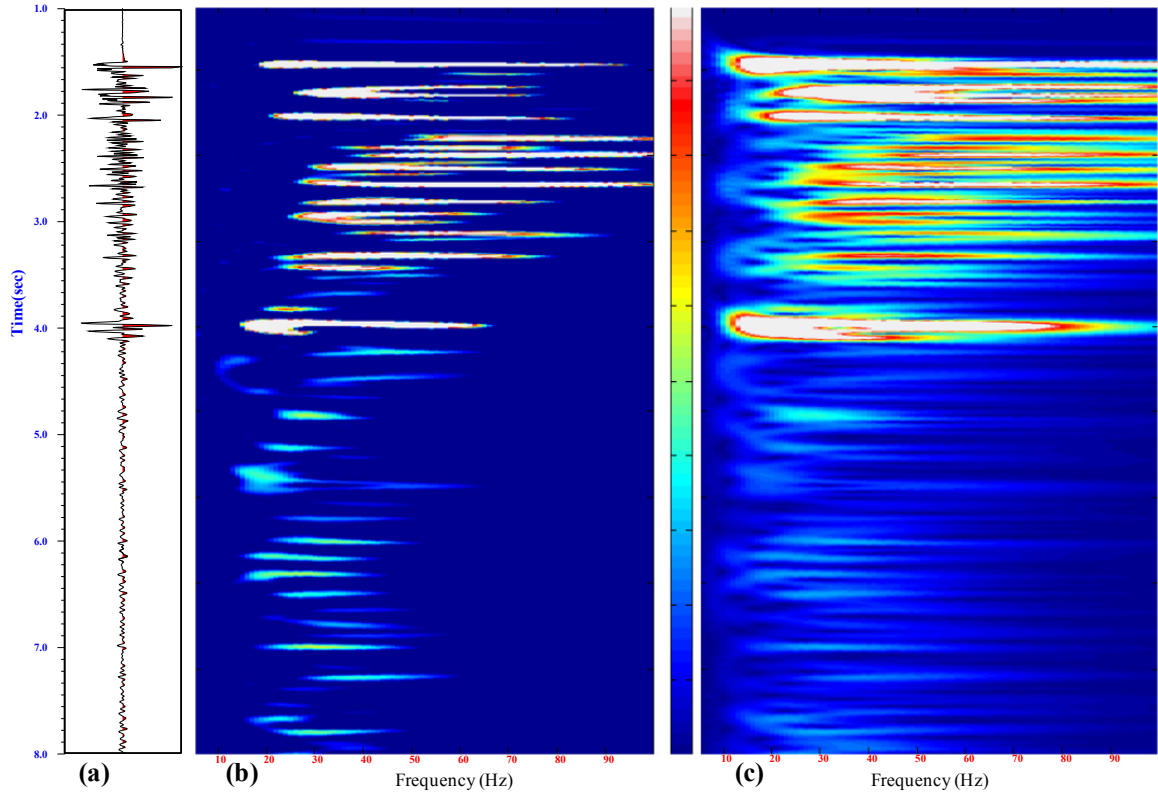


Figure 3.12 Comparison of results of application of spectral decomposition to a (a) real seismic trace using (b) the hybrid wavelet transform and (c) continuous wavelet transform.

Figure 3.12 shows the frequency gather of a real seismic trace using the CWT and HWT. Clearly the HWT yields superior resolution to the CWT method. The results of the HWT are sharper and more focused than are those of the simple CWT. In the result of the new method, the energy of events is clearly isolated from low frequency to high frequency, whereas they are merged in the CWT result, producing a spuriously continuous energy distribution extending from the low- to high- frequency range. The shift from high frequencies in shallow layers to low frequencies in deep layers highlights the attenuation affect as the seismic wave propagates from shallow to deep geology.

### 3.8 Discussions

Unlike Fourier analysis, wavelet-transform-based spectral decomposition can be implemented using a non-unique process or a non-unique basis; thus a single seismic trace can produce different time-frequency character analysis (Castagna and Sun, 2006).

The wavelet we choose can significantly influence the time and frequency resolution of the result. In signal feature detection and pattern recognition, the time-frequency decomposition of a signal in the presence of noise using a wavelet matched to the signal produces a better resolved image as compared to conventional unmatched wavelets. The seismic signal is a complicated signal having low amplitudes, making it difficult to analyze. However, the signal properties of seismic data can be enhanced by the use of matched wavelets, which performs the much closer analysis of the signal. The method to extract matched wavelet described in the previous chapter is based on discrete wavelet transform (DWT); but, the wavelet transform of signal with DWT accepts only integer scale values. DWT cannot provide analysis band with any arbitrary fine frequency sampling. The continuous wavelet transform (CWT) still uses discretely sampled data; however the shifting process is a smooth operation across the length of the sampled data, and the scaling (frequency) can be defined from the minimum (original signal frequency) to a maximum chosen by the user, thus giving a much finer frequency intervals.

For signals corrupted by strong background noise, it is usually very difficult to perform signal detection and parameter estimation in either the time domain or the frequency domain. But, they may be identified in the joint time-frequency domain by taking wavelet transform (Victor, 2002). Signal often concentrates its energy within a limited time and a limited frequency band; while random noise typically has energy spread over the time-

frequency plane. By combining the wavelet scheme, which represents the signal and noise in the time-frequency domain, with the mathematical morphology scheme, which separates the signal coefficients from the noise coefficients by using an appropriate thresholding, signal detection and recognition become much easier. However, some interesting maxima corresponding to singularities are difficult to pick up from the data which have very low value. This is because relevant wavelet coefficients are embedded into non-specific background. Maxima which are difficult to locate are also difficult to characterize by wavelet-modulus maxima (Mallat and Hwang, 1992; Bouyahia, 2009). This makes top-hat algorithm detection and characterization become a very difficult task if use a fixed thresholding in the formula (3.13). To overcome this problem, we use regional thresholding or local thresholding to implement the hot-hat algorithm. Local thresholding depends on the data histogram, local statistics such as mean and standard deviation, or the local gradient.

### **3.9 Conclusions**

In this chapter we presented and developed wavelet-based techniques for high-resolution time-frequency decomposition from seismic data. Wavelet-based time-frequency decomposition is a straightforward transform with low computational complexity compared to matching pursuit for time-frequency decomposition which is an adaptive but expensive iterative approach. This is a two-step procedure which utilizes the continuous wavelet transform to obtain two dimensional time-frequency spectral of the signal, followed by the morphological top-hat transforms to extract maxima associated with only the specific frequencies of interest. This combinational use of the CWT and a nonlinear

transform is referred to herein as the hybrid wavelet transform (HWT). A synthetic seismic signal and field data are provided to demonstrate the performance of the hybrid wavelet transforms for high-resolution time-frequency decomposition as well as instantaneous amplitude estimation. The results show that the new method provides the high time and frequency resolution when compared to the smoothed continuous wavelet transform. Combined with conventional wavelet analysis and image-filtering techniques, the HWT offers an integrated, versatile, and efficient approach for analyzing non-stationary seismic signals with promising results when applied to the seismic attributes extraction and reservoir feature detection.

## CHAPTER 4

### Attenuation estimation with continuous wavelet transforms

#### 4.1 Summary

The spectral ratio method is a popular means of measuring seismic attenuation. As ratios are particularly sensitive to noise and spectral errors, the precise estimation of the signal spectrum is a key to making robust attenuation measurements. The spectrum of the signal may be affected by many factors, for example, thin bed influences (Hackert et al., 2004), interbed multiples and other noise, and windowing. Seismic attenuation measurements from surface seismic data using spectral ratios are particularly sensitive to inaccurate spectral estimation. Spectral ratios of Fourier spectral estimates are subject to inaccuracies due to windowing effects, noise, and spectral nulls caused by interfering reflectors. We have found that spectral ratios obtained using continuous wavelet transforms as compared to Fourier ratios are more accurate, less subject to windowing problems, and more robust in the presence of noise, which results in a more robust and effective means of estimating  $Q$ .

#### 4.2 Introduction

It is common practice to express seismic attenuation in terms of the quality factor ( $Q$ ). The spectral amplitude-ratio technique is a popular method of estimating  $Q$ , because it is independent of the source influence. Accurate estimation of the signal spectrum is a key to accurately determining  $Q$ . However, in practice there are many difficulties to estimate the signal spectrum correctly. First, it is almost impossible to remove the reflectivity

spectrum from the spectral estimates. This would require isolating and performing spectral estimation on reflections from two individual reflectors. However a seismic event is usually a complex superposition of many reflections. Second, the conventional spectral analysis method using Fourier Transforms temporally localized by windowing distorts the spectrum. Third, the noise spectrum will certainly cause severe degradation in the low SNR frequency range (Turner and Siggins, 1994). Wavelet time-frequency analysis provides an alternative approach to determining the local characteristics of a signal. A variety of wavelet analysis methods had been applied in the literature for estimating Q since Dr. Taner proposed doing so in 1983. James and Knight (2003) applied the S-transform to measure the centroid frequency shift to calculate Q for ground-penetrating radar data. This method can be applied to seismic reflection data in an analogous fashion.

In this chapter, we discuss the estimation of instantaneous spectral of the signal using the continuous wavelet transform (CWT) and compute Q in the time-frequency domain using spectral-ratios. We find that this method exhibits several advantages: (1) In comparison to conventional Fourier spectral estimation with wide windows, the CWT can directly determine the signal spectrum for individual events. These events may be composite signals of sub-resolution reflectors, but the severe spectral notching that characterizes wide window Fourier spectral estimation from multiple events in the window is reduced. (2) The CWT avoids smearing the spectrum as a consequence of the temporal window influence. (3) Scale-based wavelet transform filtering takes advantage of the fact that the noise due to domain boundaries is at a smaller scale than the signal due to the area of

interest. Thus, by selecting all areas at an optimal scale, noise due to the domain boundaries can be easily eliminated.

The continuous wavelet transform is a well-known approach to separating objects at different scales. Spectral ratios derived from CWT spectra are more robust in the presence of noise. We will study the effects of windowing and noise in comparing Fourier and CWT attenuation estimation on both synthetic seismograms and laboratory signals.

### 4.3 Methods

By definition, attenuation affects the amplitude spectrum of the propagating seismic wavelet and thus the resulting reflection seismogram. A spherical harmonic wave  $A(R, \omega)$  propagating in an attenuating medium can be described as:

$$A(R, \omega) = A_0(R_0, \omega)G(R)G(I)K(r)\exp(-\alpha(\omega)R)\exp(-i\omega R/V) \quad , \quad (4.1)$$

where,  $A(R, \omega)$  is the wave amplitude at a distance  $R$  from the source,  $A_0(R, \omega)$  is the amplitude at the source,  $V$  is the frequency dependent wave velocity in the medium,  $G(R)$  is geometric spreading,  $G(I)$  is instrument response, and  $K(r)$  is the loss due to reflection and transmission. The exponential term  $\exp(-\alpha(\omega)R)$  is the anelastic attenuation in the medium. The second exponential term  $\exp(-i\omega R/V)$  is a phase delay. If we assume that the attenuation coefficient  $\alpha(\omega)$  is linearly dependent upon frequency within a limited bandwidth, then  $Q$  is nearly constant over the frequency range providing the velocity dispersion is small. In reality, a seismic record contains a superposition of reflections from a great many impedance contrasts that will overlap temporally with one

another. However, suppose that we can isolate two discrete seismic events, then the spectral ratio method for estimating Q can be expressed as follows:

$$\frac{A_2(R_2, \omega)}{A_1(R_1, \omega)} = \frac{A_2(R_2, \omega)}{A_1(R_1, \omega)} = \frac{R_1}{R_2} \cdot \frac{G(I_2)}{G(I_1)} \cdot \frac{K(r_2)}{K(r_1)} \cdot \exp \alpha(\omega)(R_1 - R_2) \cdot \exp(i\omega(R_1 - R_2)) , \quad (4.2)$$

The exponential term  $\exp(i\omega(R_1 - R_2))$  is purely a time delay that does not enter into the amplitudes, and therefore it can be omitted. Then we obtain:

$$\alpha(\omega) = (R_1 - R_2)^{-1} \left\{ \log\left(\frac{A_2(R_2, \omega)}{A_1(R_1, \omega)}\right) - \log\left(\frac{R_1}{R_2}\right) - \log\left(\frac{G(I_2)}{G(I_1)}\right) - \log\left(\frac{K(r_2)}{K(r_1)}\right) \right\} = \frac{\pi f}{QV} . \quad (4.3)$$

Here we assume,

$$const = \log\left(\frac{R_1}{R_2}\right) + \log\left(\frac{G(I_2)}{G(I_1)}\right) + \log\left(\frac{K(r_2)}{K(r_1)}\right) . \quad (4.4)$$

Thus the logarithm of the ratio of the spectra of the two reflected wavelets is assumed to be a linear function of frequency whose slope will estimate Q. In particular, if reflection K is from the top of an interval containing a gas reservoir and reflection J is from the bottom of that interval, then we might hope by this method to estimate the Q value of the interval containing the reservoir.

#### 4.4 Synthetic example and application

In Q computation, we need to compute the amplitude spectral ratio of two events as shown synthetically in Figure 4.1. We used a 25 Hz Ricker wavelet as a source wavelet, a wave velocity of 3000m/s, a distance between two events of 1100m, and a constant Q of 40.

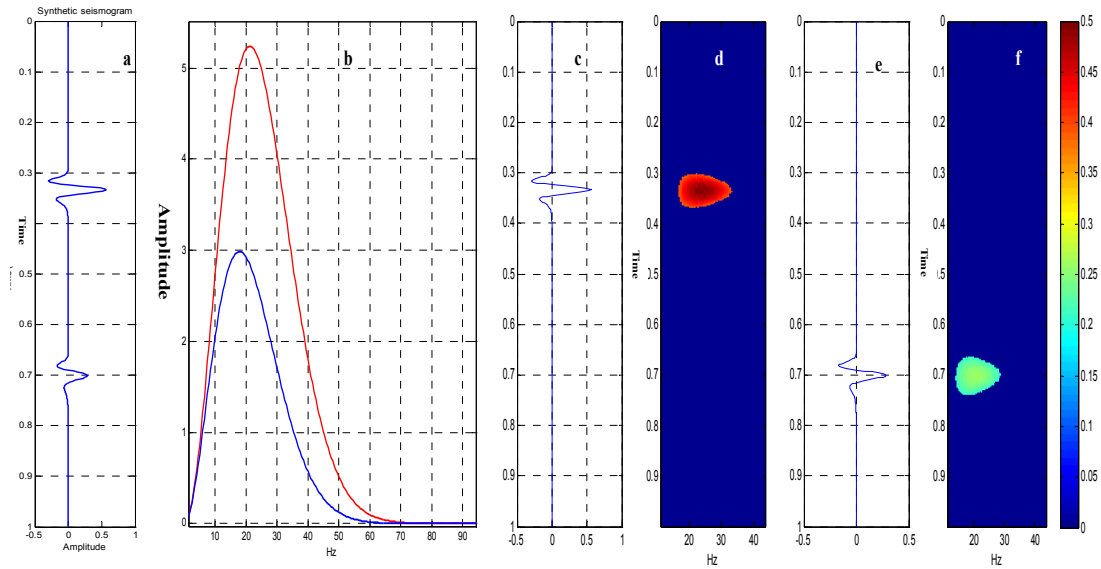


Figure 4.1 (a) and (b) are two synthetic events and their amplitude spectral, the red line is the first event and blue line is second event. (cdef) are signals and corresponding time-frequency decompositions with CWT.

Figure 4.2 shows the effect of added Gaussian noise (SNR=12 dB). The Fourier amplitude spectrum (Figure 4.2a) shows the spectral oscillation caused by noise, which influences the slope of a best-fit line and the accuracy of Q estimation. However the CWT time-frequency plot shows less oscillation due to noise (Figure 4.2c and 4.2e). Since seismic data is band limited, our calculation of amplitude spectral ratio is located within the band of the data. If we select the frequency range outside the range of the signal, the results of estimated Q value would be unreliable.

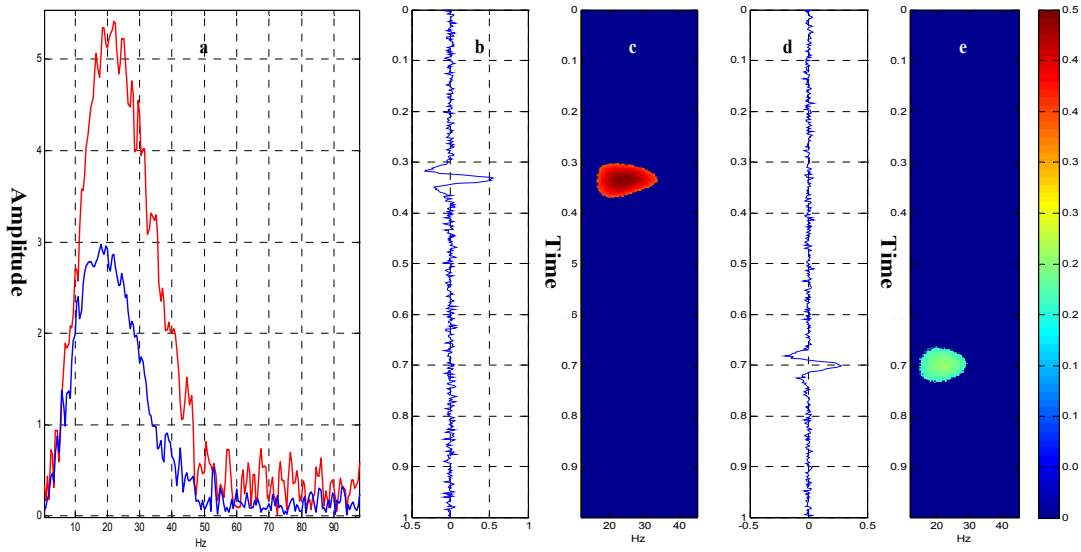


Figure 4.2 (a) is the amplitude spectra of two synthetic events with noise, the red line is the first event, and the blue line is second event. (bcde) are signals and their time-frequency decompositions with CWT.

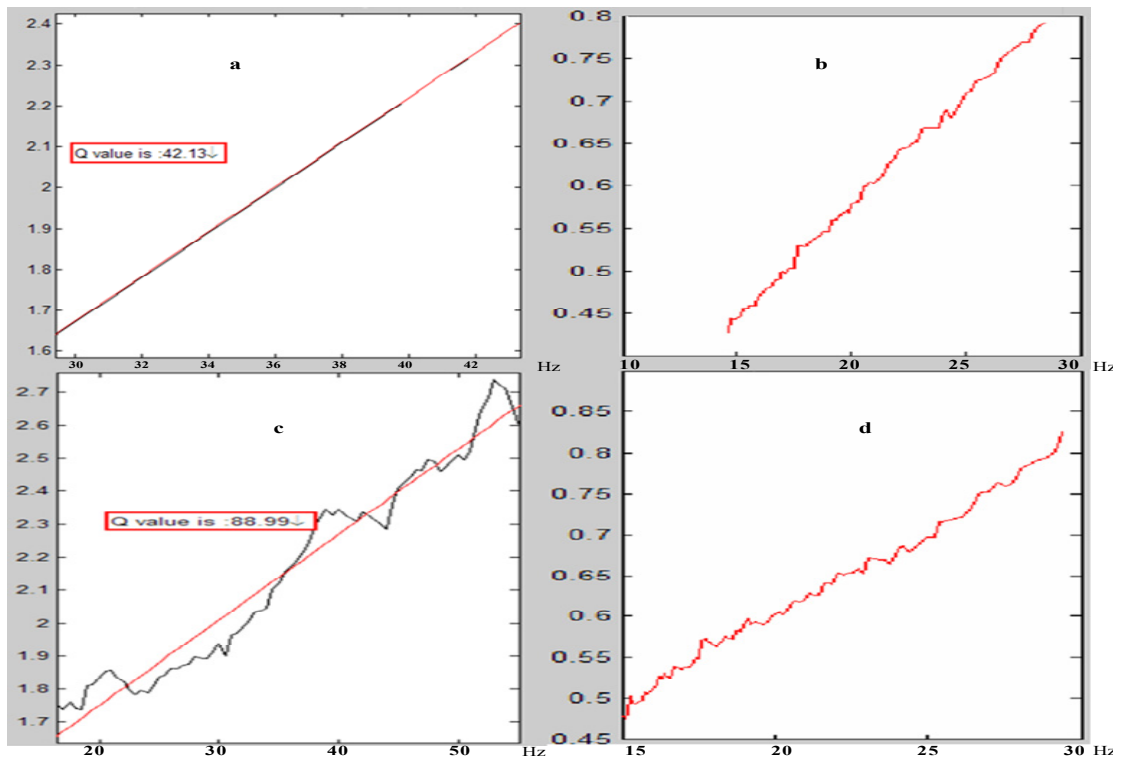


Figure 4.3 (a) is the noise-free Fourier amplitude spectral ratio compared to the correct spectral ratio  $(\ln A_1 - \ln A_2)$ . (b) is the amplitude spectral ratio line generated by CWT. (c,d) corresponding to (a) and (b) with Gaussian random noise added.

The two amplitude spectral ratio lines generated by windowed FFT and CWT respectively are shown on the Figure 4.3. Without adding noise to signal, the Q values determined by using equation (3) to be 42.13 using the FFT and 39.8 using the CWT, which is very close to the true value of  $Q=40$ . But, with noise, the FFT gives  $Q=88.99$  while the CWT spectral ratio gives  $Q=38.4$ . The large error using Fourier spectra comes from the interplay of windowing and noise. We also applied this method to estimate the

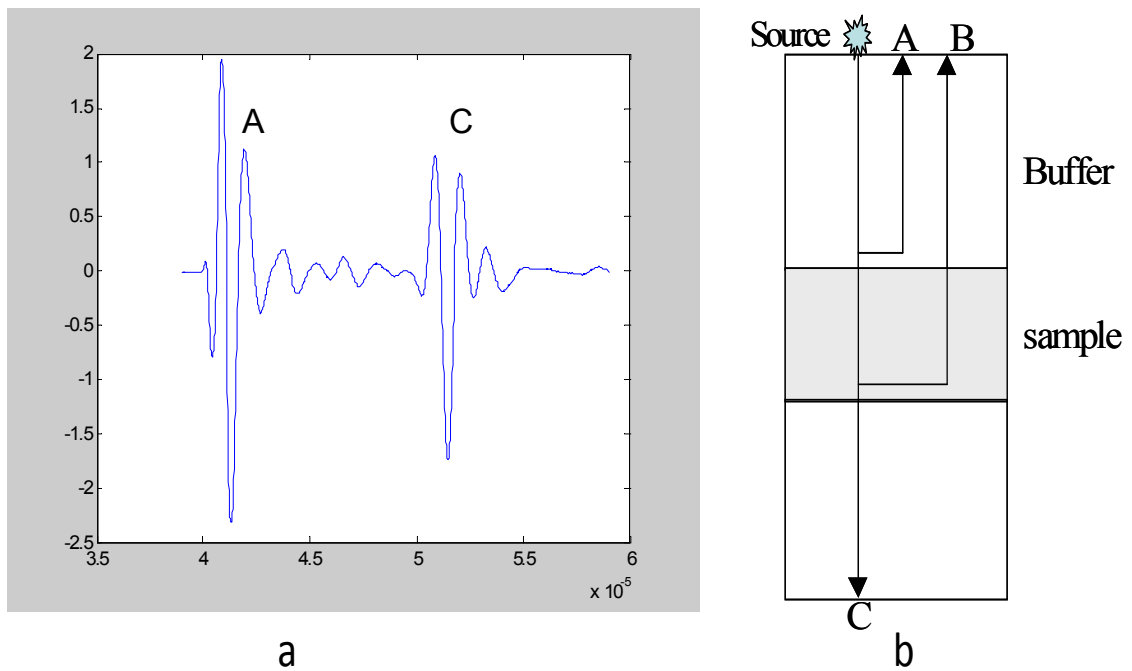


Figure 4.4 (a) The wave A is reflected from the top of the sample and C is the transmitted wave. (b) The schematic diagram of the measurement.

Q values for ultrasonic pulse transmission measurements of a sandstone sample. The rock sample density is 2.16 g/cc, porosity is 31.91%, water saturation is 100%, pore pressure is 500psi, and confining pressure is 3500psi. Figure 4.4a shows the data measured in laboratory. The waveform A is the reflected waves from the top of the sample and C is the transmitted wave. The schematic diagram of the measurement is shown in Figure 4.4b.

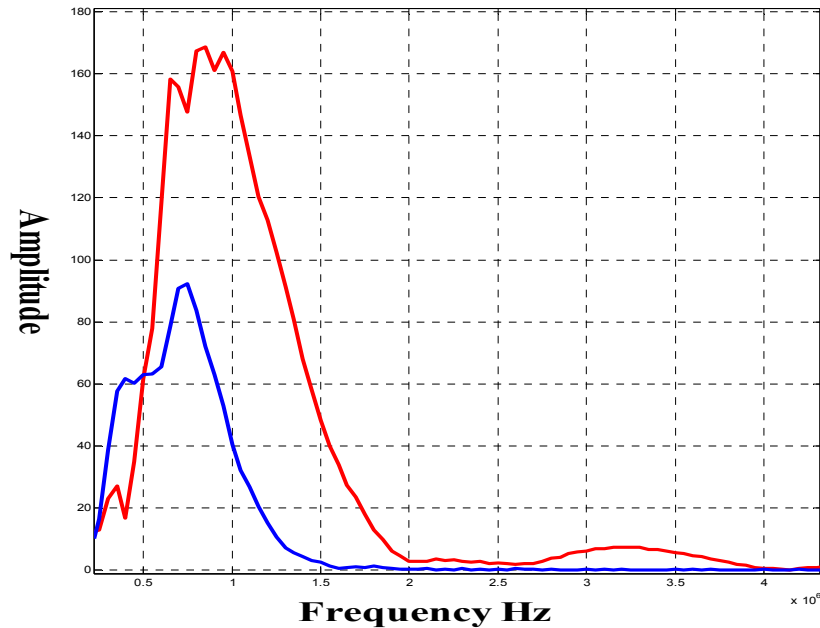


Figure 4.5 (a) is the amplitude spectrum of the signal (FFT), Red and blue lines are A wave and C wave, respectively.

Fourier amplitude spectrum of the transmitted wave shows that its amplitude is greater than that of the reflected wave around 20k Hz-50k Hz, and its amplitude dramatically changes at 70k Hz (Figure 4.5a). This phenomenon shows that the transmitted wave is not a pure transmitted wave, and that it may be a superposition of a transmitted wave and a reflected wave from side edge (Figure 4.6c and 4.6d). Estimating a Q value using Fourier spectra will be influenced by the notching, which was produced by two such closely spaced arrivals. For example, Q will be determined to be negative in the 20-50 kHz frequency range in the case. In contrast, the CWT method may avoid the temporal window influence and directly consider two local events. Figure 4.7a is CWT time-frequency spectrum of the signal, and Figure 4.7b is the threshold-window filter applied to time-frequency spectrum in order to focus local energy and better show the downward trend in the dominant frequency of the signal with time. In the time-frequency plane, a

clear downward shift in the dominant frequency of the trace with time is evident as a result of wavelet attenuation.

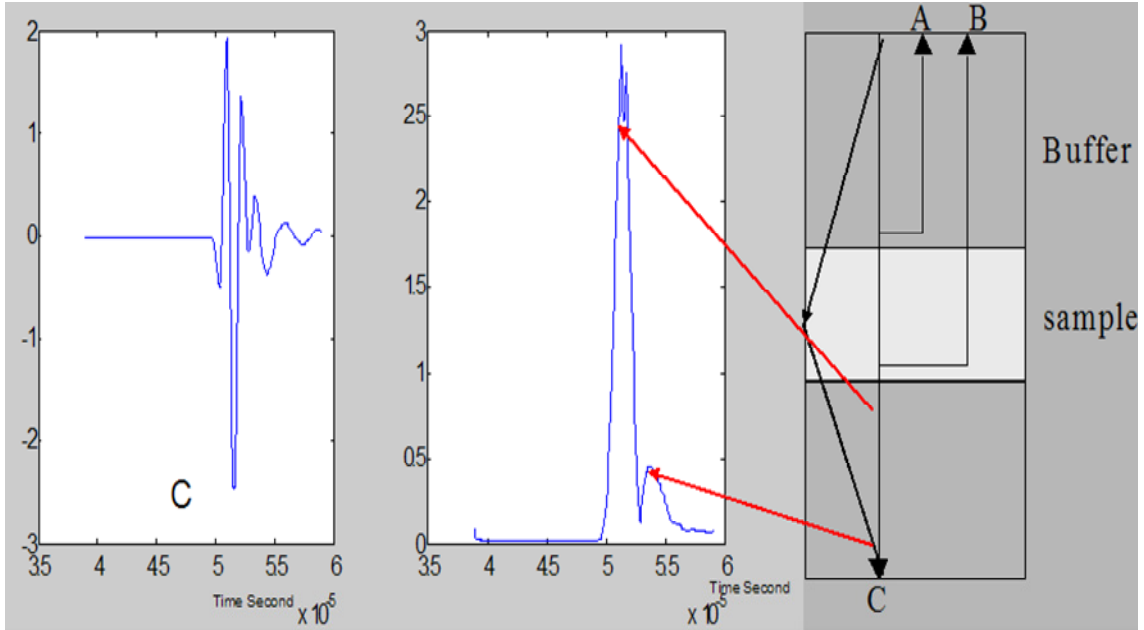


Figure 4.6 (c) is the amplitude spectrum of Hilbert transform, note the second peak of amplitude. (d) is the diagram of the possible path of C wave.

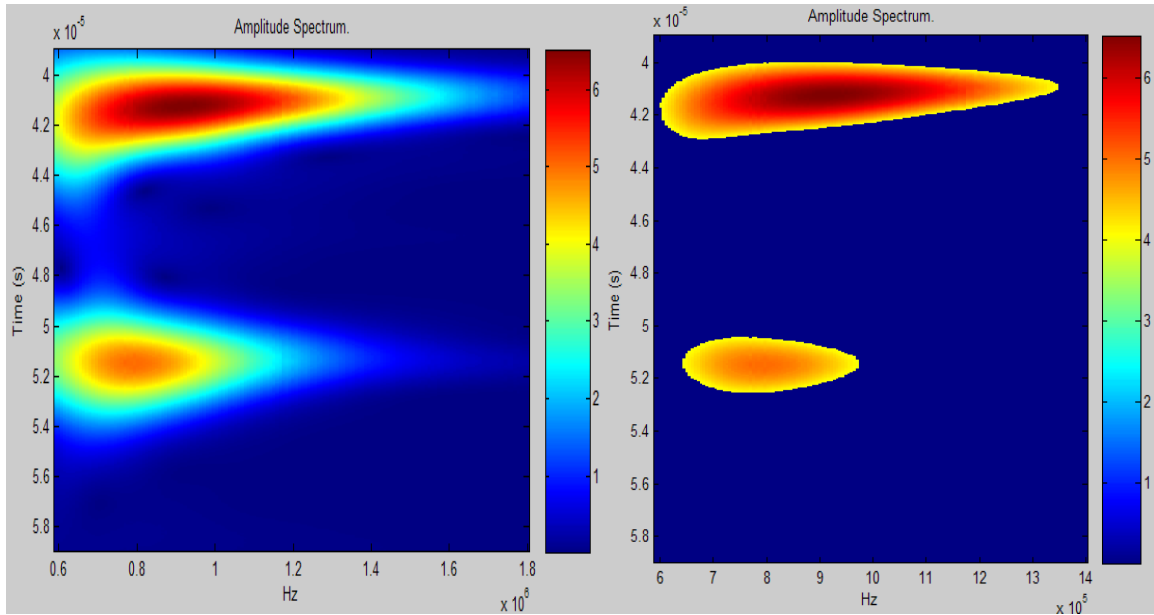


Figure 4.7 (a) CWT time-frequency spectrum of the signal, (b) the threshold window filter applied to (a).

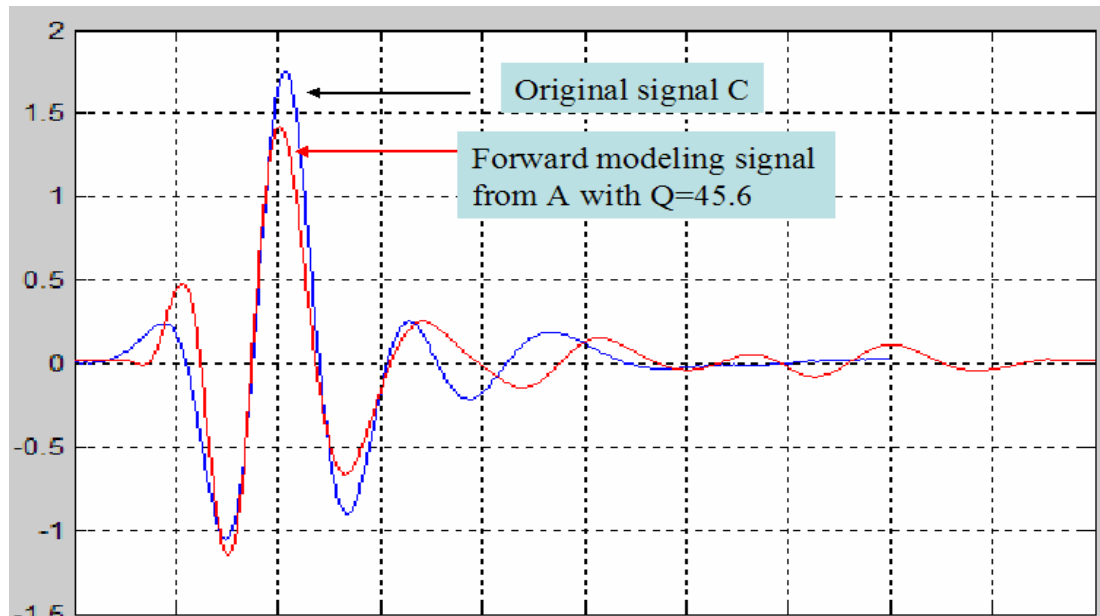


Figure 4.8 the blue line is the transmission wave C. red line is the wave generated by the reflector wave A with forward modeling.

The dominant frequency drops from 0.92 MHz to approximately 0.78 MHz over the interval shown. Using our Q value estimation procedure computed  $Q=45.6$ . To examine the accuracy of this Q value, we applied it to forward modeling through taking the first waveform A as a source signal and letting it propagate to the C location with  $Q=45.6$ . Figure 4.8 shows that the forward modeled signal significantly fits the original signal Q in dominant frequency and there is only a minor discrepancy in the relative amplitudes of the peaks.

#### 4.5 Conclusions

It has been shown that the continuous wavelet transform is a flexible time-frequency decomposition tool that can form the basis of useful signal analysis and coding strategies. This spectral analysis method makes it possible to estimate the attenuation Q values

directly between two events. In comparison to Fourier spectral ratio for Q estimation, the CWT time-frequency spectral decomposition appears to provide a more robust and effective means of estimating Q.

## **CHAPTER 5**

### **Frequency characteristics of seismic reflections in thin layer zone**

#### **5.1 Summary**

As a seismic wave propagates, it loses energy due to spherical divergence, scattering, intrinsic absorption, and reflection at interfaces where rock properties change. The amplitude and frequency responses of the reflected seismic wave are influenced by a variety of factors including: geologic structure, layer thickness, lithology, and pore fluid properties. When the seismic wave travels back to the surface, it also brings back the information related to stratigraphic features, rock property changes, and hydrocarbon accumulations. Each reservoir has its own characteristic seismic frequency response because of its unique rock and fluid properties discriminating it from the surrounding environment. To understand the underlying physical factors of the low-frequency anomaly, we build a set of wave-equation-based synthetic forward models. Analysis shows that seismic waves traveling more slowly through a gas zone than the background material are the main reason for seismic time-series delay and low-frequency anomaly in the thin layer reservoirs. Our explanation has been validated in the analysis of frequency anomalies corresponding to gas-bearing sands in the Gulf of Mexico fields.

#### **5.2 Introduction**

In stratigraphic interpretation of seismic data, emphasis has traditionally been placed on the amplitude of the reflected wavelet, whereas its frequency behavior has not been widely used. This is probably due to the fact that variations in amplitude can be straightforwardly related to variations in physical properties such as the velocity and density through the definition of the reflection coefficient, and the fact that amplitude

analysis is more straightforward than frequency analysis. In contrast, relationships between the peak frequency of a reflected wavelet and any properties of a geological formation have not yet been firmly established. After many of reservoirs were successfully found by utilizing bright spot of amplitude attribute in the past few decades, seismic exploration is now facing the prospect of searching in areas that have subtle to no seismic amplitude expression of hydrocarbons. During the recent years, seismic frequency characters analysis for recognition of hydrocarbon reservoirs has become more popular due to the increased difficulty of prospecting coupled with the rapidly development of spectral decomposition techniques. In fact, low frequency energy anomalies associated with reservoirs have been observed for many years. *Taner et al. (1979)* noted the occurrences of low-frequency energy are associated with gas and condensate reservoirs. *Castagna et al. (2003)* used spectral example to show that some gas reservoirs could be identified by low-frequency anomaly. *Li (2006)* presented a method using the continuous wavelet transform to detect thick gas reservoirs. So far, there are no proven explanations for the low-frequency phenomenon. Many researchers applied attenuation modeling in order to explain low-frequency phenomena. Because attenuation acts like a low-pass filter (it suppresses higher frequencies proportionally more than lower frequencies), some targets that contain oil or gas have a lower Q value than the background and exhibit a zone of anomalous absorption lying in a larger background region (*Winkler and Nur 1982; Klimentos, 1995; Parra and Hackert, 2002; Kumar, et al., 2003*). However, it is often difficult to explain low-frequency shadows under thin gas reservoirs where there is insufficient travel path through absorbing gas reservoir to justify the observed shift of spectral energy from high to low frequencies

(Castagna, 2003). If a particular low frequency anomaly was strictly caused by attenuation effects, one can compensate the high-frequency components within that zone by applying a reverse Q filter. But, Wang (2007) showed the low-frequency shadow zone still exists even after Q compensation. Goloshubin et al. (2006) used some examples of field-data processing to show that oil rich reservoirs exhibit increased reflective properties at low frequencies, and that expanding the active seismic bandwidth to low frequencies has a strong potential for predicting fluid content. Quintal et al. (2009) demonstrated reflection coefficients of gas reservoirs can be significantly increased and be frequency dependent in the low-frequency range because of attenuation within the reservoir caused by wave-induced flow. Sometimes this low-frequency effect, which occurs below the target, is confused with target reflection, which itself may be anomalously low or high frequency when containing gas.

In this chapter, we focus on explaining anomalously low-frequency target reflections; we do so by quantifying the various mechanisms that influence local frequency components of seismic data in thin layers (one-half-wavelength thickness). We construct a detailed forward model in order to facilitate understanding of the underlying physical factors, including local fluid properties, lithologic properties, and layer thickness variation that cause local frequency anomalies. The results of our analysis show that the decreased velocity of the seismic signal in gas and oil zones is a more important cause of low frequency anomalies than attenuation. This is because seismic signal travels in gas /oil zone at low velocities that result in push down of reflectors and cause the delay in time series which exhibit low-frequency anomalies in frequency domain.

### **5.3 Tuning and peak frequency**

We defined peak frequency as the frequency which has the maximum amplitude in the frequency domain. Lange and Ahnoghribi (1988) discussed the peak frequency behavior of seismic reflections from thin beds as a function of bed thickness and the incidence angle of the seismic ray path. By the combination of time-and frequency-domain analyses with a limited prior knowledge of the formation environment, the authors demonstrated that pore-fluid type can be determined using mode-converted waves in the frequency domain. Partyka et al. (1999) used spectral decomposition to demonstrate a heightened response of different stratigraphic targets at specific frequencies. Marfurt and Kirilin (2001) used peak frequency to map channels in seismic data. Partyka (2005) and Puryear and Castagna (2008) inverted the amplitude spectrum for layer thicknesses. Hence spectral analysis is an important tool for prediction of fluid properties and lithology and for detection and thickness estimation of thin layers. Chung and Lawton (1995) studied four different wedge models and showed that peak frequency of the reflectivity is inversely proportional to layer thickness, which used a convolutional synthetic wedge model without considering attenuation. In this section we utilize Chung and Lawton's (1995) four wedge models to determine the effect of pure attenuation on the peak frequency of thin layer zone have a lower Q value than background. We create a model of an attenuating layer inside an elastic medium half-space and quantify the effect of attenuation on the peak frequency response of the thin layer. We do not account for velocity dispersion linked to attenuation in our model.

Consider a wavelet  $W(t)$  impinging on a three-layer “boxcar” sequence, we generated a simple model of a thin layer embedded between two thick layers, with reflection

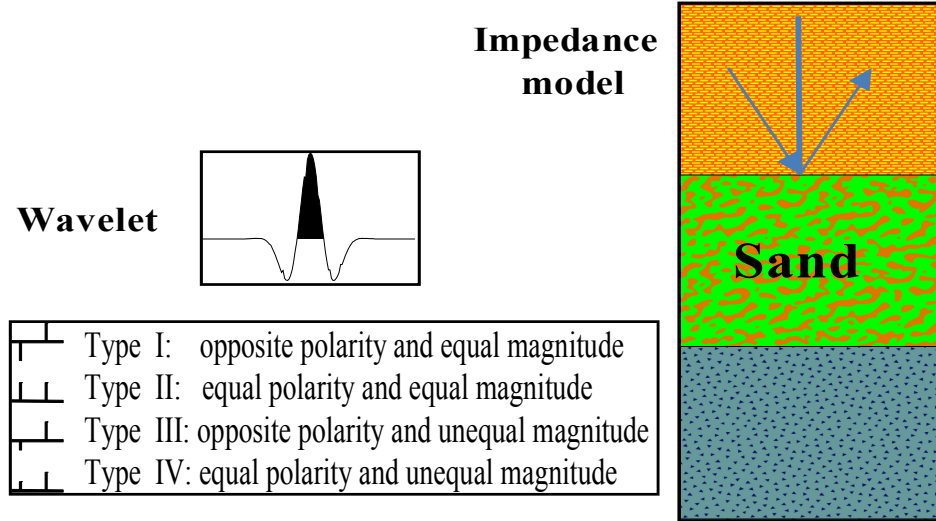


Figure 5.1 Three-layer “boxcar” model and its four types of the reflectivity series.

coefficients with magnitudes  $r_1$ , and  $r_2$  and travel times  $t_1$ , and  $t_2$ , respectively, at the top and base of the thin layer. In general, there are four fundamentally different two-term reflectivity series classified in the figure 5.1. We assume that there is no attenuation outside the middle layer, while the quality factor  $Q$  inside the layer is finite. Accounting for attenuation present inside the middle layer, the spectrum of these reflectivity series can be expressed as:

$$X(f) = r_1 e^{i2\pi f t_1} + r_2 e^{-\frac{\pi}{Q} f \Delta t} e^{i2\pi f t_2} \quad , \quad (5.1)$$

where  $\Delta t = t_1 - t_2$  is the two-way travel time within the thin layer. The corresponding amplitude spectrum is given:

$$R(f) = \sqrt{r_1^2 + r_2^2 e^{-\frac{2\pi}{Q} f \Delta t} + 2r_1 r_2 e^{-\frac{\pi}{Q} f \Delta t} \cos(2\pi f \Delta t)} \quad . \quad (5.2)$$

The amplitude spectrum of a Ricker wavelet with peak frequency  $f_0$  is:

$$W(f) = \left(\frac{f}{f_0}\right)^2 e^{-\left(\frac{f}{f_0}\right)^2} . \quad (5.3)$$

Hence, an amplitude spectrum of the thin bed response formed by the time domain convolution of a Ricker wavelet  $W(f)$  with a two-term reflectivity series is:

$$A(f) = W(f) \cdot R(f) = \left(\frac{f}{f_0}\right)^2 e^{-\left(\frac{f}{f_0}\right)^2} \sqrt{r_1^2 + r_2^2 e^{-\frac{2\pi}{Q}f\Delta t} + 2r_1r_2 e^{-\frac{\pi}{Q}f\Delta t} \cos(2\pi f \Delta t)} . \quad (5.4)$$

The peak frequency can be obtained through making

$$\frac{dA(f)}{df} = \frac{d}{df} \left[ \left(\frac{f}{f_0}\right)^2 e^{-\left(\frac{f}{f_0}\right)^2} \sqrt{r_1^2 + r_2^2 e^{-\frac{2\pi}{Q}f\Delta t} + 2r_1r_2 e^{-\frac{\pi}{Q}f\Delta t} \cos(2\pi f \Delta t)} \right] = 0 , \quad (5.5)$$

Simplifying and using  $f_p$  to denote peak frequency results in:

$$\begin{aligned} & f_p \left( \frac{r_2^2 \pi \Delta t}{Q} e^{-\frac{2\pi}{Q}f_p \Delta t} + r_1 r_2 \pi \Delta t e^{-\frac{\pi}{Q}f_p \Delta t} \left( \frac{\cos(2\pi f_p \Delta t)}{Q} + \sin(2\pi f_p \Delta t) \right) \right) \\ & = (r_1^2 + r_2^2 e^{-\frac{2\pi}{Q}f_p \Delta t} + 2r_1 r_2 e^{-\frac{\pi}{Q}f_p \Delta t} \cos(2\pi f_p \Delta t)) \cdot \left(1 - \left(\frac{f_p}{f_0}\right)^2\right) . \end{aligned} \quad (5.6)$$

Where  $f_p$  is the peak frequency sought. The equation 5.6 can be solved by iterated

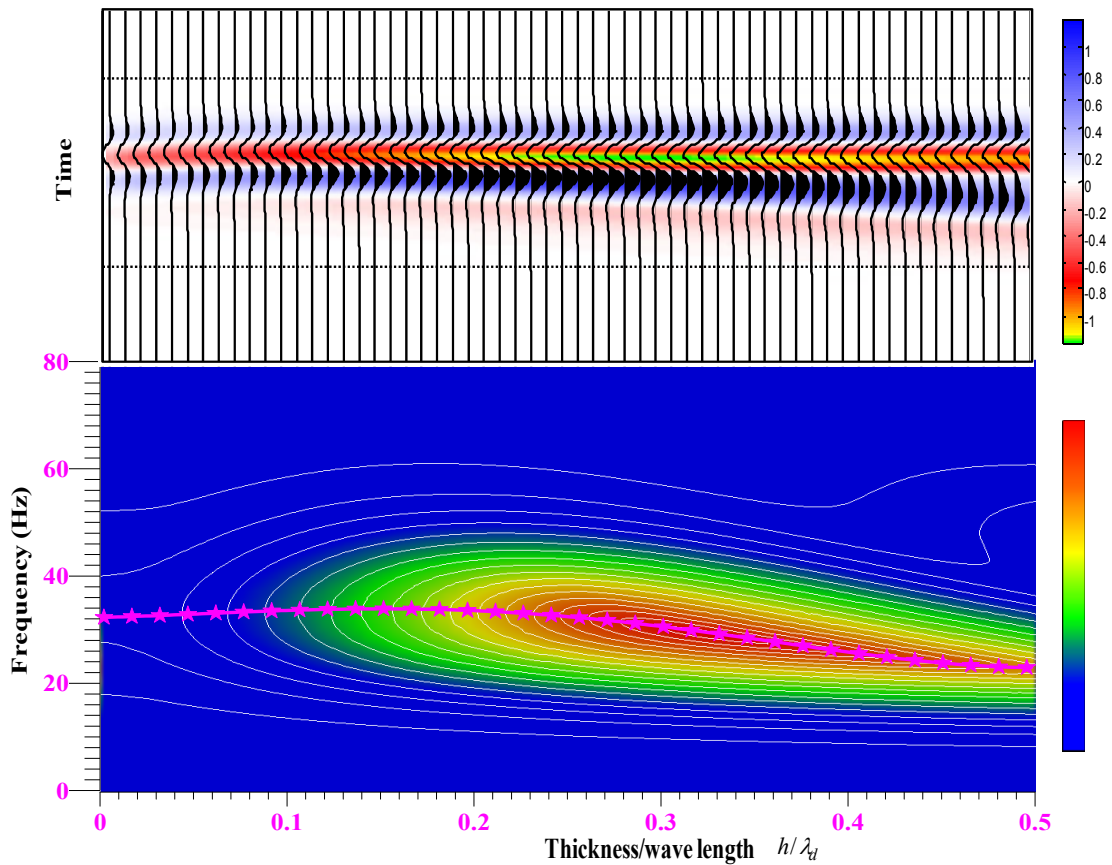


Figure5.2. The top shows synthetic traces for the Type III thin layer model with the thickness less than one-half wavelength. 30 Hz Ricker wavelet is used as a source wavelet. The bottom shows the corresponding frequency response of the synthetic traces in 2D display; the dark red color indicates the high energy location. The pink curve with stars shows the peak frequency location of the traces.

method. Synthetic traces for type III wedge model are shown in Figure5.2 (top). In this example, we used a 30Hz Ricker wavelet since this is a typical peak frequency for field seismic data. For each trace generated, the peak frequency of each trace was computed as the maximum amplitude of its Fourier frequency spectrum; the relationship between the peak frequency and thickness is plotted in pink curve with stars in the Figure 5.2

(bottom). The slope of the curve changes at a place of the quarter thicknesses. These peak frequencies consistently agree with those values predicted from equations (5.6).

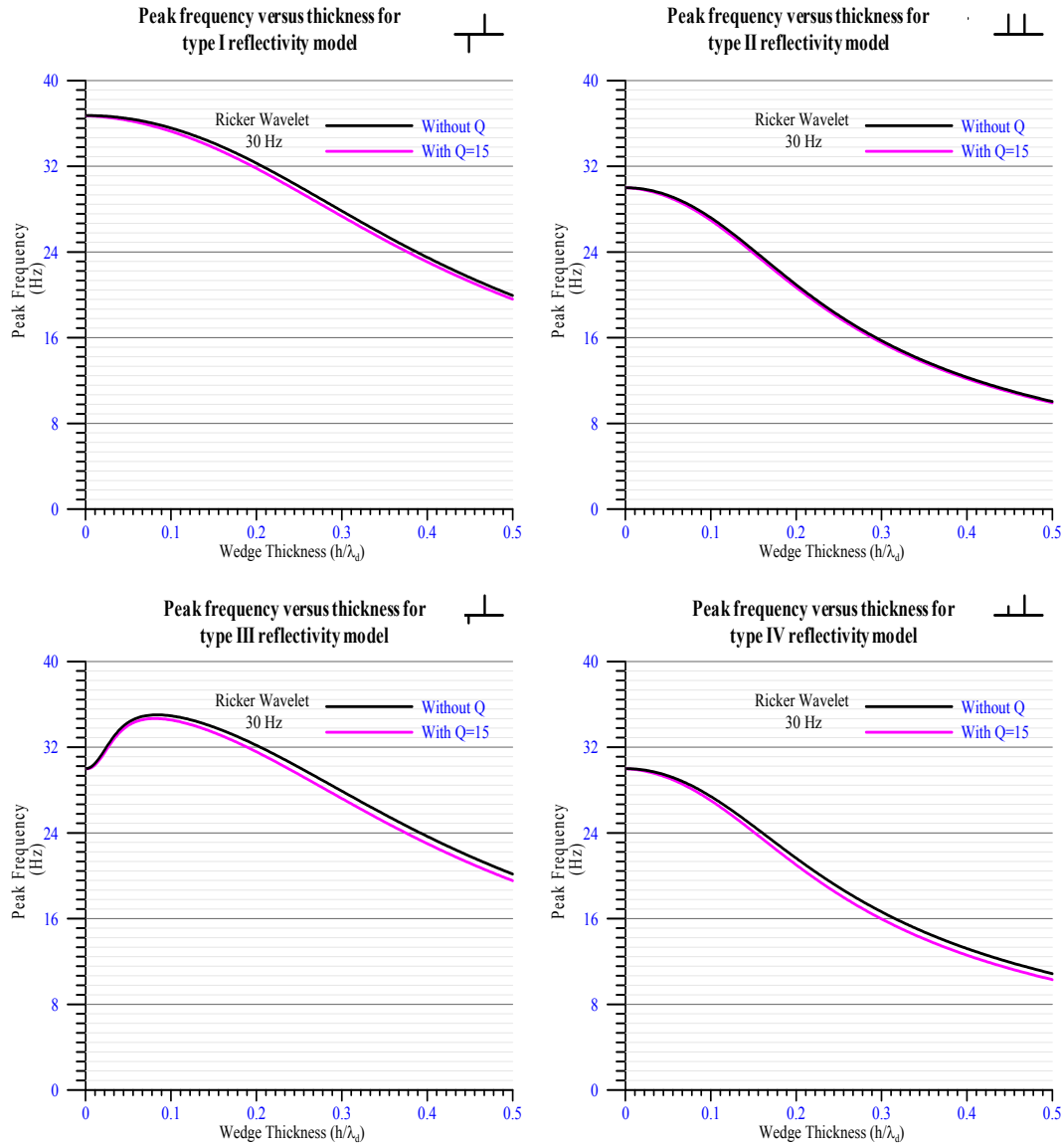


Figure 5.3 Peak frequency versus thickness for four different wedge models. The pink line shows the peak frequency location of the convolution model as a function of thickness with  $Q=15$ , the black line shows the peak frequency without attenuation consideration.

The Figure 5.3 shows the plot of the peak frequency versus thickness for four different wedge models with attenuation calculated according to equation 5.6. A low Q value of 15, which is a relative high attenuation for a reservoir, is used for the quality factor of attenuation. The travel time through attenuation layer  $\Delta t$  gradually increase as the geometric thickness progressions.  $\Delta t$  is the two-way travel time through the reservoir, and can be expressed as  $\Delta t = \frac{2h}{V} = \frac{2h}{f\lambda}$ , where  $h$  is the thickness of the layer,  $V$  is the velocity of seismic wave, and  $f$  and  $\lambda$  are frequency and wavelength, respectively. We use the thickness over wavelength as a scale – independent representation of thickness. The thickness of layer starts from 0 to 0.5 wavelengths. The reflectivity of  $r_1$  and  $r_2$  are both 0.2 for equal magnitude Type I and Type II, and 0.12 and 0.2 for unequal magnitude Type III and Type IV. The sign of the reflection coefficient is determined by the model

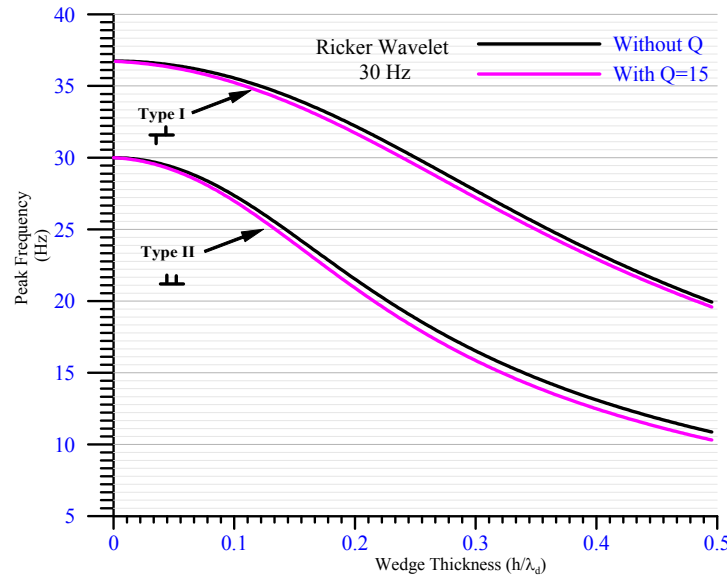


Figure 5.4 Peak frequency versus thickness for two different type of reflectivity models with the same frequency source wavelet (Ricker wavelet 30Hz). The initial peak frequencies are different as the thickness starting from zero. The initial peak frequency of type I is  $\sqrt{3/2}f_0$ , which is higher than that of original source wavelet.

type, same sign for even reflection coefficient pairs and opposite sign for odd reflection coefficient pairs. Combining the results of Chung and Lawton (1995) and the results from equation (5.6), we concluded that the peak frequency of the reflected composite wavelet will decrease as the thickness of a thin bed sequence increase. Although we used a low Q value (Q=15, a relative high attenuation) in the model, the results obtained from all four wedge models indicate that the difference between the attenuation and non-attenuation models is negligible; meaning that attenuation does not play an important role in the observed peak frequency shift in thin layer zone.

It is worth noting that the Type I and Type II wedge models start at different initial peak frequencies near zero thickness even with the same frequency source wavelet. Figure 5.4 demonstrates that as the thickness of the bed decreases to zero, the peak frequency limit will approach  $\sqrt{3/2} f_0$  for type I, and  $f_0$  for type II and type IV, where  $f_0$  is the peak frequency of the source Ricker wavelet. The Type III reflectivity is the only reflectivity that exhibits the frequency tuning effect. Frequency tuning occurs when peak frequency does not increase or decrease monotonically as a function of thickness. Figure 5.5 shows the peak frequency tuning effect occurs between thickness  $0.002\lambda_d$  and  $0.15\lambda_d$  at the following reflection coefficient pairs:  $r_1 = -0.18, -0.12, -0.06, -0.02$ , and  $r_2 = 0.2$  fixed. The plot shape of peak frequency depends on the ratio between top and bottom reflectivity, which is defined as:

$$Ratio = \frac{|abs(r_1) - abs(r_2)|}{\max(abs(r_1), abs(r_2))} \quad (5.7)$$

In general, the maximum value of peak frequency shifts down as the difference between the two reflectivity coefficients increases. Thus, in a geological setting which can be

modeled by a single thin bed, if the seismic data shows a frequency tuning effect, the setting is a Type III reflectivity sequence. Note the systematic suppression of peak frequency value as  $r_1$  influence relatively decreases when attenuation  $Q$  was taken into consideration (pink line).

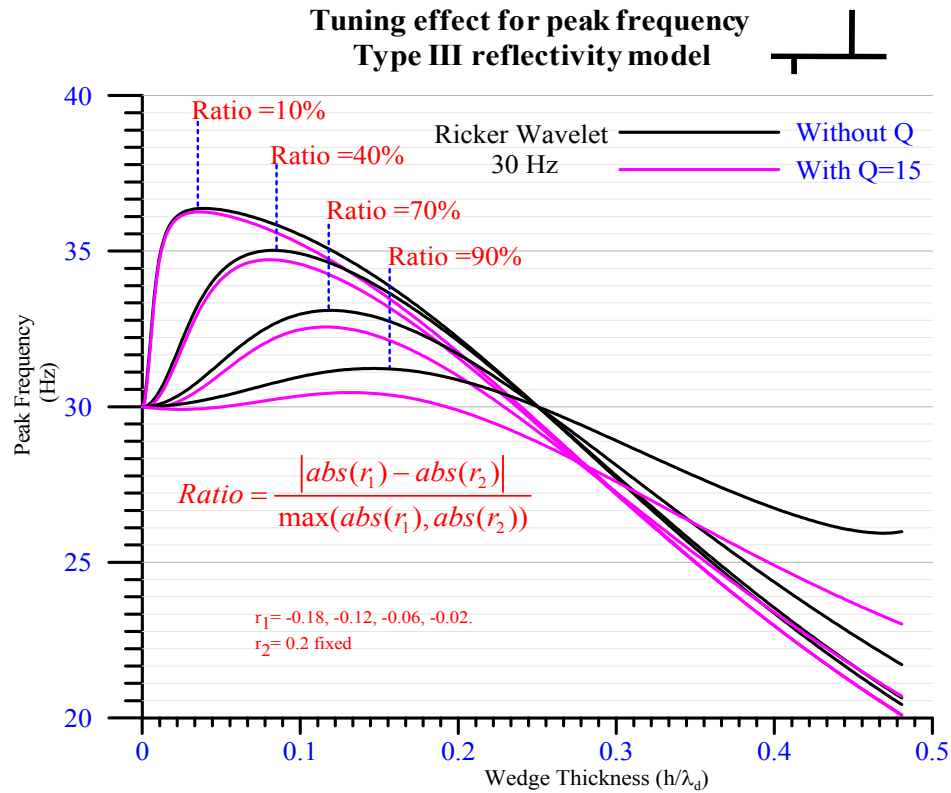


Figure 5.5 Tuning effect of the peak frequency for type III reflectivity model. In this example, the  $r_1$  values are -0.18,-0.12,-0.06, to -0.02 and the  $r_2$  is fixed at 0.2, The maximum value of peak frequency shifts toward thicker beds as the difference of the two reflectivity coefficients increases. Note the systematic suppression of peak frequency value as  $r_1$  influence relatively decreases when  $Q$  taken into account (pink line).

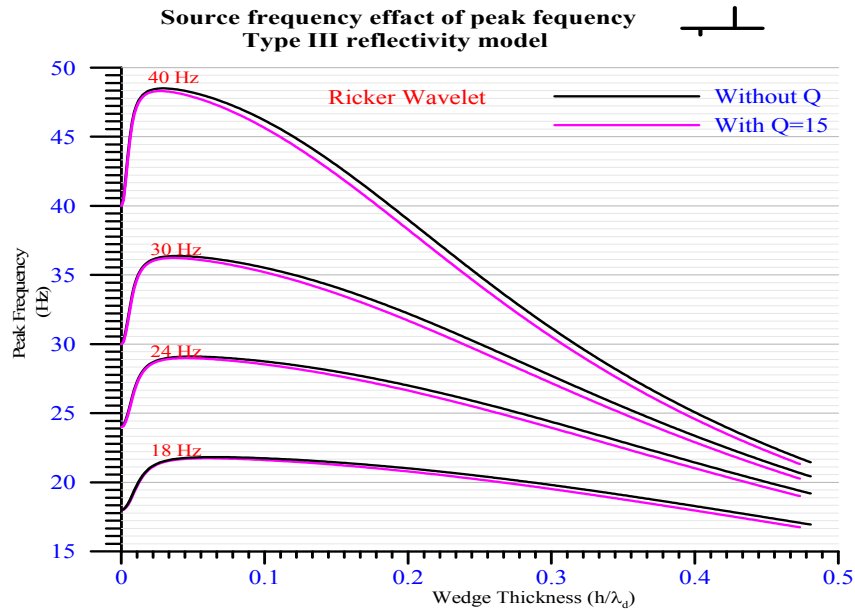


Figure 5.6 Source frequency effect of peak frequency for four different input Ricker wavelets with peak frequencies of 18Hz, 24Hz, 30Hz, and 40Hz.  $r_1 = -0.18$ ,  $r_2 = 0.2$ .

Figure 5.6 is a plot of the results of type III model ( $r_1 = -0.18$ ,  $r_2 = 0.2$ ) for four different input Ricker wavelets with peak frequencies of 18Hz, 24Hz, 30Hz, and 40Hz. Beyond the tuning effect, the peak frequency of the composite reflected wavelet decreases monotonically as bed thickness increases; the gradient is nonlinear and is frequency-dependent. The figure demonstrates that the peak frequency is more sensitive to bed thickness at higher frequencies. In processing seismic data representative of thin geological formations, geophysicists often attempt to boost the high frequency content of the data in order to increase vertical resolution. The results shown in Figure 5.6 indicate that, even if the thickness is below resolution, higher frequencies are still preferable because they are more sensitive to changes in bed thickness than lower frequencies.

#### 5.4 The factors that influence local frequency of seismic data

The final seismic frequency content is a comprehensive result of many factors including the source wavelet, the lithologic properties of the layer, the application of seismic data processing, etc (Ebrom, 2004). There are many examples which show the presence of low frequency spectral anomalies associated with hydrocarbon reservoirs. To understand the physical reasons causing this phenomenon, and to utilize it as an attribute of hydrocarbon indicator, we may classify the frequency influence factors into two categories: (1) the global factors which change the frequency of the whole seismic section, and (2) the local factors that alter the frequency content of the seismic section in the vicinity of a particular geological feature. For example, the source wavelet, the seismic data processing procedure, and the regional geologic structure are global factors. Local factors include lithologic properties, layer thickness variation, and the presence of abnormal geopressure. For the purposes of hydrocarbon detection, our interest is mainly focus on the local factors. The formula 5.6 indicates that the peak frequency is negatively proportional to the travel time  $\Delta t$ , i.e. the peak frequency decreases as the travel time increases. Since travel time is composed of two parameters, the layer thickness and wave velocity, it gives:

$$f_p \propto (-\Delta t = -\frac{2h}{V}) , \quad (5.8)$$

Thus the change of peak frequency results from the change of thickness and the change in velocity as :

$$\Delta f_p \Leftrightarrow \Delta(-\frac{2h}{V}) = \frac{2h\Delta V - 2V\Delta h}{V^2} . \quad (5.9)$$

The ratio of the change of the peak frequency to the peak frequency is given by:

$$\frac{\Delta f_p}{f_p} \Leftrightarrow \frac{2h\Delta V - 2V\Delta h}{V^2} / \frac{2h}{V} = \frac{\Delta V}{V} - \frac{\Delta h}{h} \quad (5.10)$$

Formula 5.9 and 5.10 indicate several interesting things. First, they imply that the change of peak frequency moves toward the same direction with the change of velocity but opposite direction with the change of the thickness. Second, the ratio of the change in peak frequency to peak frequency is the same order of magnitude as are the ratio of the change in velocity to velocity and change in thickness to thickness. The changes in the two terms determine the changes in peak frequency. If we have prior knowledge of either velocity or thickness, we can measure the variation of peak frequency to estimate the thickness in the reservoir zone, or to predict local lithologic and fluid properties and the presence of abnormal geopressure that often result in the velocity variation. For example, given 4D seismic data at the fixed thickness, the peak frequency analysis can be used as an important tool for mapping and monitoring of fluid movements and pressure changes in petroleum reservoirs during production, thus contributing to improved recovery rates and better management of the fields. Figure 5.7 shows the peak frequency versus velocity variation with the various attenuation factors at two fixed thickness conditions  $h = 0.25\lambda_d$  and  $h = 0.5\lambda_d$ , respectively. This is the example of type III reflectivity model, 30Hz Ricker wavelet as a source wavelet. We decrease wave velocity about 25% from 2300 m/sec to 1725m/sec. In both conditions, we observe that attenuation factors do not significantly affect peak frequency. With the thickness fixed at 0.25 wavelength, there is only 0.6Hz difference of peak frequency between with  $Q=10$  and no attenuation; and a 0.85Hz difference in peak frequency for the model with thickness fixed at 0.5 wavelengths. However, a 20 percent of velocity decrease can cause approximately 1.5 Hz

difference in peak frequency at the thickness 0.25 wavelengths, and a 3.9 Hz change at thickness 0.5 wavelengths.

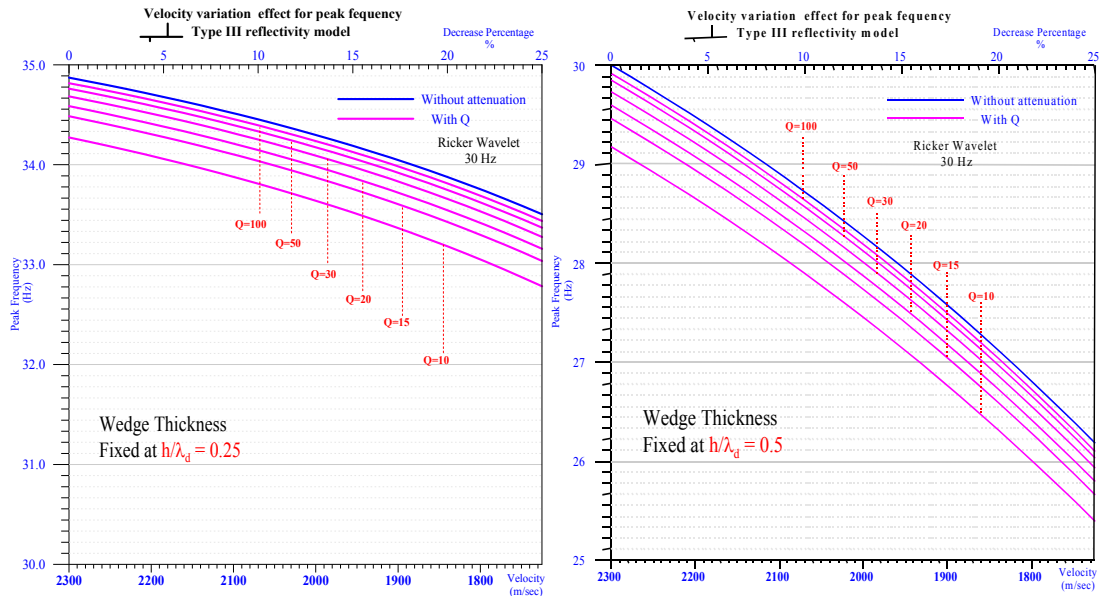


Figure 5.7 Velocity variation effect for peak frequency of type III reflectivity model with the fixed thickness place. The left is wedge thickness fixed at 0.25 wavelengths. The right is wedge thickness fixed at 0.5 wavelengths.

We use a three-layer wedge model to study the effect of layer thickness, lithology, and fluid properties on the local frequency response. A low-impedance layer (e.g., gas sand) is sandwiched between two high-impedance layers (e.g. shale). We begin by investigating the influence of layer thickness on the frequency response, particularly where the layer thickness is less than one-half wavelength. In this region the reflected events from the top layer and the bottom layer will overlap and produce a compound signal whose peak frequency depends on the thickness. After layer thickness increases beyond one-half wavelength, the two events can be resolved in two-way travel time. The physical parameters of the layers are shown in Figure 5.8 ab. Here the typical velocity and density values were taken from published data for shale and sandstone in the Gulf of

Mexico. The rock physics parameters are shown in the figure, the porosity of the gas sand is 32% with an initial water saturation of 0.1. Gassmann equation is used for fluid substitution in this study. The synthetic traces are generated by a plane-wave propagation model with attenuation as shown in Figure 5.8c. The source wavelet is a zero-phase Ricker wavelet with a peak frequency of 30 Hz.

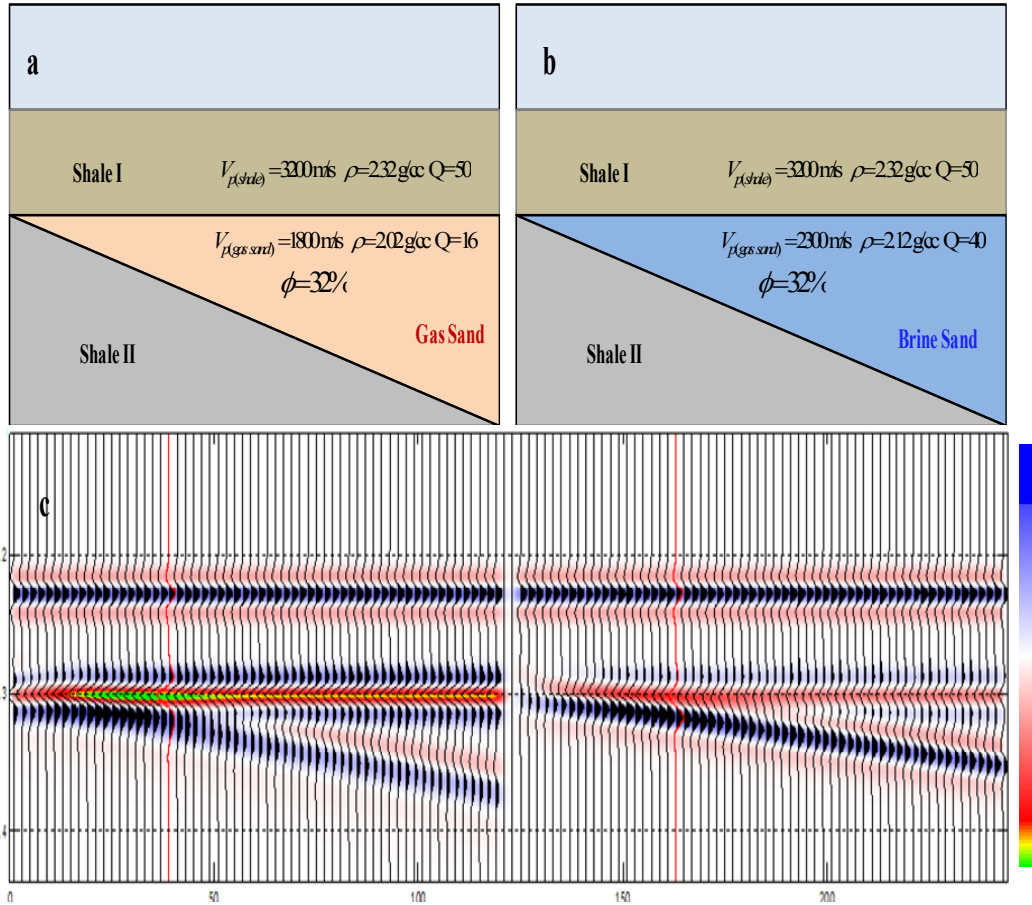


Figure 5.8 The geology model and its synthetic seismic traces. The red traces indicate at one-half wave length thickness location

Now, we fix the layer thickness at one-half wavelength to investigate how the velocity variation controlled by the fluid properties affects the peak frequency. Figure 5.9 (left) shows the results of varying only the Q value. We keep everything at the same condition

except for changing Q value from 50 to 16. As expected, the peak frequency difference for the range of Q values is less than 1 Hz, meaning that pure the attenuation effect does

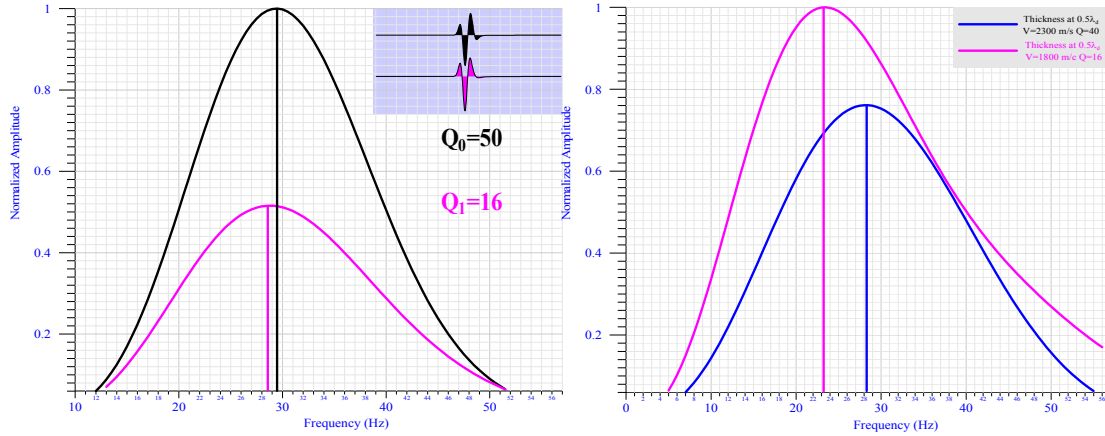


Figure 5.9 Left (a) is the frequency response of the two signals with only changing Q values. The right (b) is the frequency response of brine sand velocity  $V_p=2300$  m/s and gas sand velocity=1800 m/s.

not significantly affect the peak frequency in the thin layer zone. However, if the fluid properties change from fully brine saturated into fully gas saturated, it will yield a velocity change of approximately 20% from 2300 to 1800 m/s and a peak frequency decrease of about 5Hz. The lower velocity of the gas sand causes time sag of the base of sand reflector that modifies the reflectivity spectrum. This corresponds to a visible spectral shift toward low frequencies in the reflected signal. The internal velocity effect is more important than the Q value in determining the peak frequency. This relationship also could explain the commonly observed association of abnormally high geo-pressure regions with low-frequency anomalies because high pore-pressure reduces the effective pressure and results in a decrease in the velocity of the rock.

Figure 5.10 shows a comparison between the peak frequency shift that occur for a 20% thickness change of a brine sand and for a 20% velocity change caused by substituting brine for gas at a fixed thickness. The amplitude response is normalized to unity to

investigate the frequency response. The 20% velocity variation caused by changing the pore-fluid content causes a larger frequency shift (4.5Hz) than the 20% thickness variation (2Hz). This means that at in situ conditions the gas-containing reservoir may display a discernible low frequency anomaly if the thickness of the layer varies laterally less than 20%, and also implies that it should be easier to detect and identify an area or compartment of a reservoir that has gone through a fluid property change than an area that has experience the thickness changes.

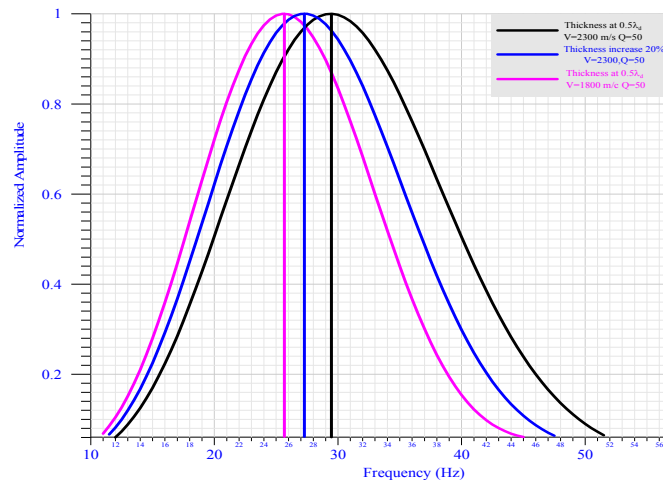


Figure 5.10 Comparison of the effect of a 20% thickness increase and 20% velocity decrease on peak frequency. ( $V_p$  from 2300 m/s to 1800m/s).

## 5.5 Conclusions

Seismic reflection amplitudes are influenced by many parameters such as thickness, lithology, porosity, and fluid content. In conclusion, the reservoir thickness and the acoustic impedance (velocity and density) are the major factors that control the spectral responses of the seismic signal in the thin layer zone. If the reservoir thickness is varied less than 20%, velocity is the dominant factor that influences the peak frequency shift.

## CHAPTER 6

### **Anomalous frequency as a direct hydrocarbon indicator**

#### **6.1 Time –frequency analysis and local-frequency anomaly**

With the rapid development and improvement of spectral decomposition, Joint time-frequency analysis is today one of the principle tools used to analyze non-stationary data such as seismic recordings. In general, seismic data will experience an increasing amount of attenuation with depth as a result of the growing number of attenuating layers and interfaces it must pass through. Attenuation acts like a low-pass filter; it suppresses higher frequencies proportionally more than the lower frequencies. Targets that are oil or gas reservoirs usually have lower Q value zones and lower velocities than the background does, and thus exhibit zones of anomalous absorption and will delay the travel time in a larger background region. Therefore we can find a large frequency shift to low frequency direction at these reservoir locations. To extract the frequency anomaly, we have to remove the increased attenuation trend. The most common de-trending process usually consists of removing a straight line best fit, yielding a zero-mean residue. Such a trend may suit well in a purely linear and stationary world. However, the approach may be illogical and physically meaningless for real-world applications such as in seismic data analyses. Therefore I derived a formula for the analysis of peak frequency trend based on underlying physical mechanism of attenuation, which in turn gives a non-linear and non-stationary function. In the following steps, I will introduce the trend function which corresponding algorithm for finding intrinsically the trend and give a method to remove the background trend. Because the de-trended data define a more meaningful variability

associated with a particular time scale of the data, the method is validated by application to real data. It should be noted here that the definition of trend and the algorithm for detrending in this method are applied to seismic data that are non-stationary and non-linear processes. By definition, attenuation affects the amplitude spectrum of the propagating seismic wavelet and thus the resulting reflection seismogram as

$A(f) = A_0(f)e^{-\frac{\pi f t}{Q}}$ , here  $A_0(f)$  is source wavelet. If we take Ricker wavelet  $W(f)$  with peak frequency  $f_0$  as a source wavelet, the amplitude of spectral of seismic wave is:

$$A(f) = W(f)e^{-\frac{\pi f t}{Q}} = \left(\frac{f}{f_0}\right)^2 e^{-\left(\frac{f}{f_0}\right)^2} e^{-\frac{\pi f t}{Q}} . \quad (6.1)$$

To find the peak frequency location, making

$$\frac{d(A(f))}{df} = \frac{d}{df} \left( \left(\frac{f}{f_0}\right)^2 e^{-\left(\frac{f}{f_0}\right)^2} e^{-\frac{\pi f t}{Q}} \right) = 0 . \quad (6.2)$$

Expanding and simplifying it, it gives:

$$W(f)e^{-\frac{\pi f t}{Q}} \left( f^2 - \frac{\pi t f_0^2}{2Q} f + f_0^2 \right) = 0 . \quad (6.3)$$

Since  $W(f)e^{-\frac{\pi f t}{Q}} \neq 0$ , thus

$$\left( f^2 - \frac{\pi t f_0^2}{2Q} f + f_0^2 \right) = 0 . \quad (6.4)$$

Hence solving this equation and keep the real solution, it gives the peak frequency

$$f_p = f_0 \sqrt{1 + \left(\frac{\pi f_0 t}{4Q}\right)^2} - \frac{\pi f_0^2 t}{4Q} . \quad (6.5)$$

This formula shows the relationship of peak frequency and travel time. We can estimate

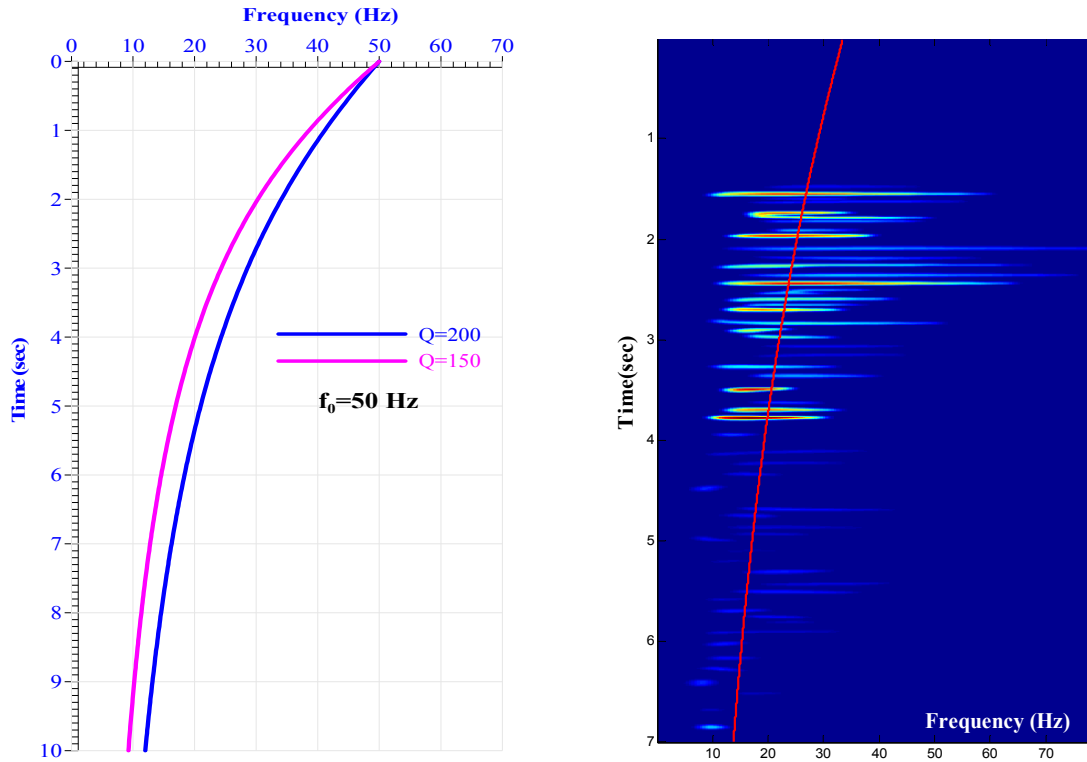


Figure 6.1 the left figure plots two theoretical curves of peak frequency vs. travel time for initial peak frequency at 50 Hz, pink line is attenuation quality factor 150, the blue line is  $Q=200$ . The right is a time frequency spectral of a real seismic trace. The red line is a fitting curve of a peak frequency trend.

a general peak frequency trend line by fitting this formula along with time direction.

Figure 6.1 (left) demonstrates two theoretical curves of peak frequency vs. travel time for initial peak frequency at 50 Hz. Figure 6.1 (right) is a time-frequency spectral of a real seismic trace. The red line is a fitting curve of a peak frequency trend. The difference between the trend fit and the local variation is  $Af(t) = Lf(t) - Tf(t)$ , where  $Lf(t)$  and  $Tf(t)$  are the frequency values from local peak frequency location and frequency trend fit location respectively. Thus large  $Af(t)$  values indicate areas of anomalous lower frequency, i.e. zones of anomalous velocity and high absorption. To obtain a true trend

line which can be used to represent the global background, we have to select a location where there is no frequency anomaly or to use an averaged trend by

$$Tf(t) = \frac{1}{n} \sum_{x=1, \dots, n} Tf(x, t),$$

where  $Tf(x, t)$  is the frequency trend at the  $x$  receiver. This

method to extract anomalous frequency values is not affected by the seismic data that have been previously spectrally balanced because spectral balancing changes only the amplitude spectral of sub-bands which does not shift peak frequency location. We are measuring only the trend of the peak frequencies, not the phase, thus spectral balanced data will be acceptable for this technique.

I now summarize the procedure in the following steps.

- 1) Calculate time-frequency spectral decomposition for each seismic trace after spectral balancing.
- 2) At each seismic trace compute the peak frequency location at each time location  $F_p(x, t)$ .
- 3) Get the local trend line  $Tf(x, t)$  by using the formula (6.5) to fit  $F_p(x, t)$  along with time direction.
- 4) Get the global trend line  $Tf(t)$  by using the formula  $Tf(t) = \frac{1}{n} \sum_{x=1, \dots, n} Tf(x, t)$  to average the local trends.
- 5) Subtract the global trend from the local frequency location by  $Af(x, t) = Lf(x, t) - Tf(t)$
- 6) Apply 2D or 3D low-pass filter to eliminate the outliers.

To make the resultant anomalous values more clearly differentiable, one can also use the

formula  $Af_{var}(x, t) = Lf(x, t)^2 - Tf(t)^2$  in step 5, where negative-valued zones represent higher than normal frequency trend and positive value zones represent the lower than normal trend.

## 6.2 Field data examples

Time-frequency analysis is used to directly compute seismic frequency attributes from field data that include the KingKong reservoir and a nearby fizz gas well (Lisa Anne). I followed the method described in Chapter 2. I first extracted an orthogonal wavelet from a seismic signal near the KingKong well, and then used this orthogonal wavelet as a mother wavelet to apply the hybrid wavelet transform based on the methods described in Chapter 3 for decomposing all fields of 3D seismic cube data into a time-frequency domain. Next, I followed the procedures described in the preceding section to remove the background trend and extract the frequency anomaly. Figure 6.2 shows the input 3D seismic volume. KingKong reservoir is a gas reservoir characterized by strong amplitude anomalies (O'Brien, 2004). Lisa Anne has a similar set of amplitude anomalies within the same stratigraphic interval on the southeastern flank of the basin (Figure 6.3). However, no commercial hydrocarbons were found in the Lisa Anne location; it was a fizz reservoir. The sand quality at KingKong and Lisa Anne is excellent, with porosities of 32-35%, and target sand thickness of approximately 26 meters. Figure 6.4 shows a seismic profile line AB that crosses the KingKong and Lisa Anne. The marked zones around time 4000 ms are the target sand location and associated with bright spots. Figure 6.5 demonstrates the time-frequency gathers of seismic traces at KingKong and Lisa Anne respectively. The white line is a curve fit of the peak frequency background trend.

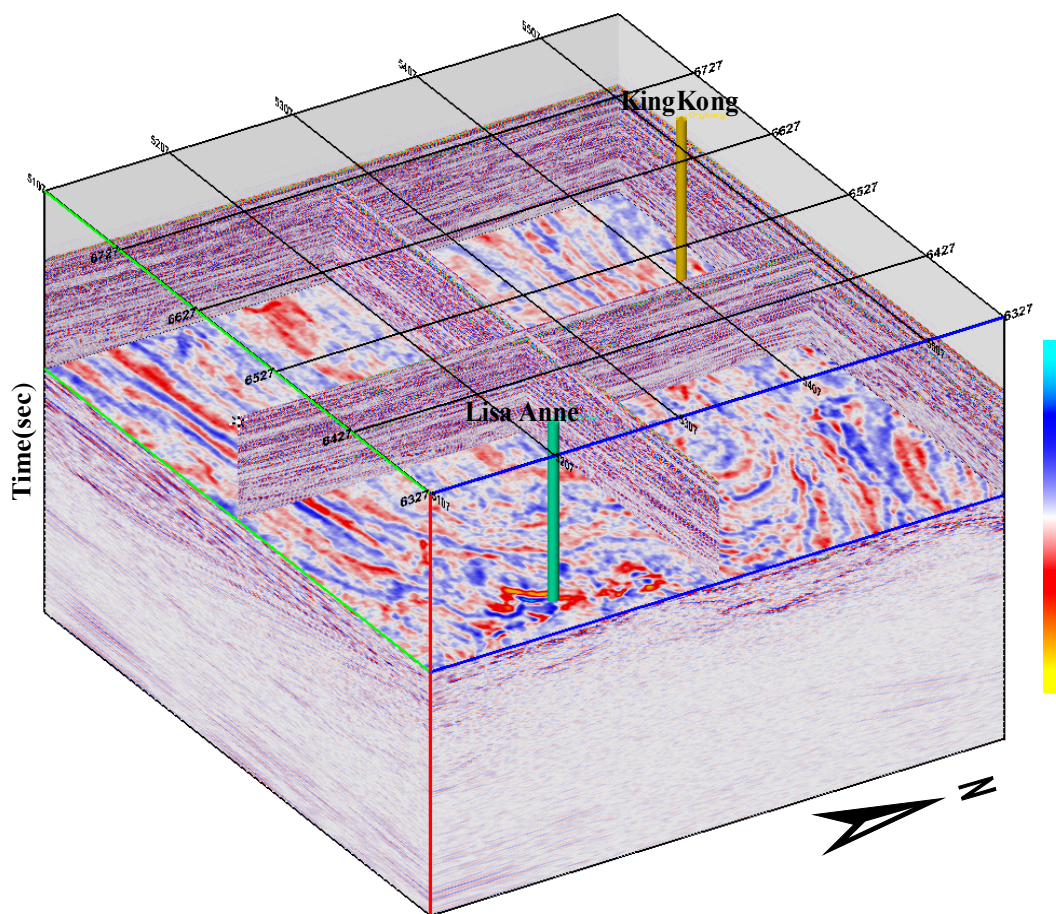


Figure 6.2 3D seismic data volume of KingKong and Lisa Anne reservoir.

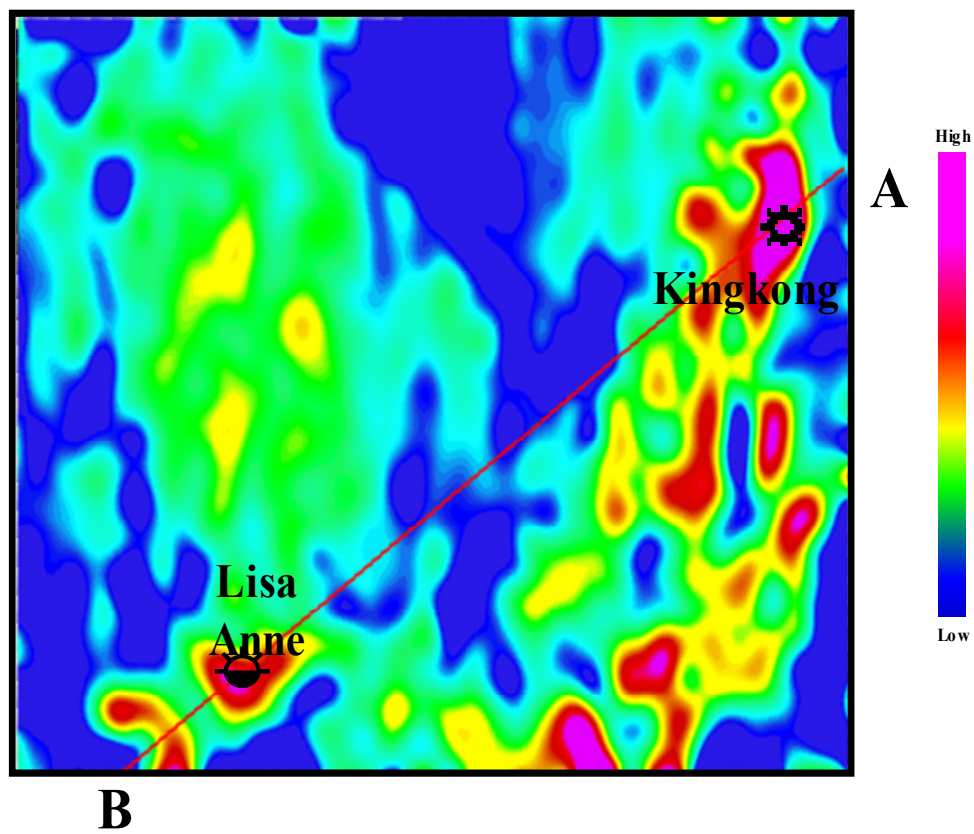


Figure 6.3 RMS amplitude of a 2D map of target sand horizon with a window around the horizon +/- 25 ms. Note that both KingKong and Lisa Anne exhibit the amplitude anomalies.

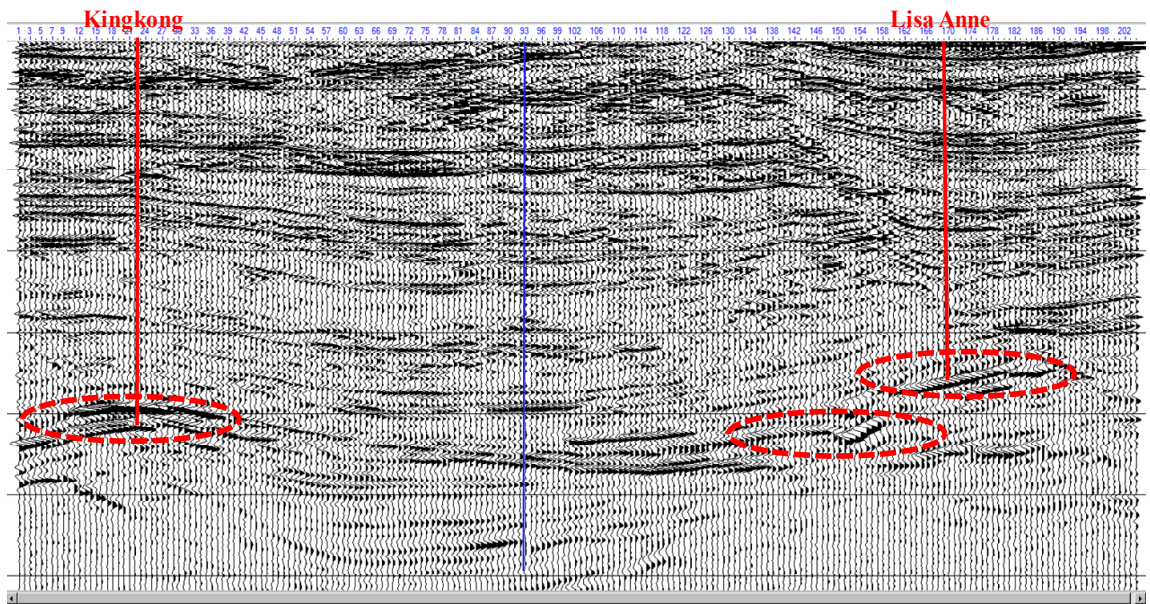


Figure 6.4 A seismic profile line AB that crosses the wells KingKong and Lisa Anne. The blue line marks trace 93 where no frequency anomaly appears.

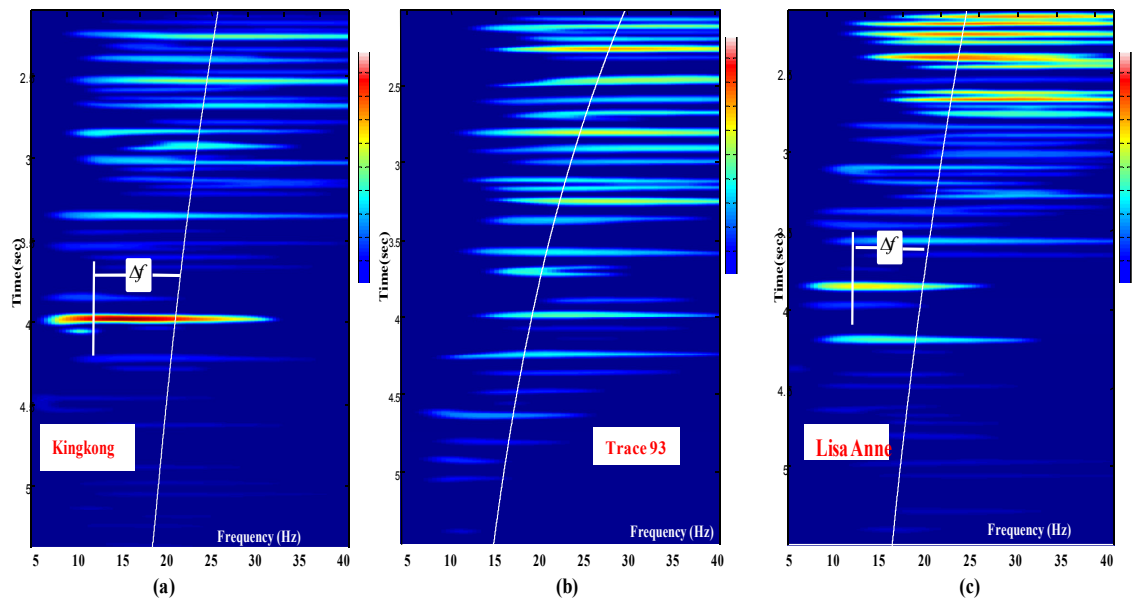


Figure 6.5 Time-frequency gathers of seismic traces. (a) is the time-frequency gather of the seismic trace located at the KingKong well. (b) is the time-frequency gather of the seismic trace 93(blue line Figure 6.4). (c) is the time-frequency gather of the seismic trace at the Lisa Anne well. The white line is a curve fit of the peak frequency background trend. Note that large low-frequency anomalies appear at the target sand location.

The differences between the local peak frequency and the background trend were marked at the target sand locations; it turns out the significant low-frequency anomalies appeared at these positions. The peak frequencies at target sands are about 12 Hz and 13.5 Hz respectively, and the maximum peak frequency shift down from the background trend is approximately -5.5 Hz at the KingKong location. Figure 6.6 shows frequency anomaly profile line AB after removing the background peak frequency trend. The orange colors represent large negative peak frequency anomalies, which spatially coincide with the target sands. Note that other strong amplitude events do not exhibit the same low frequency anomaly response observed near the two well locations. Figure 6.7 is a 2D

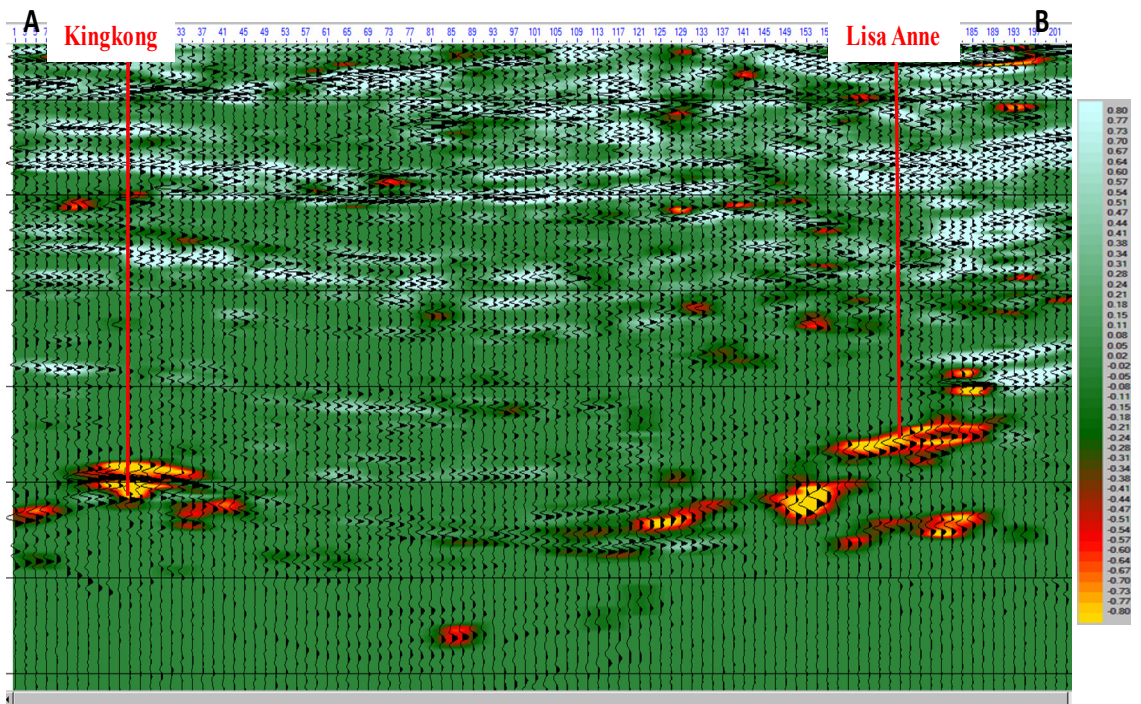


Figure 6.6 low frequency anomalies profile of AB line. The orange color represents large negative peak frequency anomalies.

anomaly map that was generated by the summation of negative peak frequency anomalies along the target sand with a window from target  $\pm 50$  ms. Comparing Figure

6.7 with the Figure 6.3, the gas-bearing sand was nicely outlined in Figure 6.7 and the gas contain was also indicated by the magnitude of the negative frequency anomaly. A strong negative frequency anomaly response appears at KingKong well area associated with gas-bearing sand zone and the relative small and weak response was shown in Lisa Anne well area in which fizz containing sand layer is located. Figure 6.8 shows low-frequency anomaly attributes were distributed in 3D seismic volume. The yellow-orange colors that represent low-frequency anomaly display the distribution of producing gas sand locations. It can be seen that no other place has large low-frequency anomalies except the area near round two well locations. This implies that the low-frequency anomaly attribute effectively isolate the potential target zone from its surrounding environments. It can provide a detailed and accurate estimate of distribution of reservoir

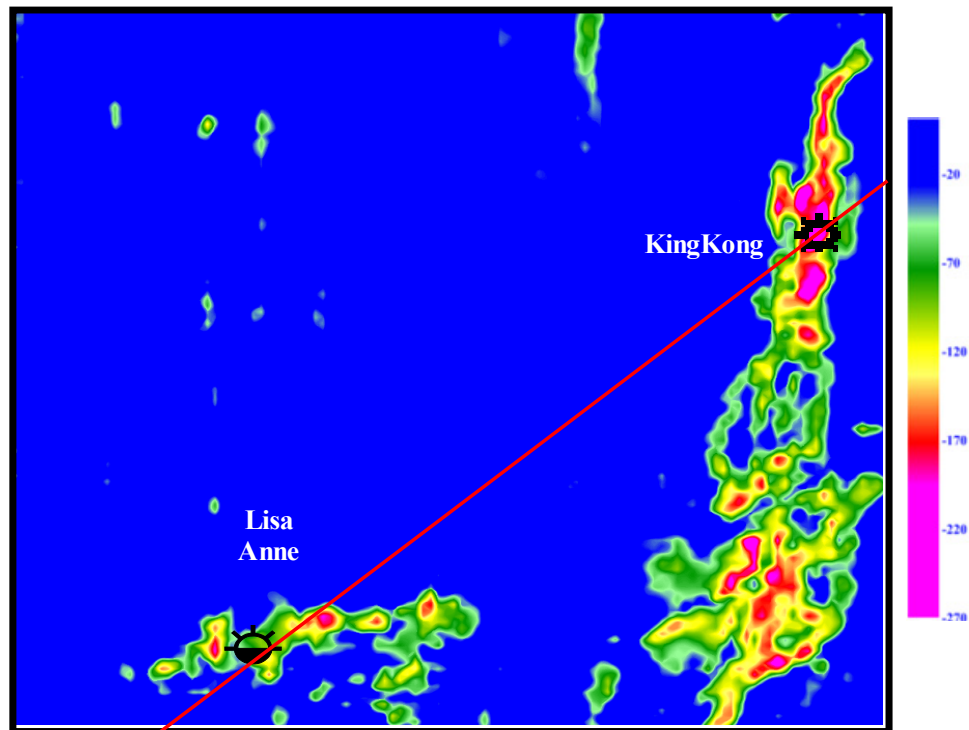


Figure 6.7 Sum of negative frequency anomalies of 2D map of target sand horizon with window at +/- 50 ms.

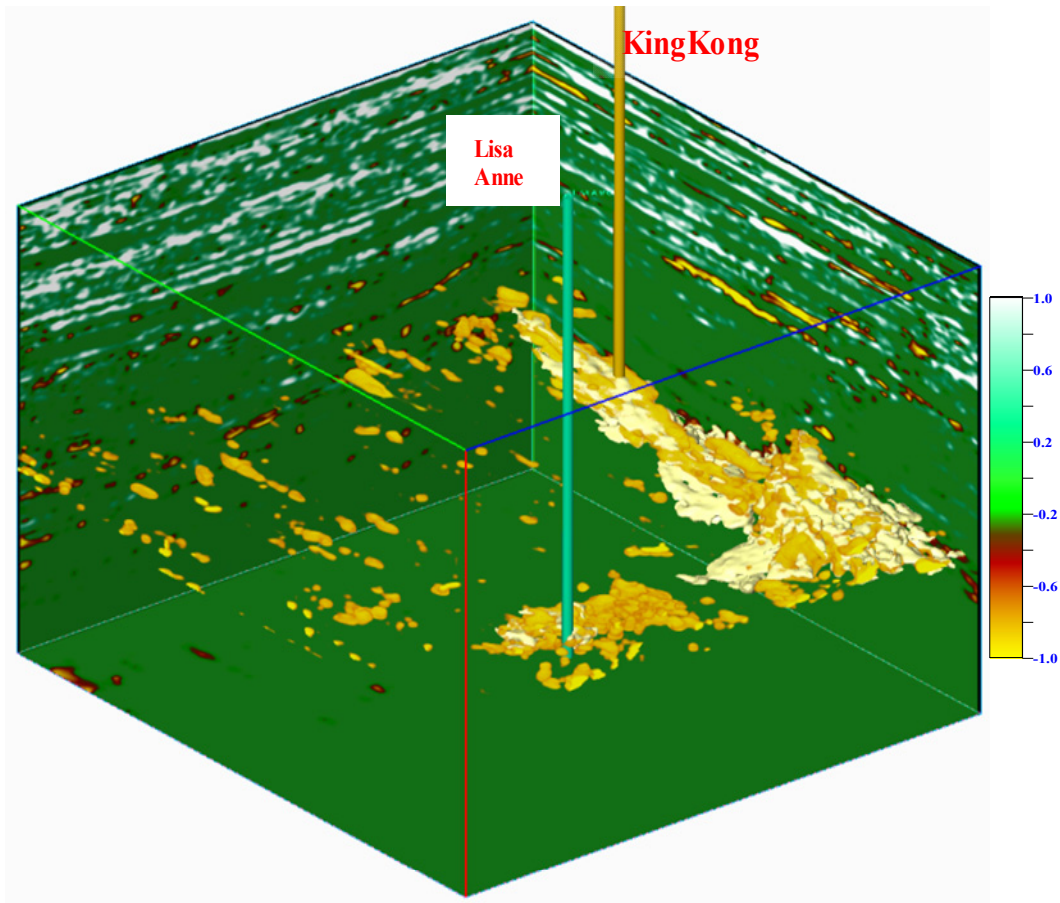


Figure 6.8 the 3D volume of frequency anomaly attributes.

sands in the zone of interest. Next we will investigate the reason for the low-frequency anomalies observed at KingKong reservoir. Figure 6.10 shows the KingKong well log and the associated synthetic trace. The dominant frequency of the seismic data is approximately 25 Hz; the sonic log indicates that the shale velocity of the top layer is approximately 2590 m/sec and the gas-sand velocity is around 1846 m/sec. The thickness of the target sand is 26 meters, which is approximately one-half wavelength, if we use the formula  $V = f\lambda$  to estimate the wavelength of seismic wave propagation, taking  $V=2600$  m/s, and  $f=25$ Hz, for two ways travel time. From the previous analysis in the section 5.3, we know that attenuation factor (Q) alone cannot cause such a large negative

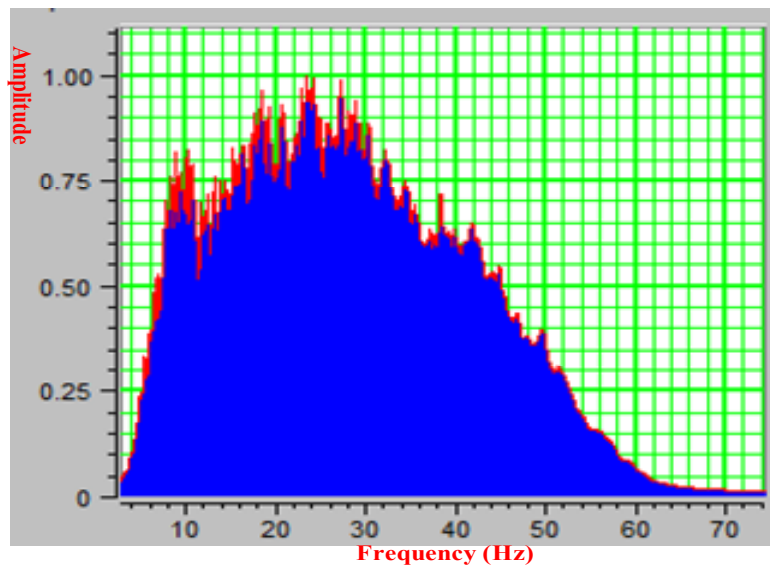


Figure 6.9 Amplitude spectrums of the seismic data.

frequency shift (less than 1Hz) due to the insufficient distance traveled through the gas sand. Instead, the low velocity through the gas zone causes the wave delay. Thus, the low velocity is the primary reason for the low-frequency anomalies. Also, from inspection of Figure 6.10, two-way travel times  $\Delta t$  from the top to the bottom of gas-sand layer is

approximately 80 ms, resulting in a center frequency  $f_c = 1/0.08 = 12.5$  Hz for this event.

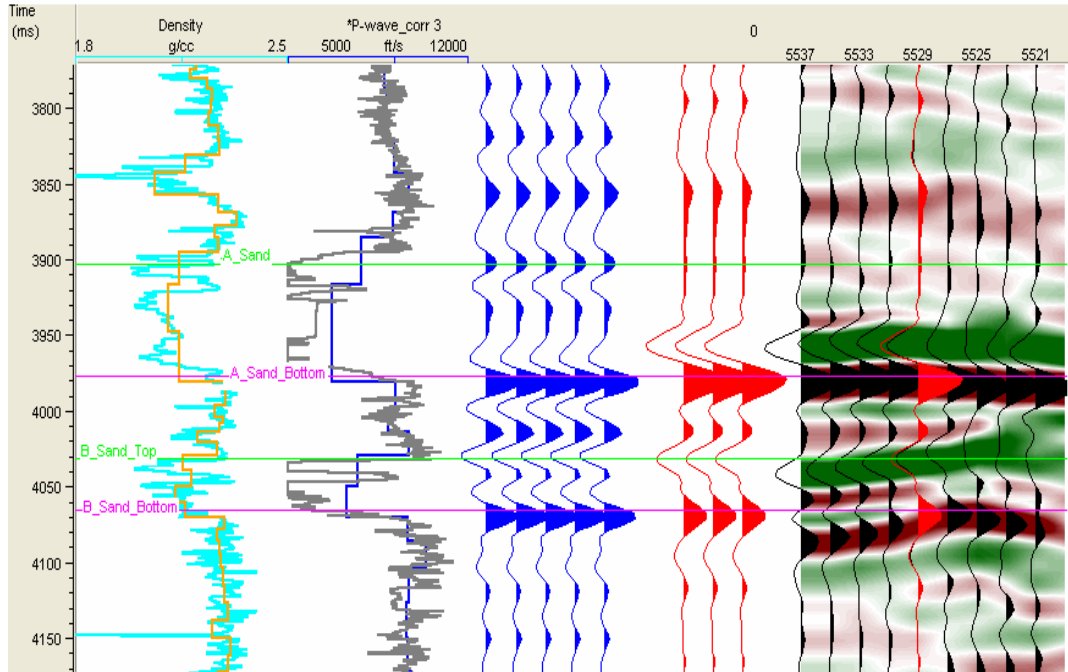


Figure 6.10 Density log, sonic log, synthetic trace, correlation trace and seismic section at KingKong well.

Figure 6.11 shows a series of common frequency profiles. The target sand horizon near KingKong well does not exhibit energy at 33 Hz, but exhibits a strong anomaly not present in any other layers at 12 Hz. Moreover, Figure 6.12 shows that the boundaries of the 12 Hz energy anomaly nicely agree with the gas-water contact interface at which the wavelet phase reversal occurs, which gives insights into how the geology and geophysics and, in some cases, the rock properties of the reservoir are linked. Figure 6.13 demonstrates the 12 Hz frequency map of RMS energy of the target sand with a window horizon  $\pm 35$  ms. The gas-containing sand was very accurately outlined at this frequency and the gas content quality was also indicated by the magnitude of the energy spectrum.

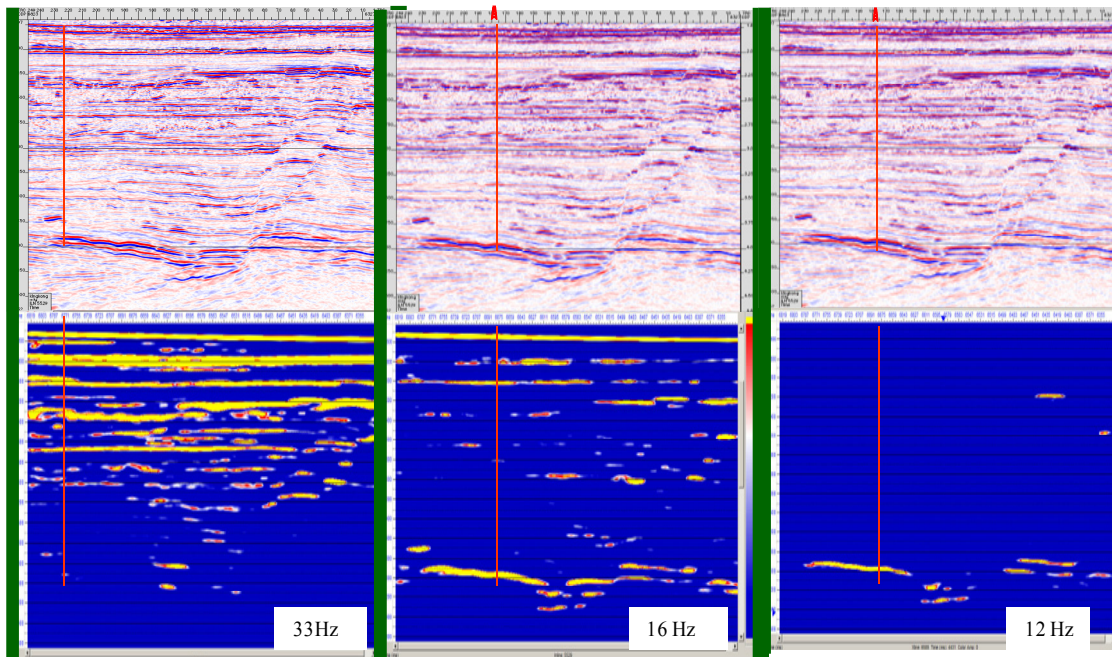


Figure 6.11 The results of the three common frequency sections (bottom) by the hybrid wavelet transform with Inline 5529 seismic profile.

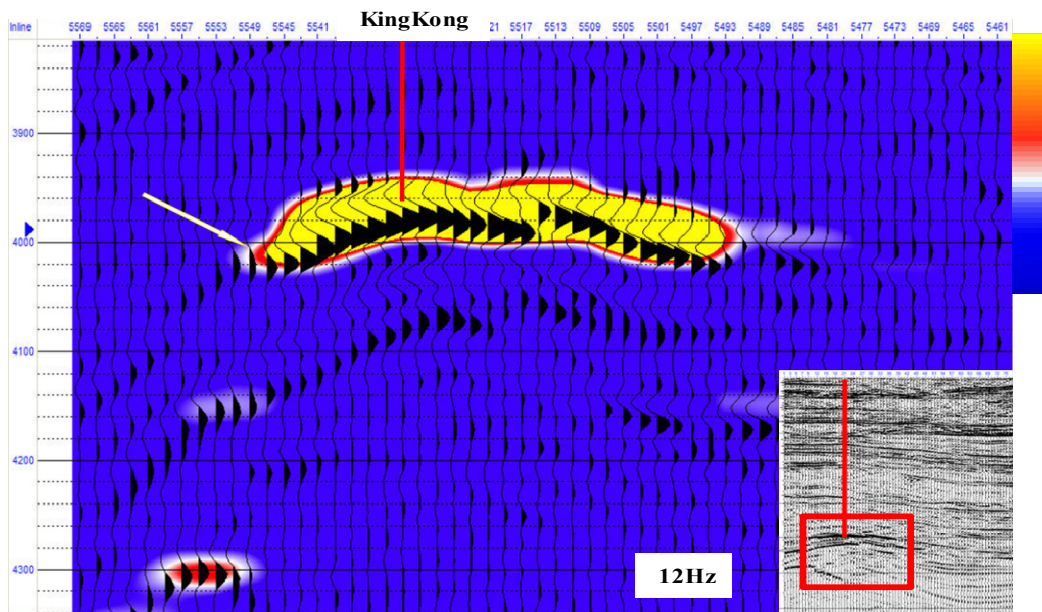


Figure 6.12 Local seismic trace profile (wiggle) and 12 Hz common frequency profile (colored background) near the KingKong well. Note that the arrow points the gas water contact boundary where the phase reversal occurs.

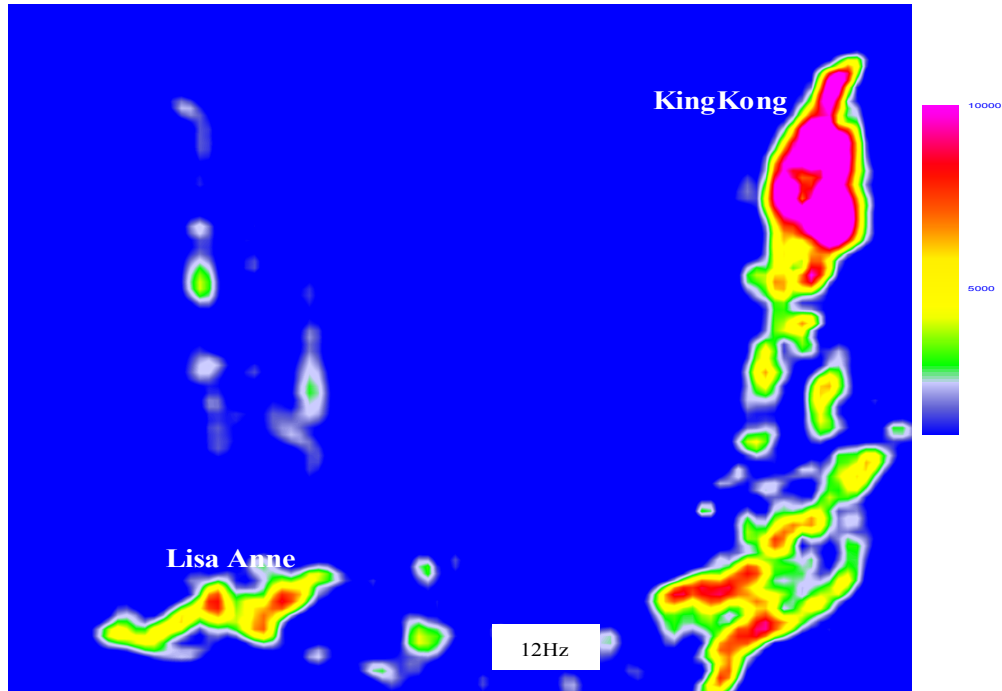


Figure 6.13 The 12 Hz frequency map of RMS energy of the target sand with a window horizon +/- 35 ms. The gas-containing sand was very accurately outlined at this frequency and the quality of gas-containing sand was also indicated by magnitude of energy spectrum.

These imply that the 12 Hz peak frequency can be used to detect and characterize the reservoir sands in this area.

### 6.3 Conclusions

In this chapter, we discussed the phenomenon of low-frequency energy anomalies associated with reservoir zones. The results of numerical forward modeling in the thin layer zone show that when seismic waves travel slower through gas than through the background material, their slower velocity results in a signal time delay. This signal time

delay is a major cause of the low frequency anomalies. A low attenuation factor  $Q$  is insufficient to produce large low-frequency anomalies in thin layer zones (one-half wavelength thickness or less).

Traditional methods to detect hydrocarbons that are based on the amplitudes of seismic reflections are subject to variation of many parameters such as thickness, lithology, porosity, and fluid content. Additionally, gas-bearing formations are not always characterized by very high-amplitude bright spots on the seismic data, so we cannot easily draw conclusions about the existence of hydrocarbons even if bright spots were present. In this thesis, we have demonstrated through an example of real data that the low-frequency anomaly attribute might provide a detailed and accurate estimate of the distribution of reservoir sands in the zone of interest in order to resolve such ambiguities. This suggests that studying low-frequency anomaly attributes can enhance the understanding of the reservoir by providing a clearer picture of the distribution, volume, and connectivity of the hydrocarbon-bearing facies of the reservoir. The low frequency anomaly attributes can also be a quantitative suite that aids the interpreter by defining the local geometry of the events. For example, these attributes could potentially be utilized when analyzing the stratigraphic elements in a sequence stratigraphic analysis. Moreover, since unique rock and fluid properties exist in the surrounding environment, each reservoir has its own characteristic frequency response to the seismic signal. Local frequency components can then be used to recognize hydrocarbon reservoirs.

## **CHAPTER 7**

### **Conclusions**

#### **7.1 Conclusions**

There are many examples that show the presence of low-frequency spectral anomalies highly correlated to the location of hydrocarbon reservoirs. In order to understand the physical causes underlying this phenomenon and utilize them as a hydrocarbon indicator attributes. In this dissertation, I built a set of wave-equation-based synthetic models with thin layer zones in order to evaluate the contributions of various factors to local frequency anomalies. The result of our analysis shows that the fact that seismic waves travel more slowly through gas zones than the background material is a primary cause of seismic time series delays and low-frequency anomalies in the thin layer reservoirs. Our explanation has been validated by the analysis of frequency anomalies corresponding to gas-bearing sands in the Gulf of Mexico fields. I used spectral decomposition to analyze the signal in the time-frequency domain. In order to maintain optimal resolution in the two domains, I designed an orthonormal wavelet that is optimized according to a desired signal in the least-squares sense. I used this wavelet to develop a hybrid spectral decomposition method that combines continuous wavelet transform with a non-linear operator. The seismic signal is a complicated signal having low amplitudes, making it difficult to analyze. However, the signal properties of seismic data can be enhanced by the use of matched wavelets. This new spectral decomposition tool can significantly improve frequency resolution and enhance local frequency components. Each reservoir has a characteristic frequency response to seismic energy determined by the unique rock and fluid properties in the surrounding environment. The tool can be used to directly

seismic frequency attributes from seismic data and identify frequency anomalies caused by gas or fluid energy absorption. Finally, the method is applied to gas-bearing sands in field data.

## **7.2 Main novelties and achievements of this dissertation**

1. I designed an orthonormal wavelet, which is optimized to a desired signal in the least-squares sense. For signal detection applications, the decomposition of a signal in the presence of noise using a wavelet matched to the signal produces a sharper or higher resolution in time-frequency space as compared to standard unmatched wavelets.
2. I developed a hybrid spectral decomposition method which combines the continuous wavelet transform (CWT) with a non-linear operator. This spectral decomposition method can significantly improve frequency resolution and enhance local frequency components. Compared to other spectral decomposition methods such as match pursuit, it provides an integrated, versatile, and efficient approach to analyzing non-stationary seismic signals. I show several examples of application to seismic attribute extraction and reservoir feature detection.
3. I used continuous wavelet transforms to estimate attenuation. I have found that spectral ratios obtained using continuous wavelet transforms are more accurate than those obtained using the Fourier transform, less subject to windowing problems, and more robust in the presence of noise, thereby resulting in a more robust and effective means of estimating  $Q$ .
4. I derived an analytic formula for investigating peak frequency characteristics of seismic reflections with attenuation in the thin layer zone. I discussed four types

of different wedge models to show that peak frequency gradually decreases as layer thickness increases. The results of the four wedge models all indicate that pure attenuation does not cause a significant peak frequency decrease in the thin layer zone, and that low velocity is a dominant factor causing the peak frequency decline.

5. To extract the frequency anomaly, I derived a formula for the analysis of the peak frequency trend based on the underlying physical mechanism of attenuation, which in turn yields a non-linear and non-stationary function. I also present a corollary algorithm for intrinsically finding the trend and implementing the de-trending operation. This method for extracting low-frequency anomaly attributes provides great advantages in isolating the potential target zone from its surrounding environments. This methodology is illustrated for hydrocarbon-bearing sands by the application of the KingKong field data.

## REFERENCES

1. Bahrampour, A.R, S. Izadnia, and M. Vahedi, 2008, A variational method for designing wavelets to match a specified signal: *Signal Processing*, Vol. 88, No. 10, 2417-2424.
2. Beatriz Quintal, Stefan M. Schmalholz, and Yuri Y. Podladchikov, 2009, Low-frequency reflections from a thin layer with high attenuation caused by interlayer flow, *Geophysics*, Vol. 74, No.1, N15–N23.
3. Bouyahia, S., J. Mbainabeye, and N. Ellouze, 2009, Wavelet Based microcalcifications detection in digitized mammograms: *ICGST-GVIP Journal*, Vol. 8, No. V, 23-31.
4. Castagna J. P., S. Sun, and R. Siegfried, 2003, Instantaneous spectral analysis: Detection of low-frequency shadows associated with hydrocarbons: *The Leading Edge* Vol. 22, 127–129.
5. Castagna, J. P., and S. Sun, 2006, Comparison of spectral decomposition methods: *First Break*, Vol. 24 (3), 75-79.
6. Chakraborty, A., and D. Okaya, 1995, Frequency-time decomposition of seismic data using wavelet based methods: *Geophysics*, Vol. 60, 1906–1916.
7. Chapa, M., and R. Rao, 2000, Algorithms for designing wavelets to match a Specified signal: *IEEE Transactions on Signal Processing*, Vol. 48, No. 12, 3395-3406.
8. Chui, C. K., 1992, Wavelet analysis and its applications, in *Wavelets: A tutorial in Theory and Applications*, Vol. 2: Academic Press.

9. Chung, H., and D. C. Lawton, 1995, Frequency characteristics of seismic reflections from thin beds: *Canadian Journal of Exploration Geophysicists*, Vol. 31, 32–37.
10. Daubechies, I., 1998, Orthonormal bases of compactly supported wavelets: *Communication on Pure and Applied Mathematics*, Vol. 41, 909-996.
11. Daubechies, I., 1992, *Ten Lectures on Wavelets*: Philadelphia, PA: SIAM.
12. Ebrom, D., 2004, The low frequency gas shadows in seismic sections. *The Leading Edge*, Vol. 23, 772.
13. Goloshubin, G., C. Van Schuyver, V. Korneev, D. Silin, and V. Vingalov, 2006, Reservoir imaging using low frequencies of seismic reflections: *The Leading Edge*, Vol. 25, 527–531.
14. Gonzales, R. C. and R. E. Woods, 2002, *Digital Image Processing: Second Edition*, Prentice Hall, 2002
15. Gupta, A., S. D. Joshi, and S. Prasad, 2005, A new approach for estimation of statistically matched wavelet: *IEEE Trans. Signal Process.*, Vol. 53, No. 5, 1178-1793.
16. Kazemeini<sup>1</sup>, S. H., C. Juhlin<sup>1</sup>, K. Zinck-Jørgensen, and B. Norden, 2009, Application of the continuous wavelet transform on seismic data for mapping of channel deposits and gas detection at the CO<sub>2</sub> SINK site, Ketzin, Germany: *Geophysical Prospecting*, Vol. 57, 111–123.
17. Klimentos, T. 1995, Attenuation of P- and S-waves as a method of distinguishing gas and condensate from oil and water. *Geophysics*, Vol. 60, 447-458.

18. Korneev, V. A., G. M. Goloshubin, T. M. Daley, and D. B. Silin, 2004, Seismic low-frequency effects in monitoring fluid-saturated reservoirs: *Geophysics*, Vol. 69, 522–532.
19. Kritski, A., A. P. Vincent, D. A. Yuen, and T. Carlsen, 2007, Adaptive wavelets for analyzing dispersive seismic waves: *Geophysics*, Vol.72, No.1, V1-V11.
20. Kumar, G., M. Batzle, and R. Hofmann, 2003, Effect of fluids on attenuation of elastic waves, 73th Annual International Meeting, SEG, Expanded Abstracts, 1592-1595.
21. Lange, J. N., and H. Almoghrabi, 1988 Lithology discrimination for thin layers using wavelet signal parameters: *Geophysics*, Vol. 53, No. 12, 1512-1519.
22. Li, H. B., W. Z. Zhao, H. Cao, F. C. Yao, and L.Y. Shao, 2006, Measures of scale based on the wavelet scalogram with applications to seismic attenuation: *Geophysics*, Vol. 71, No. 5, v111–v118.
23. Mallat, S., and W. L. Hwang, 1992, Singularity detection and processing with wavelets: *IEEE Transactions on Information Theory*, Vol. 38, 617-643,
24. Mallat, S., and Z. Zhang, 1993, Matching pursuit with time-frequency dictionaries: *IEEE Transactions on Signal Processing*, Vol. 41, 3397–3415.
25. Mallat, S., 1999, *Wavelet tour of signal processing*: Academic Press Inc.
26. Marfurt, K. J., and R. L. Kirlin, 2001, Narrow-band spectral analysis and thin-bed tuning: *Geophysics*, Vol. 66, 1274–1283.
27. Morlet, J., G. Arens, E. Fourgeau, and D. Giard, 1982, Wave propagation and sampling theory-Part II: sampling theory and complex waves: *Geophysics*, Vol. 47, 222-236.

28. O'Brien, J., 2004, Seismic amplitudes from low gas saturation sands: The Leading Edge, Vol. 23, 1236-1243.
29. Parra, J.O., and C. Hackert, 2002, Wave attenuation attributes as flow unit indicators: The Leading Edge, Vol. 21, No. 6 , 564-572.
30. Partyka, G. J., J. Gridley, and J. Lopez, 1999, Interpretational applications of spectral decomposition in reservoir characterization: The Leading Edge, Vol. 18, 353-360.
31. Percival, D. B., and A. T. Walden, 1993, Spectral Analysis for Physical Applications: Multitaper and Conventional Univariate Techniques: Cambridge University Press.
32. Puryear, C. I., and J. P. Castagna, 2006, Layer-thickness determination and stratigraphic interpretation using spectral inversion: Theory and application: Geophysics, Vol. 73, No. 2, R37-R48.
33. Rao, R., and A. Bopardikar, 1998, Wavelet Transforms: Introduction to Theory and Applications: Addison- Wesley.
34. Sinha, S., P. S. Routh, Anno, P. D., and J. P. Castagna, 2005, Spectral decomposition of seismic data with continuous-wavelet transforms. Geophysics, Vol. 70, 19-25.
35. Takla, G. F., B. G. Nair, and K. A. Loparo, 2006, Matching a wavelet to ECC signal: Proceedings IEEE 28th EMBS Annu. Conf. Aug.-Sept. 1686-1689.
36. Taner, M. T., F. Koehler, and R. E. Sheriff, 1979, Complex seismic trace analysis: Geophysics, Vol. 44, 1041-1063.

37. Vaidyanathanm, P. P, 1993, Multirate Systems and Filter Bank: Englewood Cliffs, NJ: Prentice-Hall, 1993.
38. Victor, C. , H. L. Chen, 2002, Time-Frequency Transforms for Radar Imaging and Signal Analysis: Artech House Publishers
39. Wang, Y., 2002, Seismic time-frequency spectral decomposition by matching pursuit: Geophysics, Vol. 72, No.1, V12-V20.
40. Winkler, K., and A. Nur, 1982, Seismic attenuation: Effects of pore fluids and frictional sliding, Geophysics, Vol. 47, 1– 15.
41. Lawton, W. M., 1991, Necessary and sufficient condition for constructing orthonormal wavelet bases, J. Math. Phys., Vol. 32(1), 57-61.